Department of Pharmacology and Therapeutics
School of Medicine
Autonomous University of Madrid

A novel nanoparticle-based system for sustained intravitreal drug delivery

Ignacio Melgar Asensio
BS. in Pharmaceutical Sciences
Thesis supervisors: Dr. Jack Henkin, Dr. Cristóbal de los Ríos Salgado
Tutor: Dr. Cristóbal de los Ríos Salgado

Teófilo Hernando Institute for R&D of drugs
Autonomous University of Madrid

Abstract/ Resumen

Abstract

lntravitreal (IVT) injection of anti-angiogenic proteins has become common in treating blinding neovascular intraocular diseases, but this suffers from rapid exit of active agents from the eye. Rapid drug loss is even more problematic for smaller agents to treat glaucoma or inflammation. Thus, many researchers have sought devices, usually microparticles (MP), to prolong IVT residence. These have not been approved, except with steroids, owing to foreign body reactions, especially in primates. The vitreous contains poly-anionic carbohydrates which could anchor smaller cationic nanoparticles (NP) but polycations are usually cytotoxic. Several reports now indicate greatly improved safety if the cations are derived from L-arginine (R; Arg). Our main goal has been to design and characterize R peptide NP conjugates (NPC), relating their R content and surface charge to increased duration of IVT residence; and relating these to increased IVT duration.

In this thesis, we have studied the relation between the amount of positive charges of peptides loaded to the nanoparticles, how they affect the zeta potential on the NP surface and its residence time in the vitreous. For the *in vivo* study we used rabbit eyes, an animal model closely modeling human pharmacokinetics. Our results show a half-life of <3 days for simple NP residence in vitreous, increasing in NPC from 7 to 17 days, depending on peptide R content, without any pathology or inflammation in rabbit ocular tissue at doses up to 360 µg per eye.

To enable prodrug delivery in this system, we have synthesized different types of amino-alkoxy esters with varied ester hydrolysis rates. From our first screening, we selected four amino-alkoxy ester candidates, which we then attached to a chromophoric hexanoic acid, and then we conjugated these to the NP to study the relevant ester hydrolysis. This identified two bridging esters, with respective hydrolysis $t_{1/2}$ near to 40 and 80 days, sufficient to enable sustained IVT protein delivery.

We also discovered and optimized di-carboxy half-amides of small R-containing peptides, which are active *in vivo* in a mouse model of age-related macular degeneration (AMD). Finally, we synthesized an ester-peptide prodrug of one such peptide, as an NPC, for slow release and efficacy studies, it displayed *in vitro* release $t_{1/2}$ of 28 days. Preliminary efficacy studies in the AMD model showed significant efficacy favoring the NPC over vehicle when these were each injected 14 days before laser-induced lesion. Free peptide injected simultaneously also gave a favorable trend (not statistically significant) compared to vehicle, but the conjugate was not clearly more efficacious than free peptide alone (not statistically significant). This is now being repeated with earlier injection (-28 days), where no free peptide effect is expected.

Resumen

La administración intravitrea de proteínas antiangiogénicas se ha convertido en el tratamiento más popular para las enfermedades neovasculares oculares, pero estos fármacos padecen de una excreción rápida del ojo. La rápida reducción de la concentración de fármaco en el ojo es incluso más acentuada para las pequeñas moléculas utilizadas en el tratamiento del glaucoma o la inflamación. Debido a esto, distintos grupos de investigadores han desarrollado formulaciones, normalmente micropartículas, para

incrementar la residencia intravitrea. Estos compuestos solo han sido aprobados para el uso con esteroides, debido a las reacciones de cuerpo extraño.

El humor vítreo contiene carbohidratos polianiónicos que se podrían fijar a nanopartículas catiónicas (NP) pero los policationes por lo general son citotóxicos. Estudios recientes muestran la seguridad en el uso de cationes provenientes del aminoácido L-arginina (R; Arg). Nuestro objetivo ha sido diseñar y caracterizar péptidos con R conjugadas a NP, relacionando su contenido de R y la carga en la superficie con el incremento de la residencia intravitrea.

En esta tesis doctoral, hemos estudiado cómo la relación entre la cantidad de cargas positivas de los péptidos conjugados a las NP afectan al potencial zeta en la superficie de las mismas y a su residencia en el humor vítreo. Para el estudio *in vivo* utilizamos ojos de conejo, el sistema experimental que más se aproxima al modelo farmacocinético de ojo humano. Nuestros resultados muestran una vida media de <3 días de residencia intravitrea para las NP sin péptido, aumentando en las NP conjugadas de 7 a 17 días, dependiendo de la cantidad de R que tenga el péptido conjugado a la NP, y sin ninguna evidencia de patología o inflamación en el tejido ocular de los conejos a una dosis de hasta 360 µg por ojo.

Para posibilitar la liberación de los péptidos a partir de profármacos conjugados a las NP, hemos utilizado diferentes tipos de amino-alcoholes sintetizando una gran variedad de ésteres con diferentes velocidades de hidrólisis. De nuestro primer cribado, hemos seleccionado cuatro candidatos a los que les unimos a un compuesto cromóforo con ácido hexanoico y los hemos conjugado a las NP para estudiar la hidrólisis desde éstas. Hemos identificado dos compuestos amino-éster con las velocidades medias de hidrolisis de 40 y 80 días, suficiente para conseguir una liberación intravitrea sostenida de proteínas.

También descubrimos y optimizamos hemiamidas dicarboxilicas de pequeños péptidos que contienen R que son activos *in vivo* en un modelo de degeneración macular asociada a la edad en ratón. Finalmente, se sintetizó un profármaco éster-peptídico de uno de tales péptidos en forma de NP conjugada, para estudios de liberación lenta y eficacia que mostró una liberación *in vitro* con una $t_{1/2}$ de 28 días. Los estudios preliminares *in vivo* mostraron eficacia significativa de la NP conjugada comparada con el vehículo cuando fueron inyectados 14 días antes de la inducción de la lesión. El péptido libre también dio una tendencia favorable (no estadísticamente significativa) en comparación con el vehículo,

pero la NP conjugada no fue claramente más eficaz que el péptido libre solo. Este estudio se está repitiendo ahora con una inyección anterior (28 días), donde no se espera un efecto del péptido libre.

Table of contents

Abbreviations

10 peptide (335)	COOH-adp-Sar-YNLYRVP-ethylamide
11 peptide (336)	COOH-adp-Sar-YNLYRVRS-amide
67LR	67 kDa non-integrin laminin receptor
ACN	acetonitrile
adp	Adipic acid
AdPEDF.11	adenovirus encoded PEDF
AGEs	advanced-glycation end products
AMD	age-related macular degeneration
APase	alkaline phosphatase
BCA	bicinchonic acid

BrMb	Bruch's membrane
CC	choriocapillaris complex
CDEX	condensed dextran
CDI	*N,N'*-carbonyldiimidazole
CK2	casein kinase
cmpd	compound
CNTF	ciliary neurotrophic factor
CNV	choroidal neovascularization
ColCh	column chromatography
CP	capillary plexus
CS	chondroitin sulfate
Cy7	cyanine 7 amine
d	day
DCM	dichloromethane
DDS	drug delivery system
DIPEA	*N,N*-diisopropylethylamine
DMAP	4-dimethylaminopyridine
DMF	*N,N*-dimethylformamide
DMSO	dimethyl sulfoxide
DNP	dinitrophenyl-ε-amino-n-caproic acid
EC	endothelial cells
ECM	extracellular matrix
EDI	enhanced depth imaging
EL	elastic layer
EMA	European medicine agency
eNOS	endothelial nitric oxide synthase
EPA	US environmental protection agency

EtOAc	ethyl acetate
EVA	ethylene vinyl acetate
Fab	fragment antigen-binding
FasL	Fas ligand
FDA	US food and drug administration
GA	geography atrophy
GAG	glycosaminoglycan
GCV	ganciclovir
glt	glutaric acid
h	hour
HA	hyaluronic acid
HATU	(1-[Bis(dimethylamino)methylene]-1H-1,2,3-triazolo[4,5-b]pyridinium 3-oxid hexafluorophosphate)
HBTU	*N,N,N′,N′*-tetramethyl-O-(1H-benzotriazol-1-yl)uronium hexafluorophosphate
HEPES	(4-(2-hydroxyethyl)-1-piperazineethanesulfonic acid)
HIF-1	hypoxia inducible factor
HPLC	high performance liquid chromatography
HSC	hepatic stellate cells
HSPG	heparin sulfate proteoglycans
ICAM-1	intracellular adhesion molecule-1
ICL	inner collagenous layer
IGF-I	insulin-like growth factor-I
IL-8	Interleukin-8
IM	intramuscular
IVIS	*in vivo* imaging system
IVT	intravitreal

LEDGF	lens epithelium-derived growth factor
LR	laminin receptor
MAC	membrane attack complex
MBHA	rink amide 4-methylbenzhydrylamine
MeOH	methanol
min	minute
MMp's	metalloproteinases
MP	microparticle
MW	molecular weight
MWCO	molecular weight cut off
NHP	non-human primates
nNOS	neuronal nitric oxide synthase
NOS	nitric oxide synthase
NP	nanoparticle
NPC	conjuated nanoparticle
OCL	outer collagenous layer
OCT	optical coherence tomography
OIR	oxygen-induced ischemic retinopathy
p/s	photons/second
P18	Peptide 18
PAD	peptidyl arginine deiminases
PAMAM	polyamidoamine
PBS	phosphate-buffered saline
PDGF	platelet-derived growth factor
PEDF	pigment epithelium-derived factor
PEG	polyethylene glycol
PGA	polyglycolic acid

PKA	protein kinase
PLA	poly(lactic acid)
PLGA	copolymer poly(lactic-co-glycolic acid)
PLGF	placental growth factor
p-nP	*p*-nitrophenyl
p-nPCOCl	*p*-nitrophenyl chloroformate
PPARϒ	peroxisome proliferator-activated receptor ϒ
PPI	poly-propylene imine
PR	photoreceptor
PVA	polyvinyl alcohol
Rh	rhodamine b
ROP	retinopathy of prematurity
RPE	retinal pigment epithelium
RT	room temperature
s	second
SDF-1α	stromal cell-derived factor 1-alpha
TEA	tryethylamine
TFA	tryfluoroacetic acid
TLC	thin layer chromatography
TM	trabecular meshwork
TSP-1	thrombospondin-1
UV-vis	ultraviolet-visible
VEGF	vascular endothelial growth factor
VIP	vasointestinal polypeptide

Introduction

The primary objective of the research described in this thesis project is the improved treatment of unmet medical needs in intraocular disease. This involves the use of a novel intravitreal drug delivery approach in which ionic interactions between drug carriers and vitreal components sustain residence in the eye, contrasting with more common size-based methods to prolong drug release. The hypothesis is that an optimized ionic formulation will provide advantages in safety and efficacy.

2.1 Wet age-related macular degeneration

2.1.1 *The posterior eye delivery problem*

Retinopathies and posterior eye diseases affect millions of patients and are major causes of blindness worldwide [1-3]. The effective treatments largely rely on a safe and efficient mode of therapeutic drug delivery. The unique anatomical and physiological barriers of the

eye block outside drug molecules from entering the posterior segment, thus, leaving the delivery efficiencies of conventional topical or systemic/oral drug administrations to be less than 5% [4, 5]. Currently, intravitreal (IVT) injection is the most efficient method for posterior eye drug delivery [6]. This directly delivers active agents near the lesions, increasing local drug concentration with low systemic exposure. IVT injection is the primary method to treat endophthalmitis, submacular/vitreous hemorrhage, retinal vascular occlusion, advanced age-related macular degeneration (AMD) and diabetic retinopathy [7]. In recent years, the acceptance of IVT injections has grown rapidly because of the injection of vascular endothelial growth factor (VEGF) inhibitors, which slows down the progress of neovascular retinal diseases, such as exudative AMD and diabetic retinopathy [6, 8]. In 2012, more than 2.3 million injections were reported, and the number was estimated to reach 6 million in 2016.

Despite advantages, with increasingly common use of IVT injection of proteins to treat retinopathies, IVT approaches to both large and small agent delivery are more acceptable but clearance varies with disease state [9], and is often impractical owing to rapid clearance, via retinal vasculature and intraocular drainage systems [3]. Consequently, repeated injections are needed to maintain a therapeutically effective concentration in the posterior eye. For example, the half-life of ranibizumab (a VEGF-neutralizing Fab fragment for treatment of exudative AMD) in human vitreous is approximately 8 days, requiring one administration per 4-6 weeks [10]. Frequent IVT injections raise the patients' discomfort, and cumulatively increases the risk of potential complications, such as vitreous hemorrhage, cataract and infection [11]. Additionally, frequent outpatient visits are a burden for vision-impaired patients and significantly increase total treatment cost [12].

2.1.2 *Age-related macular degeneration*

AMD is a progressive and degenerative chronic disease of the central retina, the macula, causing in advanced stages, a loss of central vision, which occurs at increasing frequency with age. The late stage of AMD is the third cause of blindness worldwide (8.7% in 2010) after glaucoma and cataracts and the main cause of legal blindness (10%-13%) among people, over 60 years old, and is their most common source of visual loss in developed countries. In fact, 30% of those at age 75 have lost vision to AMD [13]. This disease in the United States affects 15 million people. Moreover, AMD is a major medical and socioeconomic challenge worldwide also; the prevalence shows an expansion of this

disease due to the exponential increase in life expectancy and environmental risks like tobacco, genetic tendencies, the degree of pigmentation (with light colored eyes being at higher risk), arterial hypertension, ultraviolet rays, and consumption of a non-balanced diet. With these factors AMD incidence is predicted to increase by six-fold from 2010 to 2050 [14]. Nowadays, there are several treatments from the field of antiangiogenic therapies, these drugs are effective and they can prevent blindness and sometimes restore vision. However, while new biologics offer improvement these treatments are expensive, especially in countries where there is not a public healthcare system or on those that these treatments are not available yet, their delivery by repeated IVT injection is burdensome and carries risk of morbidity. AMD is the consequence of one of two processes that cause photoreceptor (PR) dysfunction: geographic atrophy (GA, dry or non-exudative AMD) or the more rapidly progressing choroidal neovascularization (CNV, wet or exudative AMD), only the latter responds to antiangiogenic agents. More than 50% of legal blindness related to AMD is from vision loss due to CNV. This is typically diagnosed by the phenotypes in fundus photographs of the macula: Retinal pigment epithelium (RPE) and/or retinal detachment, exudates (lipid degradation products left behind from a previous edema), fibrovascular scars, and hemorrhage in a small subset of patients [15]. Using imaging techniques such as fluorescein angiography and optical coherence tomography (OCT), the lesions are classified in subtypes: type 1 (sub-RPE), type 2 (sub-retinal), type 3 (intra-retinal), and mixed neovascularization [16]. These subtypes are gathered in three subclasses: classic, occult, and minimally classic lesions according to the filling patterns of fluorescein: well-defined lesions that leak fluorescein rapidly before the complete filling of retinal vessels are termed classic lesions, whereas occult lesions leak more slowly with poorly defined margins [17, 18].

In CNV, abnormal blood vessels sprout and grow from the choroid underneath the macula. These vessels leak blood into the retina, causing distortion of vision that makes straight lines look wavy, blind spots and loss of the central vision [19] (Figure 1 and 2).

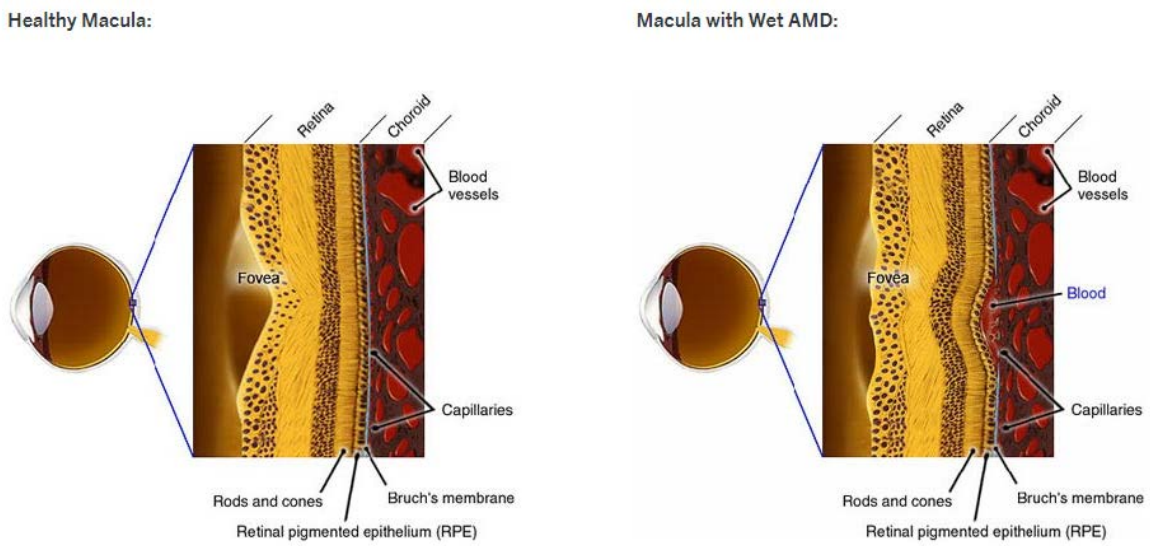

Figure 1. Scheme of a healthy macula and a macula with wet AMD where appears an accumulation of blood in the Bruch's membrane. Source: https://www.gene.com/patients/disease-education/age-related-macular-degeneration[20].

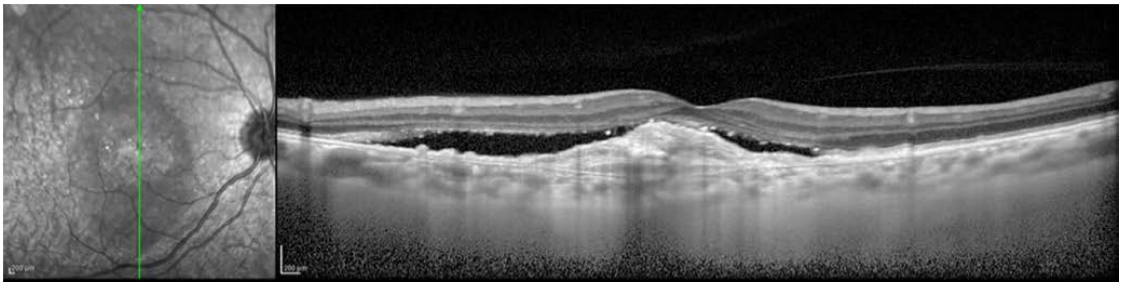

Figure 2. Left: fluorescein angiography (FA) shows a fibrovascular pigment epithelial detachment. **Right: spectral domain-optical coherence tomography** (SD-OCT) shows and a retinal detachment in a patient with age-related macular degeneration affected by a type 1 choroidal neovascularization. Both techniques are necessary for the diagnosis of this disease. FA reports information about posterior vitreous detachment and OCT gives more details about the details in the macula but only coverages a field of 1 mm. Source: Schmidt-Erfurth et al, 2014)[21].

2.2 Anatomy and physiology of the posterior eye

The retina is a light-sensitive layer located in the posterior area of the eye. There are two main layers: one comprising the neuroretina, formed by photoreceptors cells and glia cells, the second layer is formed by the RPE separated from the retina by a virtual subretinal space. This area contains the central vision and the 15-20° of the visual field. This tissue contains more than one layer of neurons called retinal ganglion cells [22]. The macula is a circular area 5 to 6 mm in diameter with the fovea at its center (0.8 mm) and surrounded by the para-fovea [23]. The pathogenesis of wet-AMD is associated with angiogenesis, the

growth of new blood vessels, predominantly from the choroid, where new capillaries break through Bruch's membrane growing aberrantly into the subretinal space. These vessels leak and bleed, causing exudative or hemorrhagic retinal detachments, ensuing scar formation leads to death of the RPE. A balance between positive and negative factors establishes the normal regulation of angiogenesis; the consequence of an alteration of this balance produces the growth of new vessels. The increased production of the proangiogenic VEGF has been identified as a strong driving factor of progression of the disease, thus anti-VEGFs are a mainstay of treatment.

According to Bhutto *et al.* [19], a relationship exists between the components of the photoreceptor, RPE, Bruch's membrane (BrMb), and the choriocapillaris (CC) complex. This is affected in AMD. CNV occurs when endothelial cells (EC) from this capillary plexus (CP) migrate and organize into sprouting neo-vessels perpendicular to their normal direction, and invade towards the retina. To accomplish this, the EC must first breach the BrMb. CC and BrMb structure are detailed below.

2.2.1 *Choriocapillaris*

This is the capillary component of the choroidal vasculature, sits adjacent and posterior to BrMb. CC is a single layer restricted to the inner portion of the choroid with the capillary plexus formed by arterioles and draining venules from below at right angles in the posterior pole. In the equatorial and peripheral choroid, arterioles and veins are located in the plane of CC. Inner choroidal vessels are sandwiched between two pigmented cells, apical RPE and outer choroidal melanocytes. The endothelial cells present in the CC are involved in secretion and /or filtration. The receptor expression of VEGFR-1 and VEGFR-2 have shown their expression on the vasculature side of the retina [24]. CC is the only capillary system in which the EC express intracellular adhesion molecule-1 (ICAM-1) [25]. ICAM-1 is responsible for firm adherence to endothelial cells by leukocytes (macrophages and neutrophils), with CD11b/CD18 on their surface.

The RPE/BrMb/CC system permits CC to provide the metabolic needs from serum for photoreceptors (PR) including 90% of the oxygen consumed by the PR in darkness [26].

The choroid lacks autoregulation [27]. Therefore, decreases in choroidal PO_2 can be caused by systemic hypoxia or elevated intraocular pressure. Choroidal nonperfusion is

unfavorable for PR function and its viability and retinal detachment from choroid addressing in PR death [26].

There is an intrinsic network of ganglion cells [NADPH-diaphorase] and nitric oxide synthase (NOS) positive] in the human choroidal stroma, whose neurons are connected to each other and to the perivascular network [19]. Ganglion cells are located in the temporal and central regions of the choroid, close to the walls of large arteries. They are solitary, polygonal cells with a diameter of 10-40 μm close to the walls of arteries [28].

Nitric oxide (NO) is a mediator of endothelium-derived factor relaxation that causes vasodilatation. NO is localized in the choroid with vasointestinal polypeptide (VIP), which has a vasodilation action. Endothelial nitric oxide synthase (eNOS) is associated with blood vessels in choroid while neuronal nitric oxide synthase (nNOS) was, in scattered cells throughout the choroid and the retinal pigment epithelium (RPE). nNOS is expressed in the choroid as a vasodilator, adjusting blood flow in response to a reduction of arteria blood pressure or protecting the retina from thermal damage associate with light exposure [19] (Figure 3).

2.2.2 *Bruch's membrane*

BrMb is a critical barrier separating the choroid capillary plexus from the retina, it is a connective tissue of 2-4 μm located between the RPE and the CC. This tissue is an elastin and collagen extracellular matrix (ECM), which function like molecular sieves. It has a penta-laminar structure formed by the basement membrane of the RPE (0.14-0.15 μm) most anterior; the inner collagenous layer (ICL); a porous elastic layer (EL); the outer collagenous layer (OCL; 0.7 μm of diameter); and the basement membrane of the endothelium of the choriocapillaris most posterior [29]. The main components of the structure are: collagen (type I, III, IV, V and VI) [30], fibronectin [31], laminin [32], heparin sulfate proteoglycans (HSPG) and chondroitin/dermatan sulfate [33].

BrMb is a stratified ECM complex that works as a biochemical barrier for normal physiological processes and to resist pathological ones like CNV. The functions of BrMb are:

-Regulating the reciprocal diffusion of bio-molecules, minerals and antioxidants components, trace elements and serum constituents between the choroid and RPE.

-Providing physical support for RPE cell adhesion [34, 35] and a surface for migration and perhaps differentiation of RPE [36].

-Wound healing [37].

-Acting as a barrier that restricts retinal and choroidal cellular migration, hallmarks of CNV.

Solute transport through BrMb is by passive diffusion due to its acellular nature. This depends on its molecular composition affected by age and location in the retina, the hydrostatic pressure on both sides and the concentration of the molecules and ions [19].

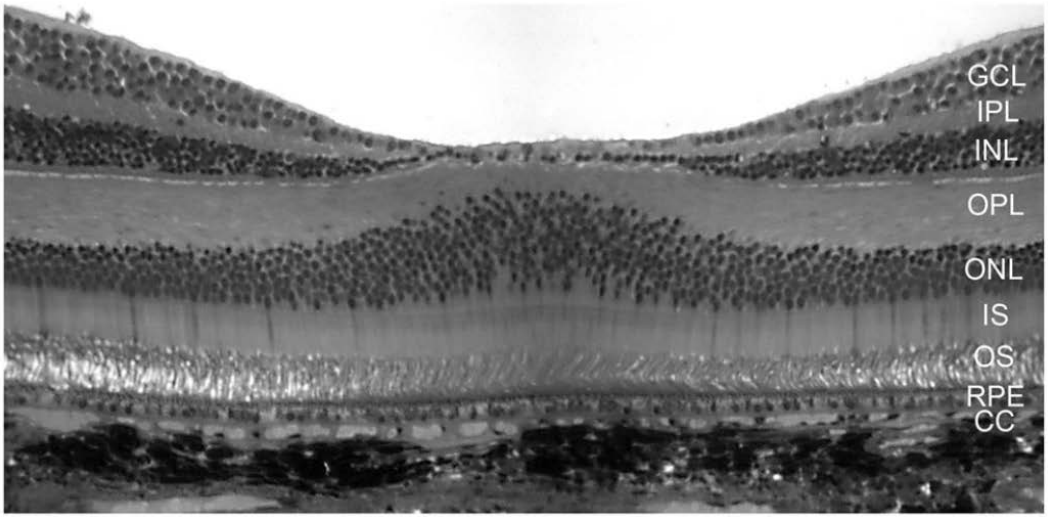

Figure 3. A cross section of the fovea from a Macaque monkey showing the layers of retina and the morphological relationship of photoreceptor/RPE/BrMb/choroid complex. On the sides of the foveal pit, the center of macula. The layers are formed by the ganglion cells (GCL). The inner plexiform layer (IPL). The inner nuclear layer of neurons (INL). The outer plexiform layer (OPL). The outer nuclear layer (ONL). The photoreceptor inner segments (IS). The outer segments (OS). The retinal pigment epithelium (RPE). The Bruch's membrane (not discernible at this magnification). The choriocapillaris (CC). The melanocytes of choroid are the structures below the CC. Source: Bhutto I, Lutty G (2012) [19].

2.2.3 *Retinal pigment epithelium*

The RPE is a single layer of hexagonal cells that are densely packed with pigment granules (melanosomes). Its location is posterior to the photoreceptors, these layers are polarized epithelial cells at the base of the retina. They are attached to their underlying basement membrane, which is the inner layer of BrMb. RPE continues as a membrane passing over the ciliary body and continuing as the posterior surface of the iris. At the surface, the RPE

faces BrMb, which separates RPE from the endothelium of the CC. The RPE function is to provide nutrients, like omega 3 fatty acids and glucose, to maintain the visual function by light-sensitive outer segments of the photoreceptors [38]. In addition, it transports ions, water and metabolic end-products from the subretinal space to the choroid. A second role of this tissue is the formation of the outer blood-retinal barrier to prevent nonspecific diffusion and transport material from the choroid. Melanosomes absorb the excess of light to protect the area from damage. Another function for RPE is serving as part of the waste disposal system. A RPE cell services between 20 and 30 photoreceptors, the RPE digests, and degrades 300 million rod membranes through a 70-year life span [39].

RPE produces and secretes several growth factors, angio-regulatory proteins, which maintain ocular angiogenesis in check: fibroblast growth factors (FGF-1, FGF-2, FGF-5) and transforming growth factor-β, insulin-like growth factor-I (IGF-I), ciliary neurotrophic factor (CNTF), platelet-derived growth factor (PDGF), VEGF, lens epithelium-derived growth factor (LEDGF), members of the interleukin family and pigment epithelium-derived factor (PEDF) to build and sustain the choroid and photoreceptors [14, 19].

2.2.4 *Photoreceptors*

PR are a type of neuron in the posterior retina which function in phototransduction, converting light into signals by triggering a change in the cell membrane potential after absorbing a photon. They are rich in mitochondria, supporting their highly metabolically active cells. These neurons consume more oxygen per gram of tissue weight than any cell in the body, also have a tissue oxygen level close to zero in the dark [26]. There are two types of photoreceptors cells that convert signals in vision: cones and rods. The chemical process in phototransduction is similar. Cones are wider than rods and less sensitive, so they require more brightness to produce a signal. The three cone cells that are present in humans are red, blue and green, they are responsible for response to different wavelengths of light. The average of rod loss is two rods /mm^2 of retina per year [23, 40]. One of the characteristics in the aging retina is the accumulation of mitochondrial DNA deletions and cytochrome c oxidase-deficient cones. These continuous changes might affect the macular function observed in aging and age related maculopathy [41].

2.3 Physiopathology of the posterior eye

2.3.1 *Changes in PR/ RPE/ BrMb/ CC complex in exudative "wet" AMD*

PR might be affected by the presence of scar formation, but this could be less severe if RPE is present on the scar. In addition, the thickness of the scar is related to the degree of the receptor degeneration. The thicker the scar, the greater the distance of the photoreceptors from surviving choriocapillaris [42, 43].

Another factor that could affect by this disease is a change in the ECM, with consequences relating to RPE function such as adhesion, proliferation, differentiation and migration. The effect of ECM is mainly through BrMb. Accumulation of advanced-glycation end products (AGEs) in RPE and BrMb produce oxidative stress and induction of CNV [44-46].

There are several theories about the choroid in AMD. Using enhanced depth imaging (EDI) a 16 μm per decade per life decrease in choroidal thickness per decade of life has been observed [47, 48]. According to another study, the decrease in choroidal thickness is more extreme, 54 μm per decade per life [49]. Other groups have not seen differences in the choroidal thickness between the AMD group and control [50, 51], but Wood et al has observed a retinal thickness, which may be related to the loss of PR [51].

The Friedman study hypothesized that vascular insufficiency resulted in loss of PR and RPE [52]. The loss in CC resulted in accumulation of waste at and on BrMb. Furthermore, AMD could be a consequence of a hemodynamic sequela of atherosclerotic changes affecting the postcapillary resistance of the choroidal vasculature [53].

Alkaline phosphatase activity (APase) is an indicator of endotherilal cell viability which is found in all viable choroidal blood vessels [54]. Large areas that lacked $APase^{+}$, in CNV, CC were covered with RPE. These areas with attenuation of CC around active CNV and scars were areas with associated with viable RPE cells. Areas with active CNV have RPE associated with them. These scars contain active CNV that appears stabilized. The vessels might be stabilized by the components of the scar. The scars are rich in two endogenous inhibitors of angiogenesis, PEDF and thrombospondin-1 (TSP-1) [19].

CNV is the endpoint in a variety of chorioretinal diseases. It is expressed as the growth of new blood vessels from the choroid into the subretinal space or sub-RPE [19]. There are three stages in CNV:

1 Initiation stage: endothelial cells from the choriocapillaris migrate towards the retina through the BrMb. Macrophages and cytokines are important on this stage.

2 Active stage: when CNV expands. It depends on the presence of inflammatory cells responding to cytokines in the area or producing cytokines releasing them in the autocrine and/ or paracrine way [55, 56].

3 Involution stage: CNV becomes fibrotic and forms disciform scar [19].

A balance between factors that simulate or inhibit vessel growth controls angiogenesis. In healthy tissues, inhibitory factors push the balance to control the vessel growth. In AMD, neovascularization happens due to the decreased production of inhibitory factors or increase of stimulators [57]. Also related with this process are matrix metalloproteins (MMP's) and other enzymes, which disrupt the ECM, permitting EC migration from vessels to tissue.

CNV is stimulated by growth factors such as VEGF, among others (insulin-like and fibroblast growth factors, interleukins and angiopoietins) [19].

VEGF is secreted by RPE, the higher basal secretion occurs towards BrMb [24]. VEGF acts as a specific EC mitogen and promoter of vascular permeability. Importantly, levels of VEGF in the vitreous are elevated in patients with wet-AMD [58].

Hypoxia inducible factor (HIF-1) in the submacular tissue is a signal of overproduction of VEGF [59]. In addition to angiogenesis, vasculogenesis and incorporation of EC precursors, are implicated in CNV development. VEGF is a chemoattractant for endothelial cells (EC) precursors, inducing their mobilization and differentiation [60]. The chemokine stromal cell-derived factor 1-alpha (SDF-1α) and its receptor CXCR4 are HIF inducible and involved in the recruitment of EC precursors into CNV [61{Sengupta, 2010 #44, 62]. VEGF is also a chemotactic signal for macrophages [63, 64].

In the initiation stage, macrophages and their cytokines are important in the growth of CNV. Vascular endothelium and macrophages produce MMP's, these enzymes degrade ECM allowing EC invasion through BrMb the infiltration of CNV [65]. MMP's are a family of ECM degrading enzymes associated with neovascularization. MMP-2 and MMP-9 types are closely involved in the progressive growth of choroidal neovascular membranes in AMD due to their location to the areas of new vessel formation and to the enveloping Bruch's membrane [66].

The physiological stability of the ocular vascular system is a balance between angiogenic and anti-angiogenic factors. Pathologic conditions shift the balance towards angiogenic factors that are released by the damaged cells [67, 68].

The endogenous angiogenesis inhibitors that are present in the eye are PEDF, endostatin and thrombospondin-1. They are extracellular proteins that are part of the matrix or bind to the matrix and frequently need proteolytic processing for their activation [69].

A study has shown that the three endogenous angiogenesis inhibitors are significantly reduced or absent in AMD in the BrMb/ CC complex due the presence of angiogenic inhibitors [70].

2.3.2 *Inflammation in AMD*

Inflammation is a cellular defense mechanism, in which foreign or damaged material becomes sensed by various pattern-recognition receptors [71]. The ligand recognition process triggers the activation of intracellular signaling pathways giving the production of pro-inflammatory mediators [72]. The activated endothelium in the blood vessels promotes and attracts effector cells and there is an accumulation of soluble proteins within inflamed tissue [73, 74]. The etiology of the inflammation is not the classical process. Evidence suggest it is a response to immunological effect [75]. There are several complement factors involved in this process: C3 complement fragments, C5 and the membrane attack complex (MAC) C5b-9 are present in ocular drusen and the capillary pillars of the choroid and in the vitreous of the human eye [76-78].

The complement system is a biochemical cascade that supports ~~to~~ antibodies to destroy pathogens. It promotes inflammation, eliminates pathogens and increase**s** the immune response. The complement system is formed by more than 20 proteins from the liver that circulate~~s~~ as inactive precursors (pro-proteins). When one of several triggers stimulates the pro-proteins, proteases in the complement system can cleave specific proteins, as consequence of this, cytokines are released starting the cascade. The result of the cell-killing MAC, which creates perforations in membrane [19].

2.4 Ocular proteins resisting angiogenesis

2.4.1 *Thrombospondin-1*

TSP-1 is a homotrimeric matricellular glycoprotein (420 kDa) that was first discovered in activated platelets [79]. TSP-1 is the most studied glycoprotein of the thrombospondin family (TSP-1, TSP-2, TSP-3, TSP-4 and TSP-5). TSP-1 is expressed on the cell surface in normal physiological processes. It is secreted by EC, fibroblasts, adipocytes, smooth muscle cells, monocytes, macrophages and transformed cells (malignant glioma cells) [80, 81]. TSP-1 is stored in the ECM, bound to proteins, like fibronectin, changing the conformation. The specific domain of this molecule binds to proteoglycans, membrane proteins like integrins among others [82, 83].

The structure of TSP-1 is formed by an N-terminal globular domain which binds heparin types I, II and III, and a terminal globular domain. The NH_2-terminal interacts with low-density lipoprotein receptor-related protein (LRP1). LRP1 releases any MMPs modulating the protease activity. This domain also binds heparin sulfate proteoglycans and several integrins related with angiogenesis, chemotaxis adhesion and cell motility [84, 85](Figure 4).

TSP-1 in humans is present at high levels in the vitreous and aqueous humor, and is an important component in BrMb [86, 87]. This protein plays a main role in the elimination of excess blood vessels during the late stages of retinal vascularization [14]. This effect is reduced in ischemic conditions when VEGF levels are high. The early and premature expression of TSP-1 in animal models, results in defective postnatal retinal vascular development and attenuation of retinal neovascularization during oxygen-induced ischemic retinopathy (OIR). A study with knockout mice for the gene Thbs1, compared to wild types, after a larger neovascular lesion, the CNV per area was 8 times greater in the knockout mice [88, 89]. There also exists a relationship between the area of CNV and the recruitment of macrophages after the lesion [14].

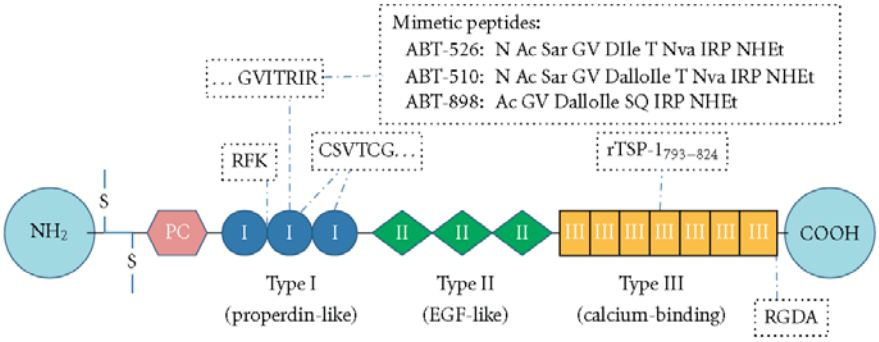

Figure 4. Structure representation of TSP-1 schematically and its receptor sites. The monomers have interchain disulfide bond, procollagen homology domain. RFK and RGDA are binding sites for TGFβ and integrins respectively. CSVTCG is the receptor site for CD36. The C-terminal domain of TSP-1 binds CD47. TSP-1 mimetic peptides have been designed from the heptapeptide GVITRIR, part of the monomer Type I. Source: Lopez-Dee et al, 2011 [90].

2.4.2 *Pigment epithelium-derived factor*

PEDF is a non-inhibitory serpin proteinase, [91, 92], and is a multifunctional protein committed in several physiological and pathophysiological mechanisms related with angiogenesis, neuroprotection, fibrogenesis, and inflammatory responses [93]. PEDF was identified for the first time as a secreted protein in a conditioned medium from fetal RPE cells that stimulated neuronal differentiation of Y79 retinoblastoma cells [94]. PEDF has a potent activity in the inhibition of the proliferation and migration of EC [95]. PEDF has an inhibitory activity on angiogenesis, is present at high levels in the eye, and might block the activity of pro-angiogenic factors. PEDF may be a key to modulate the neovascular homeostasis and prevent angiogenesis in healthy ocular tissue [96]. Retinopathy of prematurity (ROP) is a serious neovascular AMD-like disease of low birth weight premature infants, induced when they are moved, during neonatal support, from high oxygen to normal air. The vitreous of low birthweight infants lacks detectable PEDF, normally seen a full term [96]. PEDF only first appears in third trimester placenta [97]. OIR is an animal model system for ROP, in which newborn mice/rats are maintained at >50% O_2 for 5 days, then moved to room air, neovascularization appears 7-12 days later.

PEDF modulates blood vessel growth that drives angiogenesis when the oxygen concentration is low (same behavior as retinopathies and tumors) and an inhibitory environment when oxygen concentrations are normal or high [98]. According to Huang *et*

al, [99], they studied the relationship of PEDF in normal postnatal vascularization of the retina and retinal neovascularization (NV) during OIR.

OIR models produce robust pre-retinal neovascularization, mimicking the NV occurring in human ROP. ROP has become the leading cause of childhood blindness worldwide [100]. Even though many cases of ROP are not severe enough to require surgery ROP, with thousands of new cases worldwide every year frequently leads to lifelong vision problems ([101]). The abnormal angiogenesis in ROP is driven by pro-angiogenic growth factors, such as VEGF, the same as AMD. The current treatment with IVT injection of an anti-VEGF therapy (bevacizumab) has been reported as a supportive measure in aggressive posterior ROP [102-106]. Unfortunately, in newborns, the treatment is associated with concern about negative long-term outcomes in several organs due to its long half-life and the low blood volume in neonates [105, 107, 108]. PEDF has been identified as an "anti-angiogenic guardian of ocular function" [96], was reported to suppress ocular angiogenesis in animal models of ROP [95, 109, 110], and some peptide fragments of PEDF retain its antiangiogenic function, and are active *in vitro*, and *in vivo* in ROP models [110-112]. This is discussed in detail below.

An alternative OIR model in rats consists in the reduction of oxygen alternating 24-hour periods of 50% and 10% oxygen for 14 days of newborn rat pups. This regimen produces severe, reproducible, predictable, and measurable retinal NV similar to ROP and AMD [113-115]. Using PEDF-deficient knockout Serpinf1 mice, high oxygen exposure during OIR results in down regulation of pro-angiogenic factors and vessel obliteration and halts retinal vascular development. When animals were in presence of air, the ischemic retina produced a high level of angiogenic factors driving to the production of new abnormal blood vessels [99]. PEDF deficiency is associated with hyperoxia-mediated vessel obliteration during OIR with a crucial effect on retinal neovascularization [99].

PEDF acts as a protective factor for retinal EC tight junctions [116]. IVT administration of PEDF reduce retinal vascular permeability in rats with OIR and diabetes. Moreover, when there is a suppression of retinal neovascularization during OIR, overexpression of PEDF occurs with anti-angiogenic activity [117].

PEDF is also related with neuroprotection [118-120] and it promotes the survival of rod photoreceptor cells under degenerative conditions [118, 121, 122]. There is a link between the loss of PEDF and degeneration of photoreceptor cells in AMD [40, 123].

Administration of PEDF decreases motor neuron death and protects the survival of neurons from atrophy in neonatal mice exposed to the sciatic nerve section [124]. The lack of PEDF slightly affect the degeneration of retinal ganglion cells in an optic nerve crush model [14].

PEDF inhibits EC migration towards different pro-angiogenic factor such as VEGF, PDGF, Interleukin-8 (IL-8), acidic FGF and lysophosphatidic acid [98], so PEDF stimulates Fas ligand (FasL) expression and activates the FAS/ FASL transduction cascade leading to EC death [125].

PEDF affects the function of various cell types. In addition, it participates in RPE differentiation and maturation and when PEDF is made deficient as in KO animals. It affects RPE cell proliferation, migration, adhesion, oxidative state and phagocytic activity with minimal effect on their basal rate of apoptosis. This uncommon situation in RPE cells contributes to the pathogenesis of AMD [14, 126, 127]. The phagocytic function of RPE cells has a main role in the elimination of toxic metabolic waste and RPE cell survival ([128]; [129, 130]).

There is a specific epitope of PEDF, which contains the antiangiogenic activity, 34-mer (residues 24–57) which reproduces the PEDF angioinhibitory signals linking on c-*jun*-NH_2-kinase-dependent (JNK) nuclear factor of activated T cell deactivation causing apoptosis. The 34-mer has an antiangiogenic effect though the induction of endothelial cell apoptosis. 34-mer activates JNK increasing the inactive NFATc2 and reduces NFAT binding to the endogenous c-FLIP promoter, thus blocking proangiogenic survival signal [111]. One directly-binding high affinity receptor for the anti-angiogenic 34-mer within PEDF is the laminin receptor (LR), a 67 kDa protein localized on EC. It is involved in the inhibition of angiogenesis [131-133].

Also, 34-mer inhibits angiogenesis by selectively inducing tip cells apoptosis leaving unaltered the nonstimulated quiescent cells. 34-mer inhibits the angiogenesis through the Fas death pathway using peroxisome proliferator-activated receptor ϒ (PPARϒ), increasing surface FasL via up-regulating PPARϒ and activation of caspase-8 [134].

Wnt signaling-mediated PPARϒ suppression/ β-catenin [135], was studied a shorter sequence within the 34-mer this found that a sequence of 18 amino acids (P18) from the C-terminus of the 34-mer, modulates the signaling transduction between VEGF/VEGFR2 and suppresses activation of the PI3K/ Akt cascades, increasing the mitochondrial-mediated apoptosis anti-antiangiogenic activity [136] (Figure 5).

Several studies have shown that the 34-mer binds to the 67kDa non-integrin laminin receptor (67LR) and binds to the EC membranes suggesting that LR might be the true PEDF receptor for the process of angiogenesis inhibition [133]. Matsui et al, [137], has study the mechanism of 67LR in myeloma cells showing that binding 67LR with an antagonist blocks the binding of PEDF suppressing the PEDF effects. Moreover, LR agonists mimics the PEDF action. The trigger of the presence of LR is GnRH-II in ovarian cancer, it induces the 67LR precursor increasing the levels of LR. LR interacts with laminin in the ECM inducing the production of MMP-2 increasing the ovarian cancer cell invasion [138]. The 34-mer has a strong affinity and several interactions with 67LR. It acts as a proapoptotic epitope and, the 34-mer, uses the same mechanism to induce apoptosis in cancer, where 67LR is a very poor prognostic marker in epithelial ovarian cancer [139] as well as of activated EC [140] [141] (Figure 6). The activity of the 34 mer and its smaller P18 and also more N-terminal 25 mer (P46) is believed to rely on its alpha helical structure in PEDF, which must be maintained even in the isolated peptides.

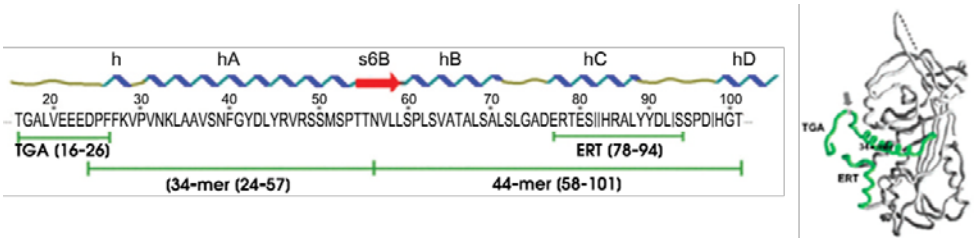

Figure 5. PEDF peptide structure. **Left:** Linear diagram of PEDF NH_2 terminus with the secondary structural elements indicated above. Peptides are marked in brackets below the primary structure. **Right:** The α-carbon diagram of PEDF backbone is sown with peptide location highlighted in green (arrow, TGA/34-mer overlap). Source: Filleur et al, 2005 (adapted)[111].

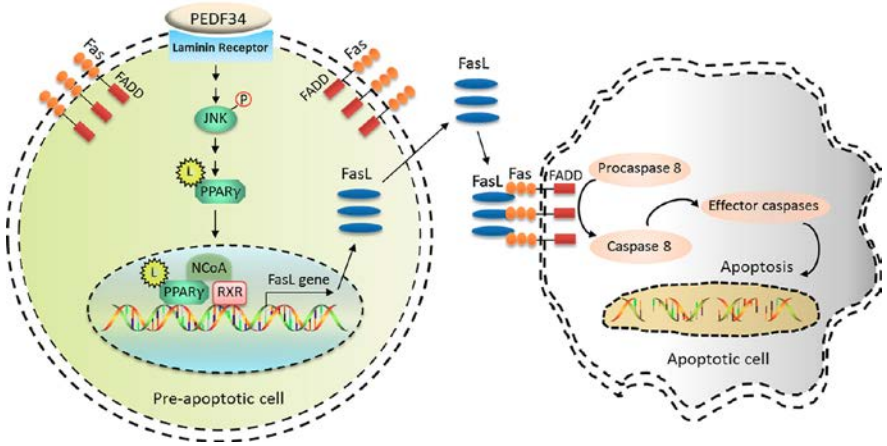

Figure 6. 34-mer epitope binds to LR to phosphorylate JNK MAPK, which activates PPARϒ through PPARϒ-ligand binding and nuclear translocation. PPARϒ activates FasL gene inducing the protein

expression. FasL. Paracrine FasL binds to FasL on the membrane binding to Fas activating the caspase-8 cascade. Source: Gong et al, 2014 [142].

2.5 The vitreous gel

2.5.1 *Collagens in the vitreous*

The human vitreous gel is a transparent extracellular matrix of 4.5 ml, formed by >98% of water without the presence of cells. The structure of the vitreous is formed by collagen fibrils with the types II, V/XI and IX [143]. The majority of the collagen corresponds to type II (60-70%). Type IX represents 20-25% of vitreous collagen, type IX is a heterotrimer and cannot form fibrils but it can interact with other collagen fibrils, moreover, alterations on this collagen might have a relationship with the most important age-related vitreous changes. Type V/XI collagen is the 10-15% of the total collagen in the vitreous. Types II and V/XI collagens combine to form a heterotypic fibril. Type IX collagen attaches to the COL2 domain of type II collagen keeping the space between fibrils. [144-148].

The average concentration of collagen in vitreous in humans is approximately 300 μg/mL [149]. The number of collagen fibrils to form the gel state of the vitreous comprises 10-20 μm in size, creating a random non-cross-linked network. The collagen is not uniformly distributed in vitreous; the highest concentration is located in the main site of synthesis, in the vitreous base. The concentration decreases towards the central and posterior parts of the vitreous, but then, increases in the posterior vitreous cortex adjacent to the retina [143] (Figure 7).

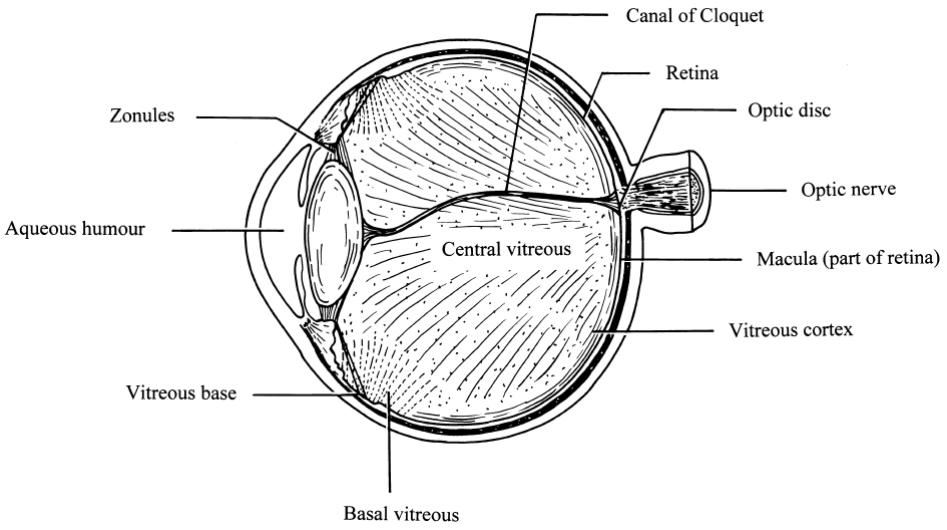

Figure 7. Anatomy of the vitreous and surrounding structures. The anatomical regions include the central vitreous, the basal vitreous, the vitreous cortex, the vitreoretinal interface and zonule. Source: Bishop et al, 2000 [143].

The central vitreous comprises the main bulk of the vitreous body. With age, the width of the retinal part of the vitreous base, might enlarge on its posterior border and become irregular [150]. The basal vitreous is formed by a dense bundle of collagen fibrils, which are very tightly adhered to the retina and to the non-pigmented ciliary epithelium of the pars plana [143] (Figure 7).

The vitreous cortex is a thin layer of 100-300 μm of vitreous gel that surrounds the central gel. The concentration of the collagen fibrils is higher than the concentration in the central vitreous. The vitreous cortex has two parts.

The anterior vitreous cortex goes from the pars plana covering the central part of the posterior surface of the lens. The vitreous cortex, which places between the pars plana and the lens and close to the zonules, is in contact with the aqueous humor (Figure 8).

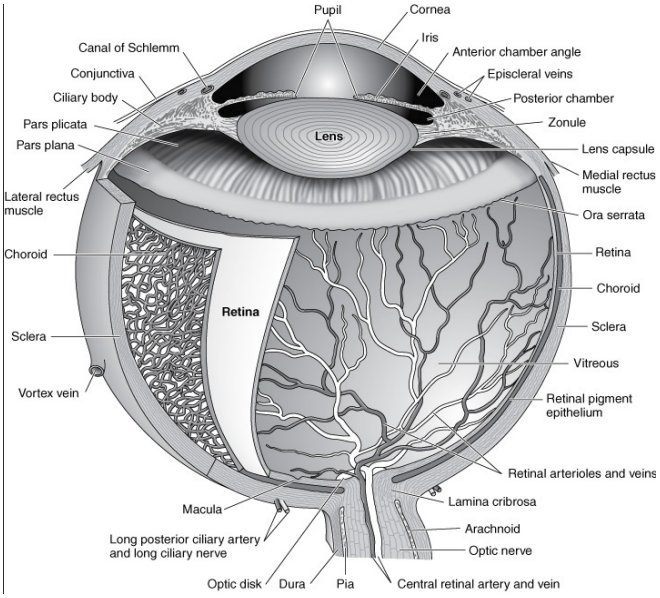

Figure 8. Schematic diagram of the eye. Source: Riordan-Eva and Whitcher. Vaughan and Asbury's General Ophthalmology, 17th Edition: http:www.accessmedicine.com (adapted) [151].

The physiological function of the vitreous gel is providing a conduit for metabolic requirements of the lens and excluding cells and large molecules from the vitreous to keep transparency [152]. Moreover, it is important its function coordinating eye growth protecting the eye from mechanical traumas and inhibition of angiogenesis [153] [154] [155].

The average in protein concentration in human vitreous is between 0.5 and 1 mg/mL. There are identified about 1,000 proteins [156]. The majority of the proteins funded in the vitreous, are derived from the plasma, so immunoglobulins and albumin are the 80% of the total protein [157]. The presence of these proteins in the vitreous might be due to the low-level leakage across the blood-retinal barrier, which when compromised increase the pass. These proteins are derived from fenestrated capillaries in the ciliary body stroma [158].

Between the collagen fibers, there is a large amount of hyaluronan (hyaluronic acid, HA). The vitreous doubles in volume during the development of a human. The concentration of HA in the eye during the development increases more than double, from 0.07 mg/mL to 1.8 mg/mL [159].

2.5.2 *Poly-anionic components of vitreous*

a) Hyaluronan of the vitreous

HA is a naturally occurring linear polysaccharide composed of glucuronic acid and N-acetylglucosamine repeats via a β-1,4 linkage. (Figure 9). It is found throughout the mucosa and many ECM of mammalian bodies, the highest concentration being in the vitreous body. HA comprises the vast majority of the uronic acid containing molecules (85–90%). HA is a polydisperse molecule with a high average molecular weight in the vitreous, where the major proportion, about 45 to 77% have a MW >1,000 kDa [160], It forms a spheroidal system with a diameter of 200-300 nm, ten times higher than the collagen fibrils. The HA molecular network consist of polysaccharide chains of 1-2 nm long space between chains is filled with water.

The poly-anionic nature of this molecule has the property to repel and can bind to water molecules giving a viscosity similar to gelatin [161]. The charges are affected by the pH and ionic strength of the environment and by the shape of the chains and the interaction with surrounding molecules. The amount of HA in the human vitreous is in the range of 100–400 μg/mL [162]; [161]. This solution creates a viscoelastic fluid system due to the molecular weight and the concentration and the structure, with the random distribution of thin molecular networks is responsible for vitreous transparency. HA distribution is not homogenous; the highest amount is located in the posterior cortical gel where the hyalocites are located, cells that continuously produce the HA. From the posterior chamber, it is washed by the aqueous to the anterior chamber and leaves the eye through the trabecular meshwork. The turnover time of HA in monkeys was several months due to the slow diffusion [163].

The main role of the HA is to provide a link between the collagen gel network of the vitreous and HA without covalent binding [160].

The rheological properties of the HA have shown that increasing the temperature and the presence of electrolytes in an aqueous solution with HA decreases the viscosity magnitude. [164].

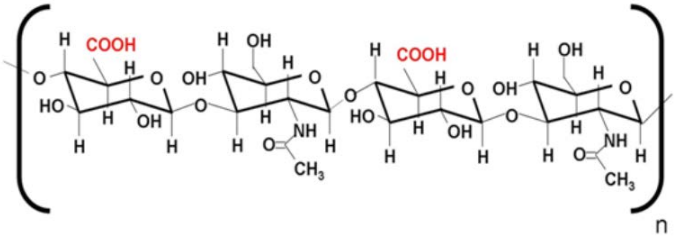

Figure 9. Chemical structure of HA. Source: Nagashima et al, 2011[165].

b) Proteoglycans of the vitreous

Proteoglycans are the third component of the vitreous with collagen and HA. They are in the liquid vitreous and they are not attached to the other two components of the vitreous. The most common proteoglycan in mammalian vitreous is called versican, which has a mass of 37 kDa and contains several sulfated disaccharides [166] [167] [168]. The other subtype of proteoglycan presence in the vitreous is type IX collagen. Similar to versican but, contains uronic acid and chondroitin sulfate (CS) [166, 169, 170]. There is a direct interaction of proteoglycans with HA but is very weak. This complex shows structural and immunological characteristics as versican [160] (Figure 10).

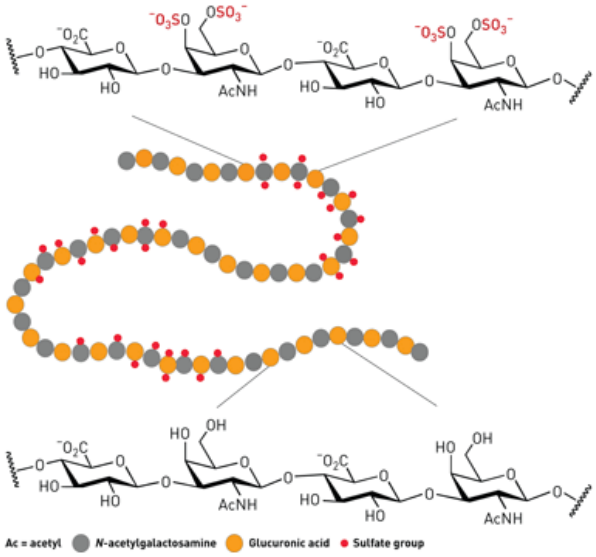

Figure 10. CS structure. Source: https://pubs.acs.org/cen/news/84/i33/8433sulfation.html [171].

The sulfation of the glycosaminoglycan (GAG) chains of the CS, gives the molecule the property to bind cationic molecules due to the high density of sulfate and carboxylic groups in its GAG moieties. The amount of versican in the human vitreous is 60 µg/mL [168]

2.5.3 *Aging changes in the vitreous body*

There are two different processes that occur at the same time, gel liquefaction and vitreoretinal interface weakening. At the end, the last step of the aging process is the posterior vitreous detachment.

Even when the presence of liquid vitreous has been observed at all ages, the first appearance is in the childhood [172]. The vitreous continues to develop after birth increasing the volume in parallel to the production of HA filling the vitreous body and giving support and stabilization for the collagen fibrillar network. The production of collagen fibers stops after birth and the space between fibrils increases as the gel becomes less dense (Figure 11). There is not liquid vitreous present in human eyes below the age of 4 years [173]. During the years, the amount of liquid increases reaching a 20% of the total vitreous volume to the age of 20. Sometimes might increases to 50% in people of 60 years old. In animals the liquid vitreous does not form, the exceptions are humans and rhesus monkeys [174]. During adulthood, the concentration of HA does not change in either of the two vitreous types [175] [176]. At age of 70, there is a slight increase of the HA concentration with the same molecular weight, but in that case in the liquid vitreous. This process starts with the appearance of narrow channels that evolve to pockets and pools of liquid vitreous that they gather each other at the age of 40-45 years. With time, this central liquid pocket occupies more than half the volume of the vitreous (Figure 12).

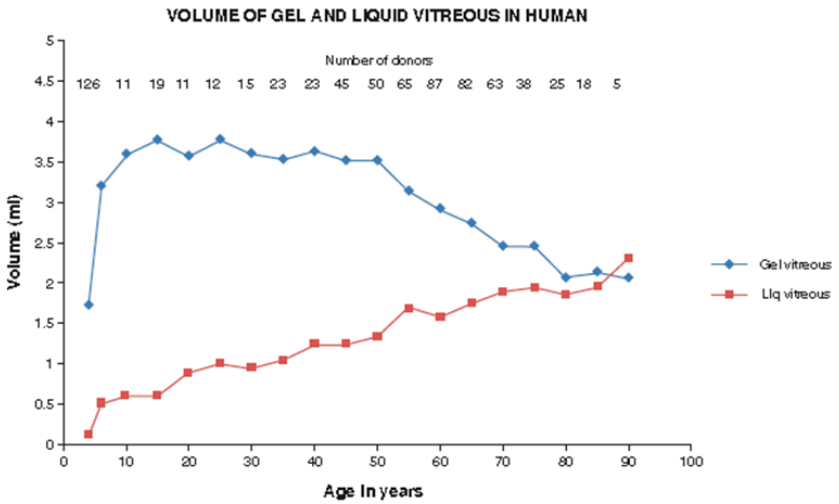

Figure 11. Representation of the average of volume of gel and liquid vitreous during the human development. The gel is stable during the first 40 years. Source: Tozer et al, 2014[177].

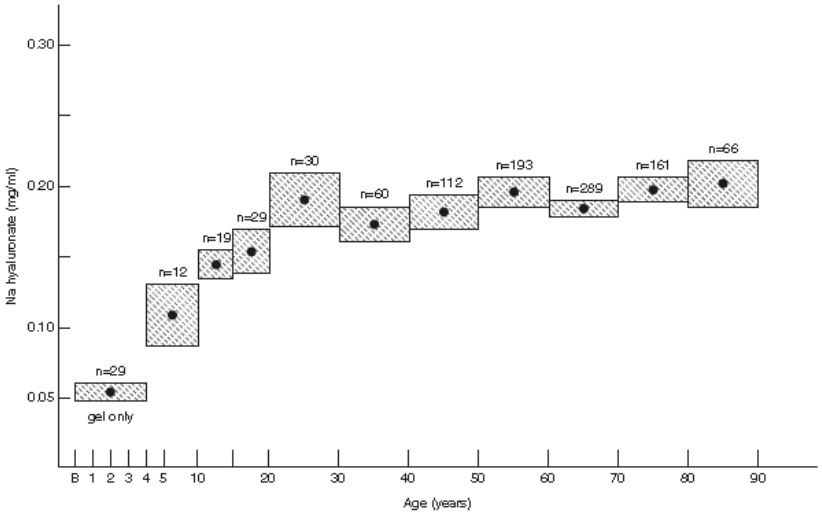

Figure 12. Concentration of HA in human gel vitreous throughout the life. The concentration increases until the age of 25. Source: Denlinger and Balazs [178].

Another process related to aging is the posterior vitreous detachment. This change is only documented in humans. This is a change that affects many people but it does not usually provoke an impairment of vision. The structural changes related on this process are a thickening of the basal lamina of the retina and an increase in the volume of liquid vitreous with a collapse of the gel and aggregation of the collagen fibrils. Posterior vitreous detachment can affect at any age as a result of chronic intraocular inflammation, traumas in the eye of highly myopic individuals. There are changes in the vitreous collagen like the nonenzymatic glycation and enzymatic cross-linking [179] [180, 181].

One of the procedures to substitute the vitreous is by vitrectomy surgery. In these cases, one uses a viscoelastic preparation made with Sodium Hyaluronate (Healon®). The properties of this compound are its high viscosity (varied MW & viscosities available) at low shear and at the same time low viscosity and high elasticity at high shear. This elastoviscous solution serves as a shock-absorbing body and protects delicate tissues and cell layers, such as, retina, iris, corneal endothelium [182].

2.6 Current treatments: Anti-VEGF's

VEGF is upregulated by hypoxia during the angiogenesis. VEGF activates quiescent endothelial cells and stimulate cell proliferation, migration and vascular permeability [183]. The intravitreal administration of recombinant human VEGF165 produces non-inflammatory iris neovascularization, ectropion uvea and neovascular glaucoma [184]. An alternative strategy was designed to inhibit the VEGF receptor tyrosine kinase (VEGFR-

2): sunitinib and sorafenib. These drugs were approved for the treatment of renal cell carcinoma and gastrointestinal stromal tumor respectively [185]. Avastin (bevacizumab) is a full-length humanized rhuMAb HER2 antibody (148 kD) and Lucentis (ranibizumab) is the humanized rhuMAb vascular endothelial growth factor Fab antibody (48.3 kD) isolated from bevacizumab [186]. But the inhibition of VEGFR-2 is proportionally related with the risk of blood pressure elevation [187] there is also a regulated increase in vascular permeability to both solutes and water [188] [189]. And VEGF regulates the apoptosis of EC, contributes to the maturation of vascular granulation tissue into avascular scar tissue and, to the pruning of retinal vessels during development [190].

The target of treatment has thus far been direct inhibition of VEGF in the eye with VEGF-A antagonists. There are four anti-VEGF drugs on the market for wet AMD.

2.6.1 *Pegaptanib*

Pegaptanib (Macugen, Pfizer) is a specific 28-base ribonucleic acid aptamer of 50 kDa aprox, covalently linked PEG [191, 192] with a high selectivity and inhibitor of VEGF-A_{165} isoform [192, 193], which has been implicated in blood-retinal barrier breakdown and pathological intraocular neovascularization [21]. Pegaptanib was found as the weaker drug to treat this disease [194]. The IVT half-life is 10 days; given at 0.3 mg every six weeks. *In vitro* and *in vivo* studies have shown that precursors of this drug inhibit the enhancement of EC proliferation and vascular permeability [195, 196]. Macugen was approved by the FDA in 2004 and by the EMA in 2006. Therapeutic benefit was very favorable in comparison with photodynamic therapy. However, was overturned in efficacy terms displaced by the next anti-VEGF drug, ranibizumab, since pegaptanib does not inhibit other bioactive isoforms of VEGF fragment *in vivo*. Pegaptanib is no longer recommended for the treatment of AMD [197].

2.6.2 *Ranibizumab*

Ranibizumab (Lucentis, Genentech), is a 48 kDa recombinant, monoclonal, humanized antibody Fab fragment which inhibits VEGF-A isoforms [192, 198, 199]. The binding site is located at amino acid sites 88-89 [200]. It is designed from the full-length monoclonal antibody bevacizumab (developed for cancer angiogenesis) by removing the Fc fragment from the parent molecule [201, 202]. Ranibizumab binds with high affinity a site present in all isoforms and their bioactive proteolytic fragments, including the soluble VEGF

isoforms 110, 121 and 165 and the tissue-bound isoforms 189 and 206 [203-205]. The half-life of ranibizumab is 2.9 days, in rabbits at a concentration of >0.1 μg/mL, the compound was maintained in vitreous humor for 29 days [206]. The relative molar binding activity to VEGF is 1, so excess drug has a rapid systemic clearance thus systemic safety of this drug is very high [207] [208]. The recommended dose is 0.5 mg/monthly injection and the initial loading dose is of three monthly injections. After this visual acuity is reached and patients have to be monitored monthly for visual acuity to continue the treatment, 1 injection every month if there is a loss of visual acuity. Lucentis was approved by the FDA in July 2006 and by the EMA in January 2007 [21].

2.6.3 *Bevacizumab*

Bevacizumab (Avastin, Genentech), is a full-length humanized anti-VEGF monoclonal IgG1 anti-VEGF-A antibody that inhibited the action of all isoforms of VEGF [192, 193, 198]. It binds to both $VEGF_{165}$a and $VEGF_{165}$b with equal affinity [209]. The target is the same as ranibizumab, the MW is 149 kDa and the half-life is longer than ranibizumab [199, 210]. Human IVT half-life is estimated at 4.32 days and its relative molar binding activity is 0.05-0.2, showing it has lower binding affinity than current treatments [211]. With a concentration of >10 μg/mL, bevacizumab was maintained in the vitreous humor for 30 days [212]. Bevacizumab was approved by the FDA and EMA for the treatment of different types of solid tumors (colorectal, non-epithelial lung, breast, ovarian and renal) and glioblastomas [213]. In ophthalmology it is used off-label. The recommended dose for intraocular treatment is 1.25 mg/month [214]. This is usually given as a 50 μL injection of 25 mg/mL protein.

2.6.4 *Aflibercept*

Aflibercept (Eylea, Regeneron), is a 115-kDa recombinant fusion protein which, in addition to inhibiting VEGF-A, also inhibits VEGF-B binding domains of human VEGFR-1 and VEGFR-2 fused to the Fc domain of human immunoglobulin G1. Aflibercept and ranibizumab have the same effect blocking endothelial cell proliferation and both are 10-fold more potent than bevacizumab and aflibercept is non-inferior to ranibizumab in treating wet AMD [192, 215]. Aflibercept binds to placental growth factor (PLGF), a proangiogenic protein present on EC and leukocytes [208]. It acts as a soluble decoy receptor recognizing and neutralizing all VEGF-A isoforms, with the establishment of a

tighter binding than the native receptors. It binds also PLGF-1 and PLGF-2 with a high affinity, greater than bevacizumab or ranibizumab. Therefore, the predicted binding affinity of aflibercept to its ligand is higher than ranibizumab (aflibercept: kDa = 0.49 pmol/L; ranibizumab: kDa = 0.46 pmol/L; ranibizumab: kDa = 0.58 pmol/L) [191]; [193]; [194]. The intravitreal half-life of aflibercept is 7.1 days and the relative molar binding is 140 thus, the activity in the eye of Eylea is 2.5 months [216] [217]. The FDA approval was granted in 2012. The recommended intravitreal dose is 2.0 mg/month for three consecutive treatments, followed by one injection every two months [218].

VEGF-A antagonists utility is limited by several factors. It has been reported that approximately 15-33% of patients with wet AMD are "nonresponders" despite undergoing treatment with anti-VEGF agents and a further 30-40% of patients will experience no improvement in vision and no change in lesion size [10, 219]. These treatments slow disease progression more often than they improve vision due to adaptive resistance of the system. The choroidal microenvironment responds to VEGF antagonists by increasing VEGF expression, and neovascularization can resurge between treatment cycles [220]. In addition, VEGF is not the only proangiogenic factor contributing to retinal neovascularization and its blockade can cause overproduction of other factors (IL-8, bFGF) as was shown for cancer angiogenesis [220]. In addition, the cons of these treatments, especially in the long-term period, are: the high frequently administration, IVT injection every 1-2 months, the price Eylea and Lucentis ranges from 800-1,900 USD (re-formulated Avastin is 50-100 USD) and most of them have potential side effects related to the eye and the circulatory system like, vitreous hemorrhage, retinal detachment, hypertension, etc [221, 222]. So novel compounds could decrease AMD progression with minimal local and systemic effects, with significantly reduced frequency of administration is important to enhance the effective of the treatment.

2.7 New possible alternative treatments

2.7.1 *Trombospondin-1-mimetics*

TSP1 is an endogenous inhibitor of angiogenesis with a promising effect in several diseases with a neovascular implication. Up-regulation of endogenous TSPs, synthetic TSP1 peptides or peptides derived from TSP were used to evaluate its therapeutic effects [223-225]. The expression of TSP1 is necessary for keeping the homeostasis and for reducing

and re-building the retinal vasculature during the development and maintenance of the inactive state of vasculature [14].

The mimic peptides derived of TSP1 have been used in several *in vitro* and *in vivo* tumor models [226-229]. Several studies have demonstrated that TSP1 suppress the cancer cell proliferation [226].

ABT-510 was developed to improve the pharmacodynamics and pharmacokinetic activity of TSP1 type 1 repeat peptide [227]. This peptide contains anti-angiogenic TSP-1 sequence with a single D-amino-acid substitution giving 1,000-fold greater anti-angiogenic activity. ABT-510 affects angiogenesis mechanisms; it competes with TSP-1 for binding EC, induction of FasL expression in EC, and inhibition of VEGF activity [227].

ABT-898 is a later generation of TSP1 mimic peptide, which given systemically, decreases the tumor size in mice with uveal melanoma. Systemic administration of this peptide has shown a 10-fold reduction in the mice tumor volume in comparison of mice control group [226]. It is also active by IVT injection in the laser induced mouse model of CNV [230].

TSP-1 blocks angiogenesis through specific apoptosis mechanisms that do not duplicate that of VEGF antagonists. Thus, TSP-1 mimetic peptides have the potential to act synergistically and to enhance activity of VEGF antagonists to mitigate CNV [14], (Figure 4).

2.7.2 *Pigment epithelium-derived factor and peptides derived from PEDF*

PEDF is recognized as a potent endogenous inhibitor of neovascularization. It is a 50 kDa glycoprotein, member of the serpin superfamily without serine protease inhibitor activity [92]. PEDF is a multifunctional protein with a broad spectrum of activities [96, 98, 112]. The inhibitory effect of PEDF was demonstrated by the inhibition of VEGF and FGF activity, only on newly forming blood vessels without affecting pre-existing blood vessels.

The administration of exogenous PEDF to a neovascularized area results in the inhibition of both EC migration and proliferation through the induction of apoptosis of recruited EC [231] [232]). The re-expression of PEDF in an area where this compound is not secreted like the human esophageal squamous cell carcinoma significantly inhibits their migration and proliferation and stop their growth by suppressing neovascularization [233]. Overexpression of PEDF decreased the size of ocular tumor metastasis associated with

reduced microvascular density in pre-clinical models [234]. PEDF overexpression decreased migration and capillary morphogenesis of melanoma cells *in vitro* [234] so; administration of PEDF is effective in attenuating angiogenesis and tumor growth.

PEDF was used in different studies for the *in vivo* treatment of ocular neovascularization with the purified protein and the recombinant PEDF, even with low doses without affecting the pre-existing blood vessels and the morphology [98, 235]. The administration of an adenovirus encoded PEDF (AdPEDF.11), inhibited CNV that corresponded with induced apoptosis of EC within the neovascularized area [236].

The active anti-angiogenic PEDF region is located in the 34-mer epitope, an anti-angiogenic 34-amino acid N-terminal peptide has been further shortened to 18 residues [111, 135], which was recently truncated to a smaller, more practical 9-amino acid fragment (P3-11), that retains anti-angiogenic activity. (Figures 5, 71, 72) [237]. A potently CNV-active 2nd generation 9-mer, peptide 11, is our CNV drug candidate, to be delivered here in prodrug form, as described in Materials and Methods and Results. The details of its discovery and bioactivity are described under the discussion section.

2.8 Prodrugs

A prodrug is a precursor of an active compound without or less activity that requires a chemical or enzymatic reaction after its administration to be active. The aim of these compounds is to improve and optimize the physicochemical, biopharmaceutical or pharmacokinetic properties of the active substances (absorption, distribution, metabolism and excretion) [238, 239], (Figure 13). Prodrugs are also known as reversible or bioreversible derivatives, latentiated drugs or biolabile drug-carrier conjugates [240-242].

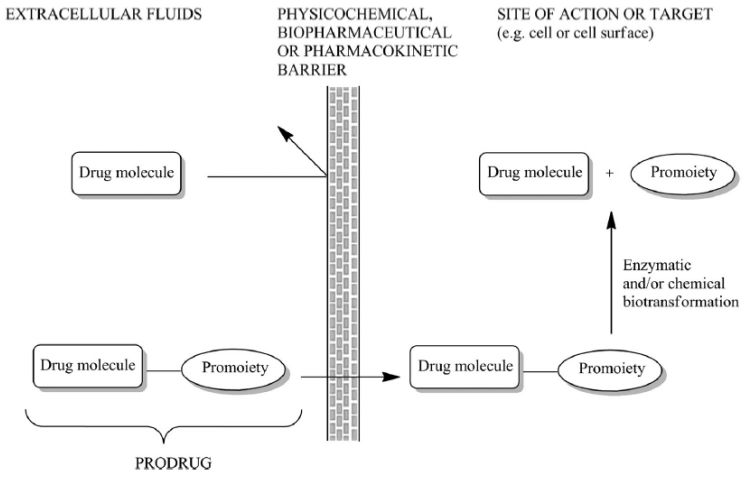

Figure 13. Illustration of the prodrug concept. The drug–promoiety is the prodrug that is generally pharmacologically inactive. The drug and promoiety are covalently linked via bioreversible groups that are chemically or enzymatically labile. Source: Huttunen et al, 2011 [239].

Inside the prodrug, there are several sub categories such as:

-Co-drugs, two pharmacologically active drugs that are coupled together in a single molecule so that each drug acts as a promoiety for the other [243, 244].

-Bioprecursor prodrug, a prodrug that does not contain a carrier or promoiety, but it needs a molecular modification to be the precursor that will be transformed to be pharmacologically active.

-Soft drugs, active drugs that are designed to undergo a predictable and controllable deactivation or metabolism *in vivo* after achieving their therapeutic effect [245, 246].

Currently, 10% of the drugs approved worldwide are classified as prodrugs, and approximately one third of all new drugs approved in 2008 were prodrugs [247].

2.8.1 *Functional groups related to prodrugs*

The selection of a prodrug might alter the characteristics of the drugs in terms of toxicity and distribution during the development of the drug. There are several factors that they have to study such as:

-Functional groups that might be candidates to react with a promoiety and generate the prodrug.

-Promoiety should be safe and without pharmacological activity and according to dose, duration of the therapy and state of the disease.

-Prodrug and drug need to study their ADME (absorption, distribution, metabolism, excretion) properties.

-Degradation by-products could affect to the drug stability.

The functional groups more used to design prodrugs are carboxylic, hydroxyl, amine, phosphate/phosphonate and carbonyl groups. The modification of these groups leads to ester, carbonates, carbamates, amides, phosphates and oximes. Other functional groups that have investigated for synthesize prodrugs. Thiols react as alcohols given new chemical bonds as thioethers and thioesters. Amines derivatize imines and Mannich bases [248-252] (Figure 14).

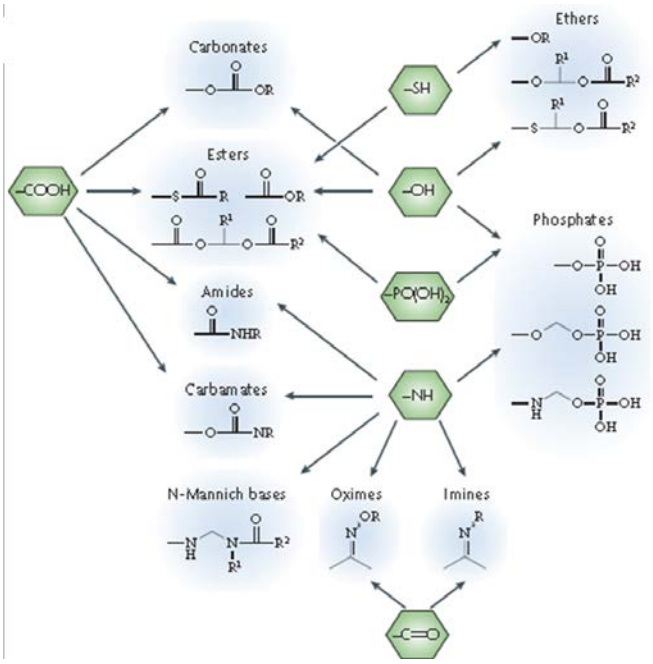

Figure 14. Common functional groups on parent drugs that are amenable to prodrug design (shown in green). Most prodrug approaches require a 'synthetic handle' on the drug, which are typically heteroatomic groups. Source: Rautio et al, 2008 [238].

2.8.2 *Esters as prodrugs of carboxyl and hydroxyl functionalities*

Ester is the chemical bond most used in prodrugs. The 49% of all marketed prodrugs have ester bonds whereby the drugs are released by enzymatic hydrolysis [253]. Spontaneous hydrolysis might be preferred when very long action is desired in a location where esterases are scarce. The most common purpose of ester prodrugs is to enhance the lipophilicity of water-soluble drugs by masking charged groups such as carboxylic acids and phosphates, to promote the passive membrane permeability [254].

In the body, the ester bond is readily hydrolyzed by esterase enzymes in the blood, liver and other organs and tissues, including carboxylesterases, acetylcholinesterases, butyrylcholinesterases, paraoxonases and arylesterases [255].

Nevertheless, one problem for the ester prodrugs is the prediction and extrapolation of the preclinical pharmacokinetic to humans, specifically on the difference of carboxylesterase activities among species [238].

A review published by Beamunt in 2003 [254], shows examples of several ester prodrugs designed to enhance the oral absorption of poorly permeable and polar drugs. There some cases which the slow and incomplete bioconversion of esters in human blood affects to the bioavailability. As an example, the oral bioavailability of the drug enalaprilate in humans is 36-44%, despite the 53-74% of the administrated drug that has been absorbed [254]. There are cases that the bioactivation has been boosted by the use of a double prodrug. This compounds needs to be modified by an enzymatic breakdown followed by an activation due to a chemical reaction and releasing the active compound. This approaching has been used for the administration of oral acyloxyalkyl ester prodrugs of β-lactam antibiotics [256, 257] (Figure 17).

2.8.3 *Carbamates*

These chemical bonds, also known as urethanes, differs of the ester bond due the presence of an oxygen and an amine on both sides of the carbonyl carbon. Carbamates are carboxylic acids and amine derivatives. These bonds are enzymatically more stable than esters but are more sensitive to hydrolysis than amides. The bioconversion of these bonds requires esterases for the release of the drug [258], (Figure 15).

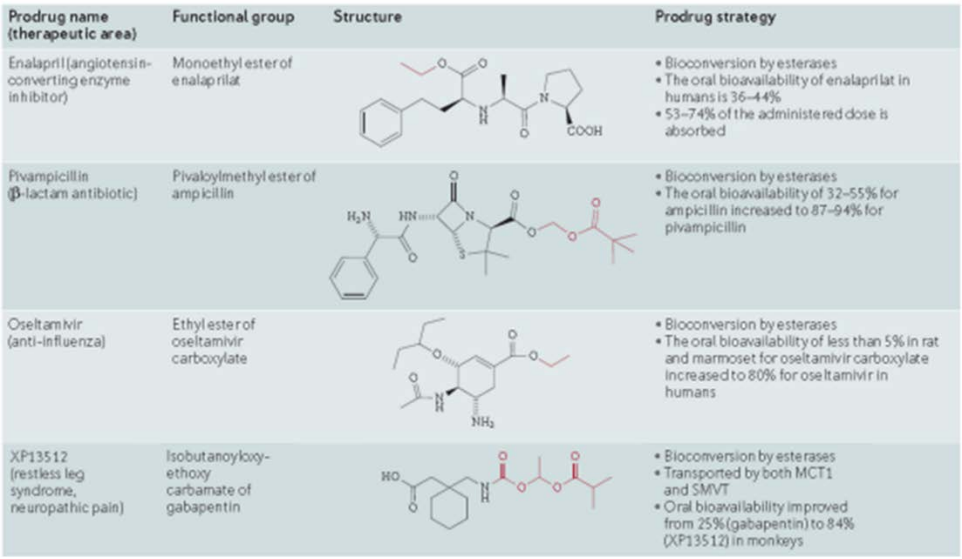

Figure 15. Example of commercial prodrugs formed by esters and carbamates and their properties. Source: Rautio et al, 2008 (adapted) [238].

2.8.4 *Prodrugs for the protection from rapid metabolism and excretion*

Rapid metabolic degradation of drugs could be protected by prodrugs. With the bronchodilator and β2-agonist terbutaline, converting its phenolic groups, which is the trigger to start the metabolic breakdown, into bis-dimethylcarbamates (bambuterol, AstraZeneca) (Figure 16). This is slowly bioactivated to terbutaline mainly by a nonspecific butyrylcholinesterase enzyme outside the lungs. As a consequence of the slow release and prolonged action of the drug, it is possible the administration of bambuterol once per day for the treatment of asthma reducing the adverse effects in comparison with terbutaline which needs to be administrated three times per day [259].

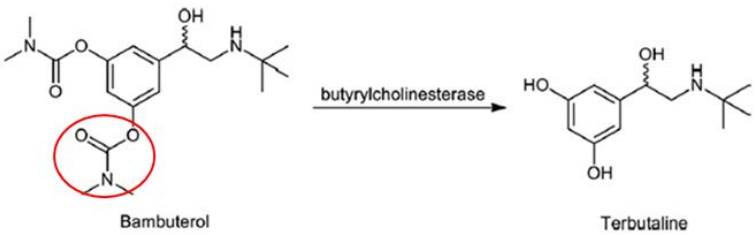

Figure 16. Bioactivation of terbutaline from bambuterol through the enzyme butyrylcholinesterase. The carbamate bond is highlighted. Source: Huttunen et al, 2011 (adapted) [239].

2.9 Drug delivery systems for intraocular administration

Release of drugs in the posterior segment of the eye to treat diseases, is a challenge from the point of the physiologic-anatomical of the eye and from the physicochemical properties of drugs. On the first challenge, there are several limitations and barriers such as the number of layers of tissue (corneal epithelium, corneal endothelium, conjunctiva and sclera), static barriers (sclera, Bruch's membrane-choroid and RPE), dynamic barriers (blood flow, lymphatic drainage, transport proteins of RPE, drug efflux pumps, organic ion transporters and bulk fluid flow from intraocular drainage systems). Metabolic barriers such as enzymes (esterase, peptidase, MMp's, Trypsins). On the second challenge, there are several variables to take care of (solubility, molecular dimensions, molecular weight, charges and functional groups) [260-264].

2.9.1 *Eye drops*

Eye drops is one of the vehicles used for the administration for anterior segment disorders (inflammation, glaucoma, infections), the disadvantage of this via is the low bioavailability through the cornea. The permeability of the drugs through the cornea is 1-7% but small hydrophilic drugs, peptides and proteins is zero [265]. On the other hand, molecules with the lower molecular weight have more permeability to cross to the posterior chamber [266]. Prodrugs were firstly used to improve the absorption of adrenaline through the cornea with its prodrug dipivalyl adrenaline (dipivefrin) [267, 268]. Dipivefrin is a dipivalic acid diester of adrenaline which penetrates the human cornea 17-times faster than adrenaline, due to the increase of 600 times of the adrenaline lipophilicity at pH 7.2 [269, 270]. Moreover, the efficacy of dipivefrin is almost 20 times more potent than adrenaline reducing the intraocular pressure and the systemic side effects are reduced [271, 272] (Figure 17). Fluid drainage from the anterior aqueous humor via the trabecular meshwork is relatively rapid, while vitreous is relatively stagnant, thus drugs entering from eye drops rarely reach the posterior eye. This makes topical delivery of agents against posterior disease nearly impossible. Figure 18.

Prodrug name (therapeutic area)	Functional group	Structure	Prodrug strategy
Dipivefrin (glaucoma)	Dipivalic acid diester of adrenaline	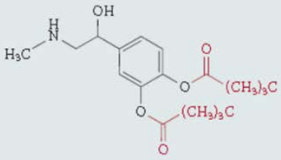	• Bioconversion by esterases • More lipophilic (600-fold) dipivefrin is able to permeate the human cornea 17-times faster than adrenaline
Latanoprost (glaucoma)	Isopropyl ester of latanoprost acid	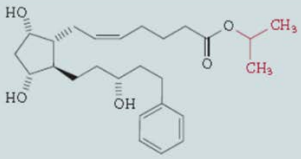	• Bioconversion by esterases • Improved lipophilicity achieves better ocular absorption and safety

Figure 17. Prodrugs for improve ophthalmic absorption and delivery using ester bonds. Source: Rautio et al, 2008 (adapted) [238].

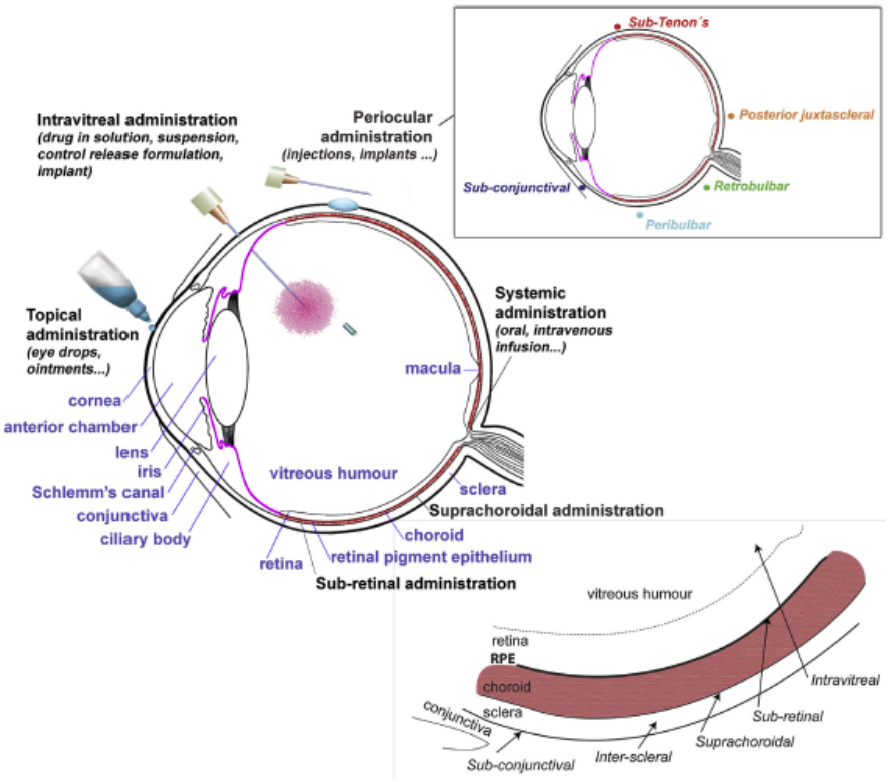

Figure 18. Different routes of drug administration for retinal drug delivery. Source: del Amo et al, 2017 [5].

2.9.2 *New drug delivery systems*

Nowadays, the development of new drug delivery systems (DDS) to release drugs in the posterior segment of the eye is of increasing interest. The carriers are designed to release

drugs to a specific space in a particular time. To design these DDSs, three techniques are considered:

1. Absorption promotion: Promotion of the passage of a drug through the tissue, which functions as a barrier.
2. Controlled release: efficient time-controlled sustained release of a locally administered drug.
3. Drug targeting: to allow it to act efficiently and exclusively on the target tissue [273].

The ophthalmic nanocarriers that have been more studied are liposomes and micro/ nanospheres and others that are taken more attention are emulsions and dendrimers.

With intravitreal injection it is possible to deliver solutions, suspensions and implants [274]. The advantages of implants are the long-term release, the zero-order kinetic release, and the possibility of remove the implant in case there are toxicological levels of the drug. There is a case where ganciclovir is formulated in a nonbiodegradable implant and administrated inside the eye. The release of the drug is during 6-8 months [3, 275]. The implant with fluocinolone acetonide (Retisert®) releases the drug is up to 30 months [276]. The disadvantage of these formulations is that the only way to remove it is by surgery. The half-life of most drugs in the vitreous is limited from 1-10 hours to 9 days as ranibizumab, a VEGF inhibitor used on the treatment of Age-related macular degeneration [10, 277-279].

There are several formulations to administer drugs, Sun and collaborators [280] have developed a thermosensitive drug delivery system to treat glaucoma, which releases brimonidine (anti-glaucoma) in rabbit eye in 7 days. Li and collaborators [281] have increased significantly the residency of Bevacizumab (Avastin®), treatment for AMD, to 90 days encapsulating the drug in nanoparticles of copolymer poly(lactic-co-glycolic acid) (PLGA). One of the problems of these formulations is the complexity of movement inside the eye, might be unpredictable and lead to toxicity and the observation of foreign body inflammatory responses to IVT-injected, spherical PLGA microspheres in rabbits, with more intense and prolonged such reactions recently seen in non-human primates (NHP) [5, 282, 283]. Another issue to solve is the diffusion of the particles in the vitreous, according to Xu and colleagues [12], PLGA nanoparticles with a size below 500 nm and neutral or negative charges diffuse in the bovine vitreous with low barrier. However, liposomes with an average of 116-139 nm and positive charges showed 10^3 times slower diffusion than

anionic liposomes (138-170 nm) in the porcine vitreous. If the treatment needs frequent injections, might be a risk of vitreous hemorrhage, cataracts and endophthalmitis [11].

a) Liposomes

Liposomes are small closed lipid vesicles (small lipid vesicles) formed by a phospholipid bilayer and where water-soluble drugs can be loaded in the aqueous phase and lipid-soluble drugs can be loaded into their lipid phase [284].

The advantages of liposomes are:

1. There are not covalent aggregates and their lipid composition, size and electric charge can be controlled [285].
2. To improve the targeting, it is possible to modify their surface with polymers, carbohydrates and antibodies [286].
3. Their toxicity and antigenicity are negligible [287].
4. Liposomes can be biodegradable and metabolized *in vivo* [287].
5. Membrane permeability can be controlled to some extent [288].
6. It is possible to use different solutes with different properties and molecular weights (fat-soluble molecules, water-soluble molecules and amphiphilic molecules) [288].

The disadvantages of this DDS are:

1. After the intravitreous injection, the vision is blurry.
2. Limited storage conditions.

Knowing these properties, several studies were developed on the intravitreal injection of drug loaded in liposomes. These studies have demonstrated that the release of the drug can be controlled, the half-life of the drug inside the vitreous body can be prolonged and the toxicity of the drug can be reduced [279].

A study conducted in rabbit eye, one group had received 1 mg of ganciclovir (GCV) encapsulated in a liposome. The other group had received free GCV in different concentrations (from 0.2 to 20 mg). After 72 hours, the rabbit eyes were they received free GCV, the one with the concentration higher that 5 mg showed therapeutic effect. In addition, GCV caused retinopathy at doses at 15 mg or higher. On the other hand, there was no indication of retinopathy in 1 mg of liposome-encapsulated GCV, in fact the concentration of the drug had demonstrated therapeutics levels up to 14 days after injection

ones, which had administered the free drug [289]. Moreover, fewer injections were required for liposomes loaded with GCV [290].

It is possible to improve the stability of the drug inside the vitreous by the addition of polyethylene glycol (PEG) to the surface of the liposomes, the function of PEG is to cover the liposome with a new aqueous layer [279].

There was a study where gentamicin was encapsulated in a liposome to check and compare with the free drug, the pharmacokinetics of the drug after injection in rabbit eyes [291]. This study has shown that the peak free drug concentration in the vitreous was significantly greater for the encapsulated drug than the free drug during 8 days. The areas under the drug concentration-time curve for the total drug and for the free drug in the case of the liposome encapsulated gentamicin were two fold and 1.5-fold higher, respectively [291].

In the case of bevacizumab encapsulated in liposomes, the concentration of the free drug and the encapsulated one was one fold and five fold higher at days 28 and 42, respectively, than the free drug [292] (Figure 21).

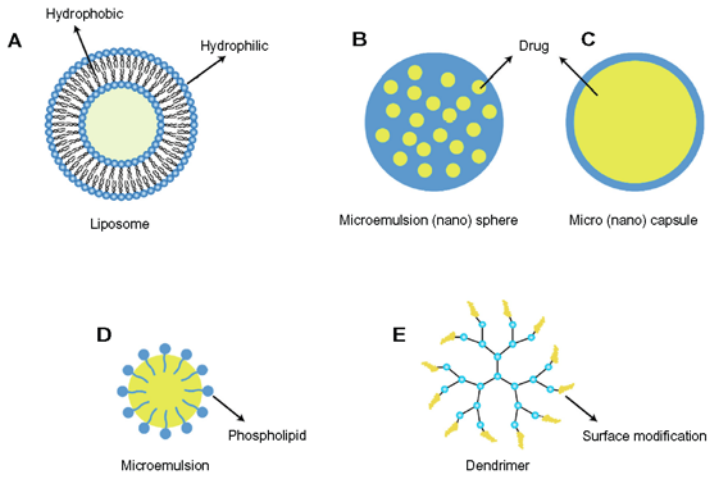

Figure 19. Formulation for injectable particles. (**A**) Liposomes. (**B**) Micro/ nanocapsules. (**C**) Micro/ nanocapsules. (**D**) Microemulsion. (**E**) Dendrimer. Source: Honda et al, 2013. [293]

b) Microspheres and nanospheres

Microspheres are spherical particles with a diameter from 1 µm to several hundred micrometers. If these particles have a diameter below 1 µm, they are considered nanospheres [294]. The particles could be made by synthetic and/or natural polymers and the architecture of the micro/nanospheres are made by multinuclear micro/ nanocapsules.

Drugs are encapsulated inside the spheres permitting sustained local release and tissue targeting of the drug [293].

The most used polymers are poly(lactic acid) (PLA), polyglycolic acid (PGA), and PLGA. These compounds are nonenzymatically hydrolyzed and degraded in vivo. Intravitreally injected PLA and PLGA had not shown electrophysiological or histological toxicity in the retina [282, 295], but a recent study have shown that the size, shape, and/or surface area of PLGA microspheres induce ocular inflammation in both rabbits and mokeys.[283] (Figure 19).

The first FDA-approved sustained-released formulation was an intraocular implant of GCV (Bitrasert®; Bausch and Lomb, Rochester, USA) that is a non-degradable *in vivo* and is being used in the treatment of cytomegalovirus retinitis in AIDS patients. This system is made by the polymers ethylene vinyl acetate (EVA) and polyvinyl alcohol (PVA), is implanted and allows the sustained release of 450 mg of the drug in 6-8 months [275]. Sometimes when the retinitis is not cure, the implant has to be removed without any complication [296].

The implant Ozurdex®, releases dexamethasone in the vitreous, the purpose of this drug is the treating of macular edema and associated with retinal vein occlusion. After 180 days of treatment there was an improve of visual acuity and retinal thickness. In addition, its efficacy is remarkable for the treatment of uveitis and diabetic retinopathy [297].

Microsphere might be transported to retinal pigment epithelial cells [298, 299]. The distribution of the particles into the tissues depends on their diameter. When three different sizes of a fluorescent nanospheres were injected into the vitreous of the rabbits, the 2,000 nm particles were found in the intravitreal cavity and the trabecula, whereas the 200 nm and 50 nm nanospheres were found inside the retina [300] (Figure 19).

c) Microemulsions

A microemulsion is a dispersion system made it by two immiscible substances (hydrophilic and hydrophobic) and a surfactant. The size of this system is as low as 100 nm or even less. Micelles are thermodynamically stable and can be formed easily without the need for strong agitation. The color is transparent or semitransparent due to the limited dispersion of visible light arising from their small size [301].

These formulations have good tissue permeability due to the small size of micelle and the surfactant. Thanks to micelles it was possible to enhance the intraocular permeability of dexamethasone in rabbit eyes [302, 303].

Autoclave is not possible for microemulsion sterilization and it is only suitable for short-term sustained drug release (Figure 19).

d) Dendrimers

Dendrimers are polymers formed by repetitive single molecules with a regularly branched structure, the central part is known as core meanwhile the external part is named dendrons. The regular shape is spherical and the molecular weight is homogeneous. All their physical properties, size and structures could be controlled at the molecular level [304, 305]. The disadvantages of this DDS are that the amount of drug that it is possible to conjugate is very limited and the in vivo safety is unclear. Most of the dendrimers are synthesized using polyamidoamine (PAMAM) and poly-propylene imine (PPI) [306]. There is not any approved dendrimer drug [293] (Figure 19).

2.10 Novel charge-based nanoparticle strategy

There have been many efforts to overcome the shortcomings of multiple IVT injections by extending the time of therapeutic release after delivery [4]. Slow-released colloidal drug carrier has become a preferred approach [4, 12, 307, 308]. These are normally nano/ micro-spheres made of biodegradable materials, with drug molecules embedded in their body or coated on their surface. After injection, the carriers remain in the vitreous over a relatively long period of time and slowly release the therapeutic molecules during their breakdown to smaller fragments until total clearance [308]. Advantages include biocompatible material for the carrier, and minimally invasive administrations. One critical issue limiting the clinical uses of the colloidal carriers is their relatively large size. These generally rely on large particle size (>10 μm) to prolong the diffusion through the viscous vitreous. While it varies according to age and other factors, the normal mesh size of vitreous is estimated from 500-1,000 nm [309]. Thus, neutral or negatively charged particles <200 nm in diameter move freely, but a strong diffusional slowing is observed above 500 nm. Most attempts to achieve slow drug release rely on extending IVT residence of colloidal carriers larger than this mesh size. These range over liposomes and micelles, polymers and thermal gels, for prolonged delivery of agents, from small molecules to antibodies. Typical carriers

are microparticles (MP), diameters >2 µm, for slow vitreal diffusion. These generally biodegrade for eventual removal, but cannot be sterile-filtered or autoclaved, a problem for safe IVT delivery. Their breakdown produces a continuum of sizes, some of which may obstruct the trabecular meshwork (TM), or activate its phagocytes. Commonly used poly(lactic-co-glycolic) MP (PLGA), though well tolerated in non-ocular sites, elicited a foreign body response in rabbit eyes [282], such MP have recently led to rabbit eye inflammation, and more severe and prolonged reaction in primates with potential for damage to critical structures [283]. With risk of causing glaucoma or tissue damage, few size-based carriers are approved for non-steroid drugs, making long-acting, smaller NP (<100 nm diameter) desirable.

One potential solution to reduce particle size while maintaining slow diffusion is to use cationic nanoparticle carriers. The vitreous has a very high content of poly-anionic polymers, especially the viscosity-enhancing, HA. Particles with poly-cationic compositions will anchor themselves to HA in vitreous through ionic binding, resulting in slow diffusion. In 2009, Kim *et al.* showed that albumin, freely diffusing in vitreous, was immobilized by converting its surface acidic residues to cationic amides with ethylenediamine (Zeta potential change from -33 to +11.7 mV) [310]. In 2013, Xu *et al*. reported that 200-nm polystyrene particles coated with cationic amine groups showed diffusion rates of 1000-fold slower than their neutral or anionic counterparts in bovine vitreous [12]. Using such cationic carriers, however, was not clinically practical since the particles are conjugated with multiple amino groups, which, along with most other cationic groups, are toxic, especially when multiple cations are on particles of a size that can be engulfed by cells [311].

Importantly, in 2011 Zern *et al*. [312] reported that when the positive charge is derived exclusively from L-arginine (L-Arg), small cationic particles were at least two orders of magnitude less toxic to cells. They compared cytotoxicity among cationic nanoparticles with varied sources of positive charges, including, L-Arg and D-Arg [312]. They found while all the particles are capable of forming complexes with polyanions, the L-Arg-based carriers were at least 200-fold less toxic than the non-arginine based cationic carriers and at least 10-fold less toxic than D-Arg carriers. Supporting evidence was then reported by Veiseh *et al.*, who compared the safety of cationic magnetic nano-vectors coated with either PEI or L-Arg ([313]). L-Arg particles showed no toxicity when injected into mice, while the PEI-based carriers produced hemolysis, erythrocyte aggregation and acute organ

toxicity. Sarker *et al.* compared lipofectamine transfection with 100-nm-diameter liposomes based on inserted lipid L-Arg [314]. Those with Zeta potentials higher than 20 mV gave far superior DNA delivery and displayed very low toxicity. The non-toxicity of L-Arg coating was further confirmed with dendrimers both *in vitro* and *in vivo* in delivery of Hsp27 siRNA to prostate tumor cells, this was efficacious against tumor growth in mice [315]. This range of observations suggested that L-Arg could be a practical and safe cationic group for anchoring nanoparticle carriers in vitreous humor. Based on these findings, our group designed and fabricated a novel L-Arg peptide-based cationic nanoparticle (NP), aiming to establish non-toxic, biocompatible therapeutic carriers for ocular drug delivery [316]. Their NP were less than 50 nm in diameter, with L-Arg containing peptides covalently linked to condensed dextran (CDEX) providing non-toxic positive charges for vitreous anchoring, thus extended IVT drug delivery. Small PEG peptides, having 1 to 4 L-Arg per peptide, were stably conjugated to carrier OH groups, with more Arg in a peptide increasing zeta potential [316], for which vitreal diffusion was monitored by rhodamine tag. Conjugates (approx. 100 kDa, 20-30 peptides/NP) with 4R peptides were highly immobilized. NP-conjugates (NPC) of 2R or 3R peptides gave slow diffusion in freshly isolated rat vitreous, and protamine competition, ex vivo, implied an ionic mechanism. These peptide conjugates gave prolonged intraocular residence in rats, histopathology showing no tissue damage. Our group experimentally confirmed ionic binding as the mechanism of slowed particle diffusion in a charge dependent manner, measured particle diffusion rate *ex vivo* and monitored the half-life *in vivo* in rat vitreous, and their relation to surface charge of the carriers (Zeta-potential). We found no adverse effects of NPC on ocular integrity by histological examination [316].

Aims

The main goal of this project is to design a novel sustained drug delivery system of newly designed potent PEDF-mimetic peptides to improve life quality of patients suffering from wet age-related macular degeneration, and other posterior retinal diseases. To achieve it, we will use three different approaches.

1) We will use a novel cationic charged-based NP for prolonged IVT residence. For this, we will conjugate anchoring peptides through stable carbamate bonds to NP (NPC). These cationic peptides with 2 or 3 L-arginines in their sequences have the property to be less toxic than any other source of positive charge. We will measure the residence time of NPC tagged with long wavelength fluorescent dye for *in vivo* clearance measurement in rabbit eyes.

2) We will synthesize ester-bridges, linker between the peptide and NP, with different amino-alcohols to measure kinetics of the ester's breakdown in physiological conditions. After a primary screening, we will measure their ester hydrolysis rates conjugated to the NP in an *in vitro* experiment in physiological conditions to select

the ester bonds with the same half-life hydrolysis rate as the residence time of the NPC with 2 R and 3 R peptides. These will define a platform for general ester prodrug delivery, where drugs are metastably attached to the long residence NPC described above.

3) We will study the efficacy a PEDF-mimetic nonapeptide, with 2 L-arginine in the sequence, derived from the 34-mer epitope in an in vivo model of neovascular disease. For this, we will synthesize an ester-peptide prodrug with a slow hydrolysis rate, which will be conjugate to the NP and getting an extended release and residence of the peptide in the vitreous.

By closely matching the half-life for residence time of the NPC and for the ester hydrolysis of the peptide prodrug we will accomplish an extended drug delivery system which will sustain the release of a maximum amount of the peptide in the vitreous.

Materials and Methods

3.1 Chemicals

Cis-4-(Boc-amino)cyclohexanol and trans-4-(Boc-amino)cyclohexanol were from Alfa Aesar, Ward Hill, MA, USA. *R,R*-trans-3-*N*-Boc-aminocyclopentanol was from PharmaBlock, Hatfield, PA, USA. *p*-nitrophenyl chloroformate, glutaryl chloride and adipic chloride were from Santa Cruz biotechnology, Santa Cruz, CA, USA, Cyanine 7 amine was from Lumiprobe, Hunt Valley, MD, USA. *m*-dPEG$_4$-amine was from Quanta Biodesign, Plain City, OH, US. All other chemical reagents were from Sigma Aldrich, St Louis, MO, USA.

3.2 Synthesis of condensed dextran nanocarriers

The nanoparticles, which were used on this project, were synthetized from condensed cholesteryl dextran (CDEX) from 70 kDa dextran, as described by Li et al, 2017[316].

Dextran was first dried by twice repeated rotary evaporation from anhydrous pyridine, followed by exposure to high vacuum in a dessicator containing phosphorus pentoxide (P_2O_5). Then 4 mol% attachment of cholesteryl groups (based on 365 glycosyl monomers per 70 kDa, 4 g dextran = 21 mmol) was accomplished by linking cholesteryl chloroformate to polymer hydroxyl groups. Cholesterol chloroformate (0.4 g, 0.88 mmol) and one equivalent of triethylamine (TEA) in 10 mL of dichloromethane (DCM) was stirred into a solution of 4.0 g dry dextran in 50 mL of anhydrous dimethyl sulfoxide (DMSO). Sealed reaction continued 3 h at 40 °C, the mixture was quenched with 50 mL distilled water and exhaustively dialyzed (dialysis bag MWCO 12,400 Da, Spectra Por, Rancho Dominguez, CA, USA. Polymer solution was shell frozen freeze-dried (VirTis Benchtop lyophilizer, SP Scientific, Gardinier, NY, USA), the cake reconstituted with 50 mL of distilled water and sonicated (Branson 1800; Branson Ultrasonics, USA) for 2 h to maximize internalization of hydrophobic groups. Additionally, the cloudy CDEX solution was sequentially filtered through filter paper, then successively through syringe filters of 0.80 µm, 0.45 µm and 0.20 µm pore size, the final filtrate then was frozen and re-lyophilized. Linked cholesterol units self-associate to form a core, thus contracting the carrier into a smaller, more spherical volume of condensed dextran (CDEX, 75 kDa), having a central hydrophobic domain.

3.3 *In vivo* diffusion study of CDEX in rabbit vitreous

To study the rate of diffusion, measured as rates of ocular NP loss, an in vivo experiment was designed to compare NP themselves with peptide-conjugated NP with two different types of anchoring peptides (2Arg or 3Arg), with similar loads of peptides attached to their surface. These peptides were designed to reduce the speed of diffusion of the nanocarrier in the vitreous due to the creation of multiple ionic interactions between the positive charges from peptide arginines and the negative charges of the hyaluronic acid present vitreous (Figure 20). The peptides were derived from short amino acid sequences of the alpha A proteins crystallin, Hsp20 and PEDF protein that were naturally found in the eye to minimize immunogenicity. They differ in that one of them had 2 positive charges (pyrrolidine-3-CO-PEG_8-CO-YRVRS-amide; MW: 1,198 g/mol, 2R) and the other peptide contained 3 positive charges (pyrrolidine-3-PEG_8-CO-RRYRL-amide; MW: 1,281 g/mol, 3R). The function of positive charges was to interact with the molecules of hyaluronic acid, an anionic polymer very abundant in the vitreous humor. The sum of numerous weak ionic attractions was intended to reduce the rate of diffusion and therefore increases the residence

time of the particles in the eye. These peptides were anchored to CDEX through a short chain of PEG followed by a pyrrolidine molecule. The pyrrolidine nitrogen efficiently forms a stable carbamate bond with activated hydroxyl groups found in dextran. The pyrrolidine PEG peptide amides were synthesized via Fmoc-based solid-state peptide synthesis on rink amide 4-methylbenzhydrylamine (MBHA) resin using a CEM Liberty Blue microwave-assisted peptide synthesizer. Fmoc-*N*-amido-PEG_8-carboxylic acid addition was carried out by manual coupling using *N,N,N′,N′*-tetramethyl-*O*-(1*H*-benzotriazol-1-yl)uronium hexafluorophosphate (HBTU) and excess *N*,*N*-diisopropylethylamine (DIPEA). Following the Fmoc removal, *N*-Boc-pyrrolidine-3-carboxylic acid was then coupled using HBTU and excess diisopropylethylamine. After cleavage from the resin and deprotection with trifluoroacetic acid (TFA), the final product peptides were purified by HPLC and lyophilized. Peptide purity before conjugation (>95%) was confirmed by analytical HPLC and mass spectrometry. In both cases, the positive charges were from the presence of the arginines in the sequences.

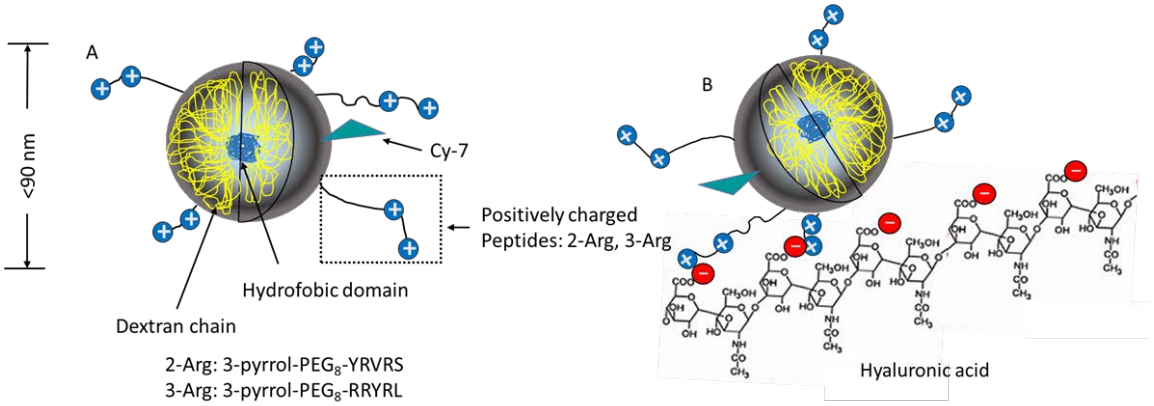

Figure 20. Schematic view of CDEX NPC in vitreous. A hydrophobic cholesteryl domain forms the NP core. Conjugated PEG-peptides extend outwards (much lower than actual loading shown for un-crowded view). NP are labeled by Cy7 amine, to yield <1 Cy7/NP. Two types of positively charged peptides were linked at 61-64 peptides per NP. NPC are immobilized in vitreous by ionic binding between L-Arg guanidinium groups (blue circles) on their surface and HA polymer (red circles are HA carboxylate groups).

3.3.1 *Attachment of compounds to the nanogel CDEX*

a) Step 1: activation of CDEX

The method used to attach the compounds to nanogels was based on the methods of Ramirez et al (1995) [317] and Vandoorne et al (1985) [318] with some modifications. 3

mg of the sterile-filtered lyophilized complex CDEX nanoparticles (75 kDa, 14 µmoles glycosyl units) were dissolved in 200 mL of a mixture of dry DMSO and dry pyridine 1:1 volume ratio. Then, dimethylaminopyridine (DMAP) was added to the solution at a final concentration of 3 mM. 11 mg (54 µmoles, 3.9-fold excess) of solid *p*-nitrophenylchloroformate (*p*-nPCOCl) was then added to the reaction mixture to activate CDEX, left at -20 °C in a sealed tube. By this reaction, *p*-nP was attached to the free hydroxyl groups of CDEX through carbonate bonds. After 17 h, to quantify *p*-nP covalently linked to CDEX, a 5 µL portion was mixed with 1 mL of ethyl acetate (EtOAc). Two methods [chromagenic and NMR, (NMR Bruker Avance III 500 MHz system, Bruker, USA)] confirmed that multiple glycosyl residues were activated by reaction of CDEX with *p*-NPCOCl. The solution was centrifuged, solvent decanted and centrifugation repeated, re-suspending with a second 1 mL of EtOAc, and supernatant again decanted. The pellet, CDEX-(*p*-nP)n was then dissolved in 1.0 mL of 0.1 M NaOH, and UV-Vis spectrum scanned in a quartz cuvette (250-600 nm), after 10x further dilution by UV-Vis spectrophotometer 8453, Agilent, Santa Clara, CA, USA.

b) Step 2 Stable anchor-peptide conjugation to CDEX

The bulk reaction (0.038 µmol CDEX, 4.75 µmol *p*-nP groups) was quenched with 2 mL of EtOAc, the white suspension was centrifuge (14,000 g, 1 min, RT) (Labnet Spectrafuge 24D Microcentrifuge, USA), solvent decanted, and pellet washed by re-centrifugation with 2 additional mL EtOAc. Pellet was dissolved in 200 µL DMSO, transferred to a 4 mL vial and subjected to rotary evaporation under high vacuum. Then, 2.8 µmol of the pyrrolidine-amido-PEG_8-peptide (TFA salt) was dissolved in 200 µL DMSO with 10.0 µmol of dry TEA (1 µL, 3.6-fold molar excess) and 0.038 µmol of Cy7 amine (from 20 mM stock in DMSO). This was added to the DMSO solution of dry CDEX-$(p\text{-nP})_{125}$ and the reaction sealed and heated at 45 °C, with orbital shaking (Elmi, Latvia) over 6 days. Reaction was then quenched at RT, with 20 µmoles of methoxy-PEG_4-amine at RT over 30 min. Then, the mixture was added dropwise to 2.5 mL of aqueous 0.2 M HCl solution. This was dialyzed against three 5 L changes of 0.1 mM HCl over 24 h, at RT, sterile filtered and lyophilized.

c) CDEX-peptide-conjugate characterization

Two methods were used to quantify the amount of peptide per particle, one was the quantification of tyrosine by UV (ʎ = 275 nm; ε_{Tyr} = 1,100 M^{-1} cm^{-1}) and by bicinchonic acid (BCA) colorimetric assay procedure, where the standard curves were based on BCA reaction of the free peptides. Cy7 attached to CDEX was quantified by Vis spectrum (ʎ = 750 nm; ε_{Cy7} = 199,000 M^{-1} cm^{-1}).

The particle size and the zeta potential (ζ) was measured by dynamic light scattering and electrophoretic mobility (n = 3) with a Zetasizer Nano ZSP, Malvern instruments, UK).

3.3.2 *In vivo diffusion experiment in rabbit vitreous*

a) Sample preparation

For the experiment, samples were dissolved in buffer phosphate (Sigma Aldrich, USA) 10 mM with NaCl 100 mM (Sigma Aldrich, USA) at pH of 7.2 ± 2. Final concentration 3 mg/mL (CDEX70-0 and CDEX70-3R) and 3, 6 and 12 mg/mL for CDEX70-2R. Samples were sterile-filtered.

b) Intravitreal injection

This utilized small 9-week old rabbits (1.8 kg, White New Zealand, Charles River Laboratories) to insure prone fit within the IVIS apparatus. Rabbits were anesthetized by an intramuscular (IM) mixture of ketamine hydrochloride (20-35 mg/kg) and xylazine hydrochloride (3-5 mg/kg), further local anesthesia was provided by additional propacaine. Topical instillation of the antimuscarinic agent tropicamide (Mydriaticum™) was also administered to obtain the mydriasis (pupil dilation) effect. The last step before injections was to flush the eyes with povidone for prophylactic local antisepsis.

To inject formulations, eyelids were retracted with a pediatric Barraquer wire speculum and the ocular bulbar conjunctivas were grasped at the lateral canthus via forceps to laterally rotate the globes towards the medial canthus. The needles tip, with their bevel directed backward were positioned on the lateral sclera 4 to 5 mm posterior to the limbus. Each eye was replaced to its natural position and a 31 gauge, 8 mm length needle (fixed to BD insulin syringe) was directed backward with an approximate angle of 45° and pushed through the sclera into the posterior ocular chambers towards the center of vitreous, until

the needle base just contacted the eye surface. Volumes of 30 µL were injected [CDEX-0, CDEX-3R and CDEX-2R 3 mg/mL (n = 3), CDEX-2R 6 mg/mL, CDEX-2R 12 mg/mL (n = 2)], n is the number of injected eyes. Needles were slowly withdrawn after the injections and the scleral conjunctiva were slightly compressed with the forceps tip to avoid any release of the injected material. The last step was to add on the eyes ointment at the end of the procedure. Intramuscular yohimbine (0.2-1 mg/kg) was used to reverse the effects of ketamine and xylazine (1 mL syringe, 25- or 27-gauge needle).

c) Imaging

Prior to imaging, rabbits were anesthetized by IM injection using ketamine/ xylazine. Eyes were kept open using a lid speculum for the duration of the imaging procedures. The imaging only took less than 1 min, with eyes only opened in the IVIS chamber <45 s. However, to avoid drying of cornea, ophthalmic solution eyewash (Akorn Animal Health, Lake, Forest, IL) was added to moisten the eyes before imaging. The fluorescence signal intensity in the rabbits were imaged on an *in vivo* imaging system (IVIS; Xenogen IVIS Spectrum; Caliper Life), over 52 days post-injection, first scan always at day 10 to allow IVT distribution. Animals were imaged for fluorescent emission intensity, the IVIS system being set to 745 nm excitation, and 800 nm for emission.

3.4 Synthesis of prodrug bridges between peptides and nanocarrier Boc-N-R-O-spacer-aa-O-tbut

There were several variables in the ester bridges used in this project. On the left hand side of the exemplary molecule shown below, different types of amino-alkoxy compounds were used (pyrrolidine-3-ol in this case), in order to explore the effects of different types of amino-alcohol (primary or secondary, cyclic, exocyclic) on the rate of spontaneous ester hydrolysis under physiological conditions, modeling release of peptides in the eye. The difference on the right hand side of molecules corresponds to the sequence of the active anti-angiogenic peptides that have been developed on this project. The spacers [dicarboxylic acid with chain of 5 (glutaric acid) or 6 (adipic acid) carbons] and the amino acids (sarcosine or glycine) are part of the active peptides sequences. Two different routes were used depending on whether an N-protected amino bromide compound or an N-protected amino alcohol compound were used as starting material (Figure 21).

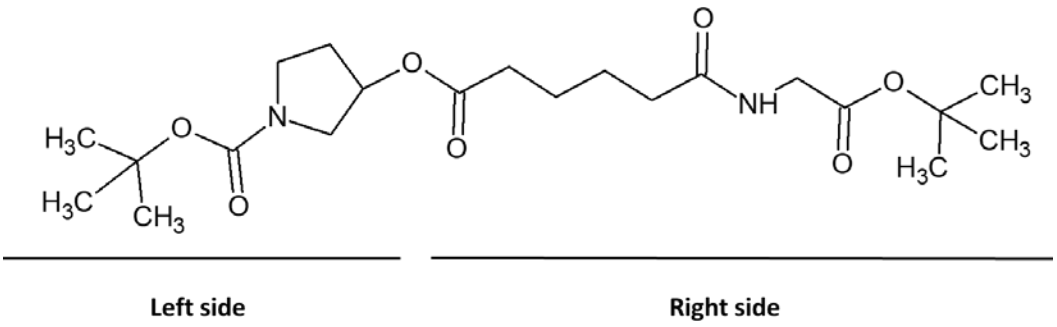

Figure 21. Example of a "Boc-N-R-O-spacer-aa-O-tbut" prodrug bridge; Boc-3-pyrrol-O-adp-Gly-O-tbut. In this case, the Boc-amino-alkoxy compound (Boc-N-R-O-) corresponds to *N*-Boc-3-hydroxy-pyrrolidine. The spacer is the adipic acid alkyl chain (-spacer-) and protected amino acid corresponds to glycine protected its carboxylic acid with tert-butyl (Gly-O-tbut).

Synthesis reactions of the intermediates are described in the supplementary section.

3.4.1 *Synthesis of the ester compound through phase transfer reaction of cmpd (2) or (4). (5-7)*

For this case, we have used the method described by Sam and Simmons (1973) [319] where an alkyl bromide reacts with the potassium carboxylate salt to obtain an ester bond. 0.1 mEq of the cmpd 2 or cmpd 4 and 10 µEq of 18-crown-6 (phase transfer catalyst) were dissolved in a mixture of dimethyl sulfoxide: toluene 2:8. The mixture was reacting under stirring at 40 °C. After 30 min, 0.11 mEq of the Boc amino bromide compound was added. After 18 h the reaction became cloudy from KBr precipitate, and was dried under vacuum. The crude product was washed in a separation funnel with water: chloroform. The organic phase was purified by column chromatography (ColCh) with a mixture of n-hexane: chloroform: methanol. The Boc-amino bromide compounds are shown in Table I (Figure 22).

Table I. Boc-amino alkyl bromides

Name	**Structure**
tert-butyl (4-bromobutyl)carbamate	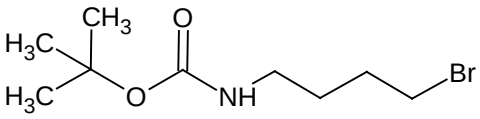
tert-butyl 3-bromopyrrolidine-1-carboxylate	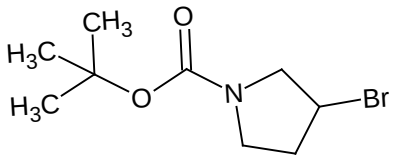
tert-butyl 4-bromopiperidine-1-carboxylate	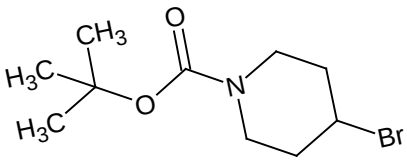

There were three compounds (below) for which we used the above alternative synthetic route to attach chromophoric carboxamides to aid in kinetic monitoring of ester hydrolysis, by HPLC.

For example, cmpd 13 is a chromophoric glutaryl-sarcosine amide, which can be amide, bound to adipic or glutaric esters (left side) of *N*-blocked amino alcohols to enable facile observation of chromophore detachment following ester hydrolysis.

3.4.2 *Synthesis of Boc-amido-alkoxy esters through transesterification of cmpds (1), (3) or (13). (14-20)*

The method described by Hatano *et al.* (2013) [320] was used to synthesize these compounds. 0.1 mEq of cmpd 1 or cmpd 13 was dissolved in toluene. The reaction was stirred at azeotropic reflux, mixed with a 6% of trioctylphosphine dimethylcarbonate and a 3% of lanthanum (III) nitrate and 0.15 mEq of the desired Boc amino alkoxy compound (see Table II). After 6 h the reaction was complete. The mixture was dried under vacuum and purified by ColCh with a mixture of n-hexane: chloroform: methanol. Boc-amino alkoxy compounds are shown in Table II (Figure 22).

Table II. Boc-amido alcohols attached to adipic Gly-t-But or to glutaric-Sar-t-But

Name	**Structure**
tert-butyl [2-(2-hydroxyethoxy)ethyl] carbamate	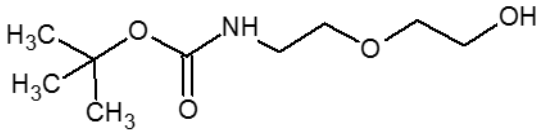
tert-butyl (trans-4-hydroxycyclohexyl) carbamate*****	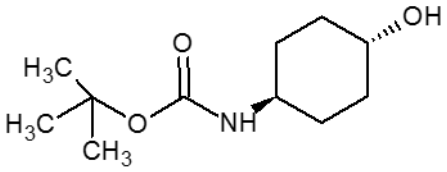
tert-butyl [(1S,2S)-2-hydroxycyclopentyl] carbamate	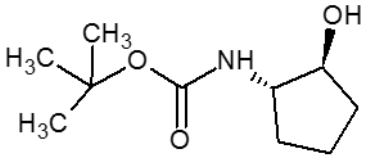
tert-butyl [(1R,3R)-3-hydroxycyclopentyl] carbamate	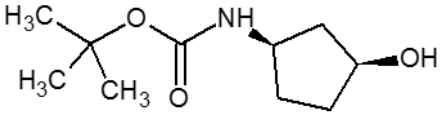
tert-butyl (cis-4-hydroxycyclohexyl) carbamate	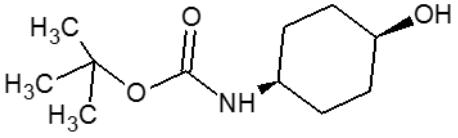
tert-butyl {2-[(4-hydroxypentanoyl) amino]ethyl}carbamate (8)	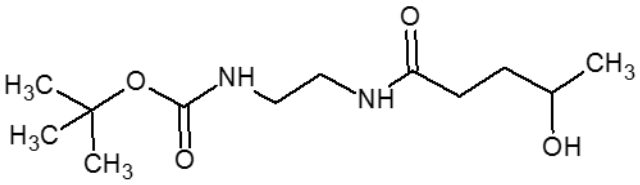

*****With this compound two ester bridges were synthesized; one with the adp-Gly sequence and the other with the glt-Sar sequence.

tert-butyl (cis-4-hydroxycyclohexyl) carbamate	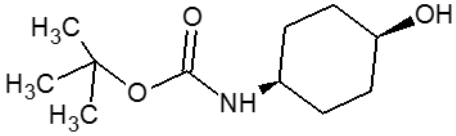

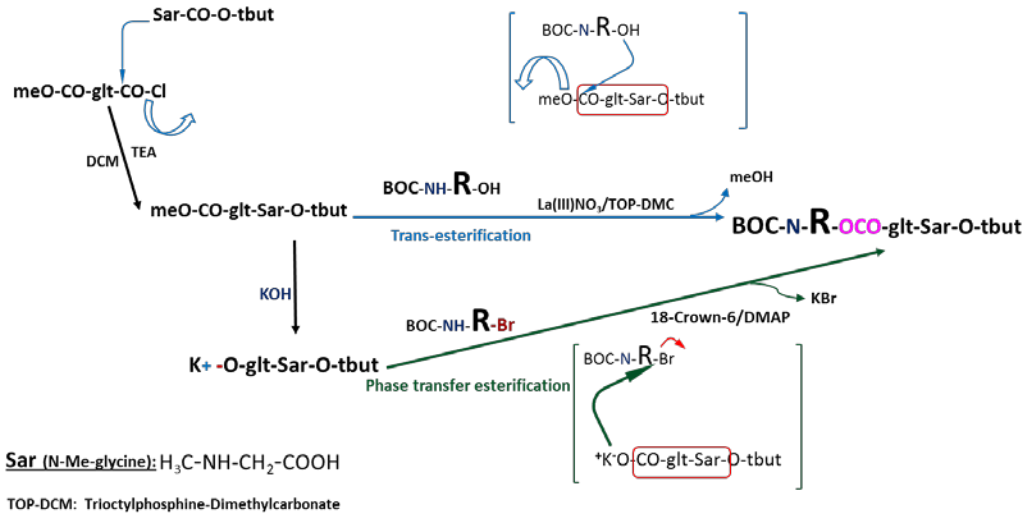

Figure 22. Boc-amidoalkoxy esters via transesterification or phase transfer displacement of bromides.

3.4.3 *Ester hydrolysis testing*

Aminoalkoxy-ester compounds were dissolved in a solution of ethanol. These solutions were diluted with (4-(2-hydroxyethyl)-1-piperazineethanesulfonic acid) (HEPES) buffer 0.1 M (pH: 7.5 ± 0.17) to a known concentration (0.1-1.0 mM). The solutions were incubated at 37 °C and time point samples evaluated by HPLC with a diode array detector (Agilent 1,100, Agilent, Santa Clara, CA, USA in different times. [Column: Zorbax SB-C_{18} 5 µm 150 x 4.6 mm, Agilent, Santa Clara, CA, USA. Mobile phase: Water (0.1% TFA):ACN 85:15 (0-5 min), Water (0.1% TFA):ACN 10:90 (15 min), Water (0.1% TFA):ACN 0:100 (17-20 min). Method time: 25 minutes. Volume of injection: 20 µL. Wavelength: 205 nm].

3.4.4 *Comparison of the behavior of the ester degradation*

To compare the effect of the dicarboxylic chain on the ester hydrolysis rate on the right hand side of the molecules (adp-Gly *vs* glt-Sar) two model peptides were designed with a methyl ester bond, the shortest one, followed by the alkyl chain, adp or glt, preceding the same amino acid sequence (-Sar-GYNLYRVRS-amide) with the aim to improve the solubility and enhance with Tyr absorbance the sensitivity of the analytical method. The two peptides were dissolved in buffer HEPES 20 mM, 0.01% w/v azide, pH 7.4 and incubated at 37 °C. The solutions were checked by HPLC [Column: Zorbax SB-C18 5 µm

150x4.6 mm. Mobile phase: H_2O (0.1% TFA):ACN 85:15 (0-5 min) to H_2O (0.1% TFA):ACN 70:30 (55-60 min). Method time: 60 minutes. Volume of injection: 20 µL. ʎ = 205 and 230 nm].

3.5 Boc-N-R-O-ahx-DNP. A simple model system to rapidly evaluate ester hydrolysis rates

In order to evaluate amino-ester prodrug candidates, for spontaneous hydrolysis half-lives before being able to make the peptide versions, we utilized a simpler chromogenic model compound system, where hydrolysis products are readily quantified by HPLC. While environmental carboxylic esters have had aqueous breakdown rates compared in water [321], we are not aware of any published systematic comparison of ester hydrolysis as a function of alcohol structure. Since we found that direct ester linkage to polymeric carbohydrates or OH-dendrimers was low in yield and did not give very stable esters, our particular focus was on amino-bridged esters, thus the hydrolysis kinetics of esters of *N*-blocked amino alcohols. The scant simple hydrolysis data suggested that esters of secondary alcohols, especially those exocyclic on 5 or 6 membered rings, were more slowly hydrolyzed than esters of primary alcohols [321].

We therefore began systematic comparison of the rate of hydrolysis under physiological conditions, of amino-alkoxy esters. We thereby hoped to find a range for tuning the rate of drug release from amino-bridged prodrugs. Below are the amino alcohol structures we examined after esterification to chromogenic hexanoic acid in the form of dinitrophenyl-ε-amino-n-caproic acid (DNP). All give the same product, the starting DNP upon hydrolysis, simplifying HPLC measurement.

3.5.1 *Amino alcohol structures candidates*

After the first ester hydrolysis rate study with the Boc-N-R-O-spacer-aa-O-tbut compounds, we selected four amino–alkoxy compounds to synthesize these Boc-N-R-O-ahx-DNP, one fast released compound, one medium released compound and two slow released compound (data in Results, Table V).

0.1 mEq DNP was reacted in toluene at 80 °C under stirring with DMF (catalytic amount). When the temperature had reached 80 °C, 0.1 mEq of thionyl chloride and 50 µEq of pyridine were added to the reaction. The reaction was followed by thin layer

chromatography (TLC) (DCM: MeOH; 9:1). After 2 h the starting material was disappeared so 0.11 mEq of the desired aminoalcohol were added to the reaction. The selected compounds were *tert*-butyl (4-hydroxybutyl)carbamate; *tert*-butyl 3-hydroxypyrrolidine-1-carboxylate; *tert*-butyl [(1*R*,3*R*)-3-hydroxycyclopentyl] carbamate and *tert*-butyl (trans-4-hydroxycyclohexyl) carbamate. After 12 h the reactions were completed. The crudes products were purified by ColCh with a mixture of DCM:MeOH (Figure 23).

Figure 23. Scheme of the synthesis pathway of the compounds Boc-aminoalkoxy-ester DNP.

3.5.2 Ester hydrolysis kinetic testing

DNP-ester compounds were pre-dissolved in DMSO and then, they were diluted in HEPES buffer 0.1 M at pH 7.4 at a known concentration (0.1-2 mM). The solutions were incubated at 37 °C and samples evaluated by HPLC at different times. [Column: Zorbax SB-C_{18} 5 µm 150 x 4.6 mm. Mobile phase: Water (0.1% TFA):ACN 70:30 (0-2 min); H_2O (0.1% TFA):ACN 10:90 (10 min), H_2O (0.1% TFA):ACN 0:100 (12-15 min). Volume of injection: 20 µL. Wavelength: 230 nm. The study was made by triplicate.

3.5.3 *Deprotection of the amines of Boc-amido-R-O-esters of ahx-DNP*

To attach the ester-DNP compound to a CDEX nanoparticle 0.1 mEq of Boc-N-X-O-ahx-DNP was deblocked by dissolution in a mixture of TFA 20% v/v in DCM at RT. After 24 h the reaction was complete. 20 volumes of toluene were added to the mixture and the sample was dried by rotary evaporation. The reaction was followed by TLC (DCM:MeOH; 9:1). The crude product was extracted in a separation funnel (DCM/ water), and aqueous phase freeze-dried to give the free amine cmpd (TFA salt). Final product: NH-X-O-ahx-DNP.

3.5.4 *Attachment of the DNP ester compounds to the nanogel CDEX.*

a) Step 1: activation of CDEX

3 mg of the sterile-filtered lyophilized complex CDEX nanoparticles (75 kDa, 14 µmoles glycosyl units) were dissolved in 200 mL of a mixture of dry DMSO and dry pyridine 1:1

volume ratio. Then, DMAP was added to the solution at a final concentration of 3 mM. 11 mg (54 µmoles, 3.9-fold excess) of solid *p*-nPCOCl was then added to the reaction mixture to activate CDEX, left at -20 °C in a sealed tube. By this reaction, *p*-nP was attached to the free hydroxyl groups of CDEX through carbonate bonds. After 17 h, to quantify *p*-nP covalently linked to CDEX, a 5 µL portion was mixed with 1 mL of EtOAc. The chromagenic method confirmed that multiple glycosyl residues were activated by reaction of CDEX with *p*-NPCOCl. The solution was centrifuged, solvent decanted and centrifugation repeated, re-suspending with a second 1 mL of EtOAc, and supernatant again decanted. The pellet, CDEX-(*p*-nP)n was then dissolved in 1.0 mL of 0.1 M NaOH, and UV-Vis spectrum scanned in a quartz cuvette (250-600 nm), after 10x further dilution by UV-Vis spectrophotometer.

b) Step 2. CDEX conjugation of the DNP ester compounds

Samples (mass: 4 mg) were quenched with 2 mL of EtOAc, the white suspension was centrifuged as above. As previously, solvent decanted, and pellet washed by re-centrifugation with 2 additional ml EtOAc. Then, 11.5 µmol of the NH-R-O-ahx-DNP (TFA salt) was dissolved in 200 µL DMSO with 13.3 µmol of dry TEA (1 µL, 3.6-fold molar excess). This was added to the DMSO solution of dry CDEX-(*p*-nP)$_{57\text{-}154}$ and the reaction sealed and heated at 45 °C, with orbital shaking over 3 days. Reaction was then quenched at RT, with 20 µmoles of ethanolamine at RT over 30 min. Then, the mixture was added dropwise to 2.5 mL of aqueous 0.2 M HCl solution. This was dialyzed against three 5 L changes of 0.1 mM HCl over 24 h, at RT, sterile filtered and lyophilized.

3.5.5 *Characterization of the nanocarriers*

The method used to quantify the amount of model-ester-DNP compound was by UV-Vis (λ = 360 nm, ε_{DNP}: 16,622 M^{-1} cm^{-1}).

The particle size was measured by dynamic light scattering (n = 3) with a Zetasizer Nano ZSP.

3.5.6 *In vitro release studies of DNP-ester compounds from CDEX*

CDEX70-N-R-O-ahx-DNP compounds were dissolved in buffer HEPES 20 mM [SDS 0.1% (w/v) azide 0.02% (w/v)] pH 7.4 and storage in glass vials at 37 °C. To analyze them,

one aliquot was filtered through a centrifuge filter [MWCO: 3 kDa, (Amicon, EMD Millipore, Burlington, MA, USA) speed: 14,000 g, RT, 10 min]. Then the filtered was collected and checked by UV (ʎ = 360 nm). These measurements were made in triplicate.

3.6 *In vitro* and *in vivo* release studies of prodrugs from CDEX

The prodrug synthetic pathway was overcome with a new strategy whereby the protected amino-alcohol, *N*-Boc-pyrroliidin-3-ol is reacted to form its ester with a large excess of adipic di-acid chloride, all acid chlorides being subsequently quenched with aqueous bicarbonate. Careful acidification to pH 3-4 then preserves the Boc protecting group while enabling organic phase extraction of the ester, while adipic acid and its salts remain in the water phase (detailed below). The 3-Boc-pyrrolidinol adipic half ester is then used to cap the growing peptide linked to solid state resin.

3.6.1 *Synthesis of the peptide prodrug*

With the drug candidate (peptide 11: COOH-adp-Sar-YNLYRVRS-amide) and the amino-alkoxy compound (*tert*-butyl 3-hydroxypyrrolidine-1-carboxylate) chosen, the ester was synthesized using a new route.

Synthesis of 6-{[1-(tert-butoxycarbonyl)pyrrolidin-3-yl]oxy}-6-oxohexanoic acid (21)

3 mEq of adipic chloride were dissolved in 10 mL of DCM at RT under stirring. At the same time 1 mEq of the amino-alkoxy compound was dissolved in DCM with 1 mEq of TEA. This solution was added to the first one dropwise. After 30 min of reaction, the mixture was dried under vacuum and the crude product was dissolved in a solution of sodium bicarbonate 1 M. The solution was washed with EtOAc, and both phases were mixed in a separation funnel. After extraction and EtOAc removal, the aqueous phase pH was adjusted with HCl 1 M to pH 4. Then, the solution was mixed with ethyl ether and the organic phase was isolated. The organic phase was dried under vacuum. Final product: Boc-3-pyrrol-O-adp-COOH (Figure 24).

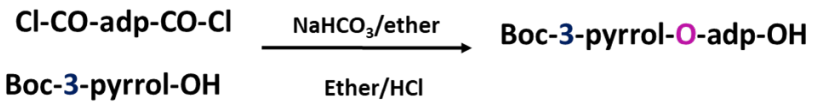

Figure 24. Scheme of the synthesis pathway to get aminoalkoxy-ester bridge.

Synthesis of the ester prodrug 3-pyrrolidine-O-adipic-N-Sar-Tyr-Asn-Leu-Tyr-Arg-Val-Arg-Ser-amide (22)

To HN-Sar-YNLYRVRS on Rink MBHA resin in DMF was added 1.5 mEq of Comp 1, 1.45 mEq (1-[Bis(dimethylamino)methylene]-1*H*-1,2,3-triazolo[4,5-b]pyridinium 3-oxid hexafluorophosphate) (HATU), and 6 mEq of DIPEA. The reaction mixture was shaken on a mechanical shaker overnight (16 h) at RT. The resulting peptide was cleaved from the resin using a mixture of 95% TFA, 2.5% water, and 2.5% triisopropylsilane for 3 h. Crude peptide was precipitated from this solution using cold diethyl ether before purification by HPLC. Final product: 3-pyrrol-O-11 peptide (Figure 25).

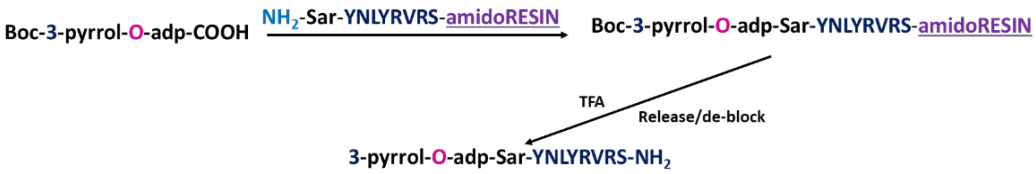

Figure 25. Scheme of the solid-state reaction and deblocking of 3-pyrrol-O-11 peptide.

3.6.2 *Conjugation of the prodrug peptide with CDEX*

Following the same procedure as the explained above for the CDEX70 activation with *p*-nPCOCl, the sample (mass: 2.3 mg) was quenched with 2 mL of EtOAc, the white suspension was centrifuged as above, solvent decanted, and pellet washed by re-centrifugation with 2 additional mL EtOAc. Pellet was dissolved in 200 µL DMSO, transferred to a 4 mL vial and subjected to rotary evaporation under high vacuum. Then, 5.4 µmol of the pyrrolidine-ester-11 peptide prodrug (TFA salt) was dissolved in 200 µL DMSO with 16.9 µmol of dry TEA (2.36 µL, 3.6-fold molar excess). This was added to the DMSO solution of dry CDEX-(*p*-nP)$_{108}$ and the reaction sealed and heated at 45 °C, with orbital shaking over 3 days. Reaction was then quenched at RT, with 20 µmoles of *m*-PEG$_4$-amine at RT over 30 min. Then, the mixture was added dropwise to 2.5 mL of aqueous 0.2 M HCl solution. This was dialyzed against three 5 L changes of 0.1 mM HCl over 24 h, at RT, sterile filtered and lyophilized.

3.6.3 *Characterization of CDEX70-3-pyrrol-O-11 peptide*

The average amount of peptide conjugated to CDEX was quantified by UV because the presence of the amino acid tyrosine (λ = 275 nm; ε_{Tyr} = 2,200 M^{-1} cm^{-1}) and BCA. Samples

were dialyzed and weighted, and then they were dissolved in a known amount of water. The same procedure was followed to prepare the standard curves of the peptides.

The size of the particles and the ζ of the compounds in water were analyzed in triplicate by dynamic light scattering and electrophoretic light scattering respectively (Zetasizer Nano ZSP).

3.6.4 *Stability test of the prodrug 3-pyrrol-O-11 peptide*

The aim of this experiment is to demonstrate the peptide prodrug does not suffer chemical alterations in the ester bond with the reagents during the conjugation reaction in the NP. The prodrug was tested by HPLC by itself, with the conjugation reaction conditions (nitrogen atmosphere, shake: 100 rpm, temperature: 45 °C, time: 3 d in presence of *p*-nP-OH, DMSO and TEA. In addition, the prodrug peptide was mixed in the conditions of the quench step (DMSO, *m*-dPEG®$_4$-amine, temperature: RT, time: 1 h). The samples were checked by HPLC [Column: Zorbax SB-C18 5 µm 150x4.6 mm. H_2O (0.1% TFA):ACN 85:15 (0-5 min) to H_2O (0.1% TFA):ACN 70:30 (55-60 min). Method time: 60 minutes. Volume of injection: 20 µL. ʎ = 230 nm.

3.6.5 *In vitro rate of adipic peptide release from CDEX70-3-pyrrol-O-11 peptide*

1.43 mg of the nanocarrier was incubated in physiological conditions; 1 mL of phosphate buffer 10 mM and NaCl 100 mM pH 7.43. Temperature: 37 °C.

Three aliquots were taken on different days and the released peptide (11 peptide) was separated by centrifugal filtration (MWCO: 10 kDa, 14,000 g, 10 min, RT). The filtered were checked by UV (ʎ = 275 nm) and by HPLC. The filtrate was compared with the peptide 336 as reference standard (concentration: 100 µg/mL in water). [Column: Zorbax SB-C18 5 µm 150x4.6 mm. H_2O (0.1% TFA):ACN 85:15 (0-5 min) to H_2O (0.1% TFA):ACN 70:30 (55-60 min). Method time: 60 min. Volume of injection: 20 µL. ʎ=230 nm].

3.6.6 *In vivo CNV efficacy of the peptide 11 released from CDEX70-3-pyrrol-O-11 peptide injected IVT in mice*

To study the efficacy of the formulation. The nanocarrier was dissolved in water and the pH was adjusted to 7.2 with NaOH 0.1 M. The sample was lyophilized. Then, the freeze-dried was dissolved in a solution of NaCl 100 mM pH 7.2 ± 2 getting the peptide final concentration of 1 mg/mL. A sample of free peptide 336 was prepared at the same concentration, 1 mg/mL following the same steps as the nanocarrier sample. As negative control was used the vehicle, the solution of NaCl 100 mM pH 7.2. All the samples were filtered by 0.2 μm.

The experimental system used on this study was the Laser-induced CNV according to the protocol described by Nourinia et al, 2015[322]. 20 C57BL/6J mice were used for this experiment. 2 μL of the samples were injected intravitreally 15 d before the induced damage of the Bruch's membrane via laser. 15 d after the laser induction, 30 d after the injection, animals were euthanized and the eyes were enucleated and fixed in 4% paraformaldehyde at 4 °C for 2 h. To get the posterior sclerochoroidal eyecup, eyes were placed in phosphate-buffered saline (PBS) and sectioned at the equator by a stereoscopic zoom dissecting microscope (LABOMED, Luxeo 4Z number 444000; Nightingale Sales, Inc., Fort Myers, FL, USA). After 1 h of incubation in blocking buffer (20% fetal calf serum, 20% normal goat serum, and 0.01% Triton X-100 in PBS) at RT, the posterior eyecups were incubated with anti–intercellular adhesion molecule (ICAM)-2 (1:500 in blocking buffer, catalog N°. 553326; BD Biosciences, San Jose, CA, USA) overnight at 48 °C. The samples were then washed three times with PBS and incubated with the Cy-3 anti-rat secondary antibody (1:500 in blocking buffer; catalog N°. 712-165-153; Jackson ImmunoResearch, West Grove, PA, USA) for 2 h. Finally, the posterior eyecups were flattened by 5 to 6 relaxing radial incisions and mounted on a glass slide with VectaMount AQ (Vector Laboratories, Malvern, PA, USA). The CNV images were captured with an inverted microscope (Olympus TH4- 200; Olympus, Tokyo, Japan) fitted with appropriate excitation and emission filters (Olympus U-RSL-T) and equipped with a digital camera (Olympus U-TV0.63xc). ImageJ software (ImageJ 1.48, http://imagej.nih.gov/ij/; provided in the public domain by the National Institutes of Health, Bethesda, MD, USA) was used to quantify the total area of CNV associated with each laser burn. The statistical analysis was one-way ANOVA between CDEX70-3-pyrrol-O-11 vs vehicle; CDEX70-3-pyrrol-O-

11 vs peptide 11 and peptide 11 vs vehicle. P value less than 0.05 was considered statistically significant.

Results

4.1 *In vivo* diffusion experiment in rabbit vitreous

4.1.1 *CDEX activation and peptide conjugation*

The activation of CDEX with *p*-nPCOCl was checked by two different techniques (chromagenic and NMR). Assuming that there were 365 free hydroxyl groups on the surface of CDEX, the *p*-nitrophenolate spectrum was observed by more than of 1/3 of the OH groups have been activated. ^{1}H-NMR, showed the presence of *p*-nP attached to CDEX through a carbonate bond. Two different compounds were compared by ^{1}H-NMR, the conjugate CDEX-*p*-nP [^{1}H NMR (500 MHz, DMSO-d_6) **δ 8.26-8.18 (m, 2H), 7.51-7.42 (m, 5H),** 6.45 (s, 1H), 5.52 (s, 1H), 5.46 (s, 1H), 5.31 (s, 1H), 5.21 (s, 1H), 5.02 (s, 3H), 4.90 (s, 1H), 4.83 (s, 3H), 4.76 (s, 1H), 4.61 (s, 3H), 4.40 (s, 6H), 3.67 (s, 6H), 3.55 (s, 3H), 3.28 (d, J = 6.1 Hz, 1H), 3.22 (s, 2H), 3.13 (s, 6H), 2.25 (s, 3H), -0.14 (s, 2H); and *p*-nP-

OH itself [^{1}H NMR (500 MHz, DMSO-d_6) **δ 8.18-8.09 (m, 2H), 6.97-6.90 (m, 2H)**]. The aromatic signals of the *p*-nitrophenyl group did not appear in the same magnetic field as they did in *p*-nitrophenol.

An UV-Vis absorbance spectrum of the 3R-NPC in water at 1.0 mg/mL is shown in Figure 26. A peak at 275 nm, not present in unconjugated NP, is from a single tyrosine in each peptide. The minimum height of this peak, subtracting only the high background scattering at 300 nm, leads to calculation of at least 27-30 peptides/ NP, based on peptide molar extinction of 1,100 at 275 nm. However, this is a minimum estimate since light scattering goes up sharply and indeterminately at lower wavelength. Correction to the baseline of a spectrum of similarly activated but only PEG-amine quenched CDEX (CDEX-70-0), estimates approximately 60 peptides per NPC but is uncertain as particle size varies. Thus, UV spectrum is only a rough measure of peptide load. Tyr spectrum assay will be reliable only after trace large particles are removed through gel filtration. More accurate peptide load determination on weighed samples was accomplished by the same BCA colorimetric assay procedure described previously, where standard curves were based on BCA reaction of the free peptides. Cy7 attached to CDEX was quantified by Vis spectrum (λ = 750 nm; ε_{Cy7} = 199,000 M^{-1} cm^{-1}) as seen in Figure 26.

This showed the number of peptides linked per particle for the three nanocarriers (CDEX70-0, CDEX70-2R and CDEX70-3R) were 0, 64 and 61 respectively. Thus, the number of positive charges, derived exclusively from Arg residues per NP/NPC were 0, 128 and 183. The measured ζ of the conjugates increased with the number of positive charges per particle (CDEX70-0: -0.61 ± 0.1 mV, CDEX70-2R: 3.9 ± 0.9 mV, CDEX70-3R: 6.34 ± 1.3 mV) and particle size was CDEX70-0: 150 nm, CDEX70-2R: 85 nm, CDEX70-3R: 82 nm. Properties of the NP/ NPC are summarized on Table VI.

NP/NPC diameter and ζ were measured by dynamic light scattering and electrophoretic mobility (n = 3) with a Zetasizer Nano ZSP. Percent CDEX mg recovered was based on the total mg of CDEX used, corrected to the theoretical added masses of peptide and PEG_4-amine. Lower yield in unconjugated CDEX (PEG_4-amine only) may reflect multimeric aggregates lost on sterile-filtration, since NP without peptides are not cationic, thus not self-repelling. We attribute the smaller diameters of cationic conjugates to mutual charge repulsion preventing self-association, presuming CDEX without peptides to have trace contamination with multimeric NP/ MP. Based on the extinction coefficient of Cy7, the

amount of dye attached to the nanoparticles was less than 0.3 dye molecules/NP. This low level was sufficient to study the diffusion of tagged NP in vitreous while unlikely to perturb diffusion, the dye being uncharged and <0.5% of any NP/ NPC mass (100-160 kDa). Table VIII.

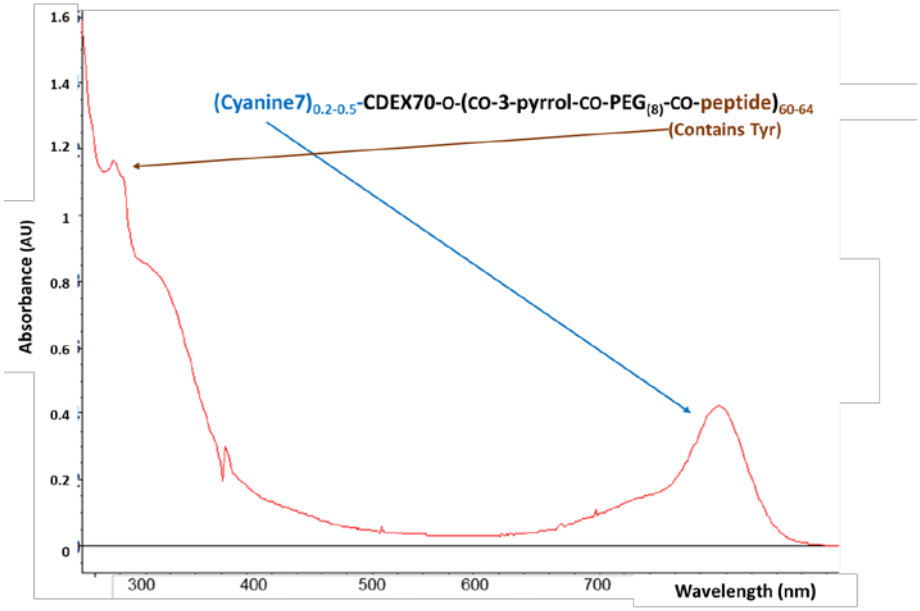

Figure 26. UV-VIS spectrum of a 3Arg peptide and the Cy7 dye conjugated to the nanocarrier (Cy7-CDEX70-3-pyrrolidine-CO-PEG_8-RRYRL-NH_2). ʎmax tyrosine of peptide = 275 nm, 67 peptides per particle of CDEX; ʎmax Cy7 = 750 nm, <1 dyes per particle of CDEX.

Table VIII. Physicochemical characteristics of the NP and NPC

NP or **NPC**	**Pept/CDEX**	**Positive charges/CDEX**	**ζ (mV)**	**Cy7/CDEX**	**Particle diam. (nm)**	**% CDEX mass recovered**
Cy7-CDEX	0	0	-0.6±0.1	0.16	150±2	50
Cy7-CDEX-R2	64	128	+3.9±0.9	0.24	85±15	80
Cy7-CDEX-R3	61	183	+6.3±1.3	0.28	82±7	90

Characterization and measurement of the NP and NPC by dynamic light scattering and electrophoretic mobility (n = 3). Number of peptides per particle of CDEX; the quantification of peptide was determined by BCA. Number of molecules of Cy7; the quantification of cyanine 7 was determine also by absorbance (EC_{Cy7} = 199,000 M^{-1} cm^{-1}).

4.1.2 *In vivo clearance from rabbit vitreous is surface charge (ζ)-dependent*

For the *in vivo* diffusion-dependent loss study, the images of the photons per area of the posterior part of the rabbit eye have checked by fluorescence at excitation: 745 nm, emission: 800 nm in a defined circular area surrounding the rabbit eye facing upward. Each rabbit eye received 30 µL, by intravitreal injection, of one of the three samples [Cy7-CDEX70-0, Cy7-CDEX70-2R, Cy7-CDEX70-3R; concentration = 3 mg/mL, (90 µg total polymer mass)]. All data were corrected against the autofluorescence background signal of the vitreous. After the injection, 10 days were waited to let the particles distribute around the whole vitreous. The day 10 was marked as time 0 for subsequent clearance. The loss of the Cy7-tagged NP particles was followed over 6 weeks beyond day 10 (taken as day 0 for clearance analysis). The change of fluorescence intensity for exemplary individual rabbit eyes is shown on Figure 27. This illustrates how individual eyes injected with equal amounts of Cy7-tagged NP can be repeatedly imaged over 1 to 3-week periods for estimation of emitted photon/s, a measure of ocular NP retention since dye is linked as a stable carbamate (urethane) bond. The rate of loss (diffusion) of the three conjugates was in the following order: CDEX70-0 >CDEX70-2R >CDEX70-3R. The half-life of CDEX70-0 (control) in the vitreous was less than 3 days. The half-life of CDEX70-2R was 7 days over which time, the average remained of CDEX70-3R was 65%. While the half-life of CDEX70-3R was 17 days (range between 14-21 days) (Figures 28 and 29).

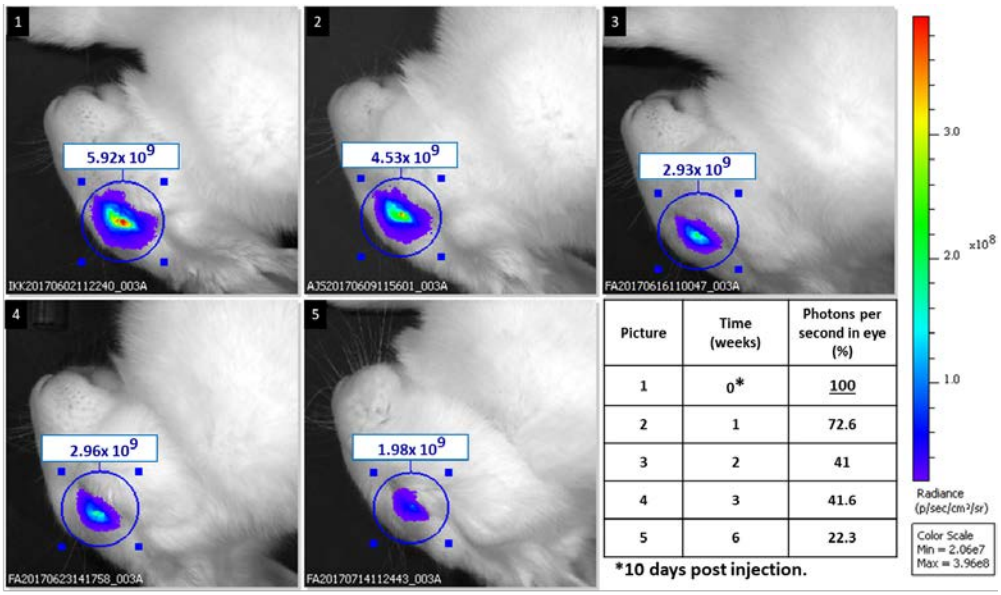

Picture	Time (weeks)	Photons per second in eye (%)
1	0*	100
2	1	72.6
3	2	41
4	3	41.6
5	6	22.3

*10 days post injection.

Figure 27. Rabbit eye imaging by IVIS of a single exemplary eye injected the sample Cy7-CDEX-3R followed over 5 weeks. Measurement of number of photons per area (excitation: 745 nm; emission: 800 nm). Line A: IVIS scan of the rabbit eye with Cy7-CDEX70-3R. The picture number 1 is the first scan after 10

days post injection. This measurement is marked as time 0. The Table shows the percentage of photons remained in the eye during the study after the correction substracting the autofluorescence background. The 50% was achieved after 3 weeks.

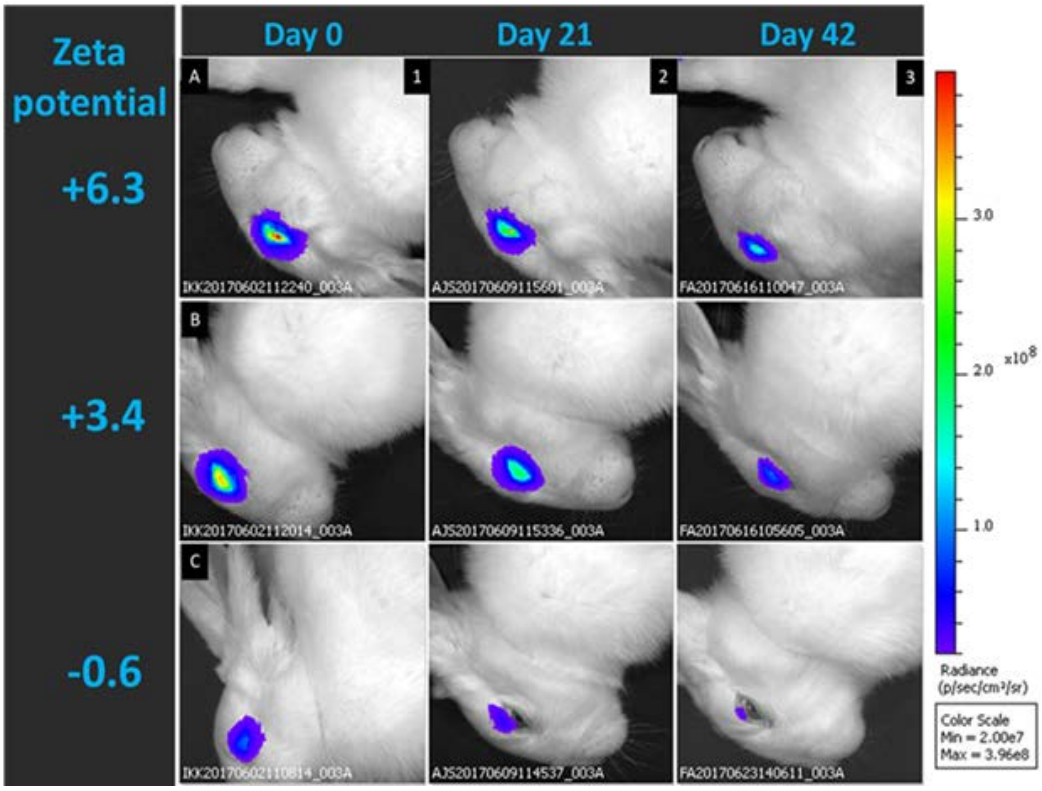

Figure 28. Rabbit eye imaging by IVIS. Measurement of number of photons per area (excitation: 745 nm; emission: 800 nm). **Line A:** IVIS scan of the rabbit eye with Cy7-CDEX70-3R. **Line B:** IVIS scan of the rabbit eye with Cy7-CDEX70-2R peptide. **Line C:** IVIS scan of the rabbit eye with Cy7-CDEX70-0 peptide. **Row 1:** IVIS scan after 10 days post injection. This measurement is marked as time 0. **Row 2:** IVIS scan after 3 weeks experiment. **Row 3:** IVIS scan after 6 weeks experiment. 3R peptide conjugate is seen to be retained longer in the eye compared with 2R peptide conjugate at similar peptide loading. Spreading and loss of fluorescence was slowed in more highly charged NPC.

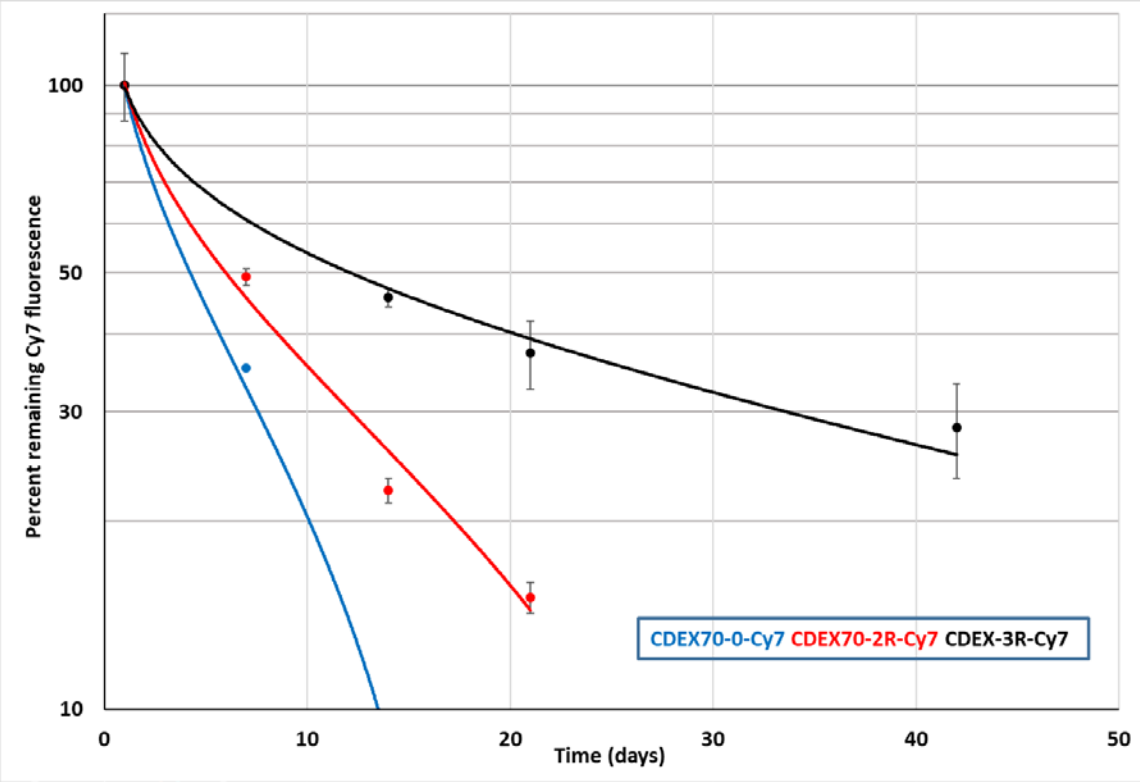

Figure 29. ***In vivo*** **charge and ζ -dependent loss of NP from rabbit vitreous expressed as a percentage of the first measured photon flux at day 10 post-injection (taken as day 0).** Volume of injection: 30 µL; nanocarrier concentration: 3 mg/mL. [Control: CDEX70-0: (n = 2). CDEX70-2R; 64 peptides per particle by BCA (n = 3) and CDEX70-3R; 61 peptides per particle by BCA (n = 3)]. Half-lives: CDEX-0: 4 days; CDEX-2R: 7 days; CDEX70-3R: 13 days. 2R and 3R peptides linked as carbamates of 3-pyrrolidine-CO-amido-PEG_8-CO-peptide to Cy7-CDEX70. Cy7 amine was carbamate-linked at <1 mol/mol NP.

4.1.3 *In vivo loss from rabbit vitreous is concentration dependent*

Four different concentrations of the same nanocarrier were tested to compare the total retention capacity of the polymer dose. The results corresponded to the same nanocarrier (CDEX70-2R) in three different concentrations [Control: 0 mg/mL (n = 6), 3 mg/mL (n = 3), 6 mg/mL (n = 2) and 12 mg/mL (n = 2)]. As in the previous experiment, we checked the fluorescence in the vitreous at a specific wavelength excitation: 745 nm, emission: 800 nm. The results were corrected to the background fluorescence from 0 mg/mL (vehicle injection). The measurement started 10 days post injection, considering this time point as 100% of remained nanocarriers in the vitreous. The measurements were 0 mg/mL ($0.85x10^9$ p/s), 3 mg/mL ($7.20x10^9$ p/s), 6 mg/mL ($16.13x10^9$ p/s) and 12 mg/mL ($4.95x10^9$ p/s), the last being much lower than an expected value near 25-30 $x10^9$ p/s. The fluorescent intensity of the samples at 3 mg/mL and 6 mg/mL were proportional to total dose and both

samples kept the proportion during the entire study. The sample at 12 mg/mL (a dose of 360 µg total) had lower intensity than 3 mg/mL (90 µg) at day 10. After 14 additional days, the percentage remained of CDEX in the vitreous was for the 3 mg/mL sample $2.25x10^9$ p/s; (22%), for the 6 mg/mL sample $5.75x10^9$ p/s; (32%), both consistent with 7-day half-life. For the 12 mg/mL sample, $2.84x10^9$ p/s; (49%), but only 14% of the total flux expected in proportion to the two lower doses. All the samples were eliminated from the vitreous after 21 additional days of study (5 weeks), for the 3 mg/mL sample $1.79x10^9$ p/s, for the 6 mg/mL sample $1.79x10^9$ p/s and for the 12 mg/mL sample $1.48x10^9$ p/s (Figure 30).

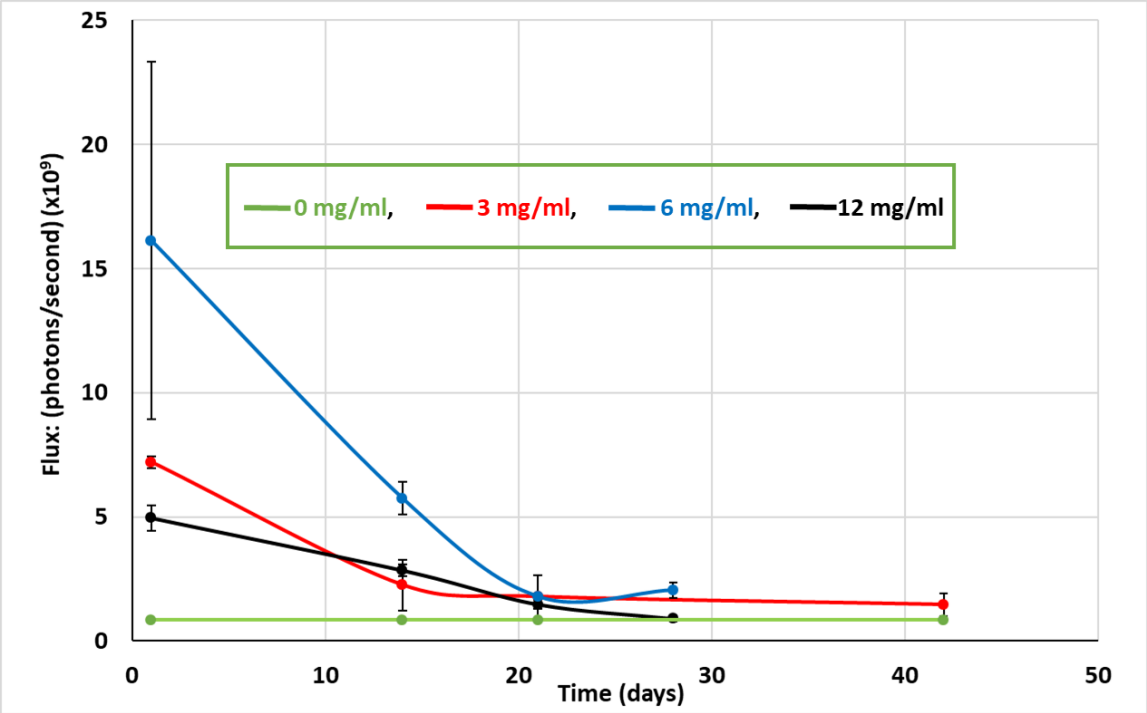

Figure 30. Initial dose dependence of *in vivo* loss of nanocarriers from rabbit vitreous expressed as fluorescent photon flux, compared to the first measurement at day 10 post-injection of 20 µL, (taken as day 0) of Cy7-CDEX70-2R (64 peptides per particle) at 4 different concentrations, [Control: 0 mg/mL (n = 6), 3 mg/mL (n = 3), 6 mg/mL (n = 2) and 12 mg/mL (n = 2)]. This indicates consistent slowing of nanoparticle loss up to 300 µg injected 2R conjugates, but large initial loss, implying binding capacity is exceeded at 600 µg in 2 mL rabbit eye.

4.1.4 *Safety evaluation*

Eye globes were enucleated, and immediately fixed in formalin and prepared for histology. Paraffin sections were stained with hematoxylin/eosin and examined for structural abnormalities and signs of inflammatory infiltrations in masked fashion. The study eyes were submitted for routine, masked histopathologic examination using standard preparation

techniques. No inflammation was observed in any of the ocular tissues in the sections examined. Some changes consistent with injection or mechanical trauma during or post-enucleation were noted. Isolated instances of developmental abnormalities in the retina and ciliary body were also observed.

4.2 Boc-N-R-O-spacer-aa-O-tbut compounds

4.2.1 *Characterization of Boc-N-R-O-spacer-aa-O-tbut compounds*

The characterization of the Boc-N-R-O-spacer-aa-O-tbut synthesized compounds were the following. The characterization of the intermediate compounds are described in the supplementary section.

_N_-Boc-4-aminobutoxy-glutarylsarcosine-*tert*-butyl ester (5)

Name of the structure: 4-(tert-Butoxycarbonylamino)butyl 5-[*N*-methyl(*tert*-butoxycarbonylmethyl) amino]-5-oxovalerate.

Appearance: orange oil. The molecular weight of the compound was 414.54 g/mol. The yield of the reaction was 52.2% (Figure 31).

^{1}H NMR (500 MHz, Chloroform-*d*) δ 5.34 (s, 1H), 4.18-4.12 (m, 2H), 3.24 (t, *J* = 7.5 Hz, 1H), 3.09 (s, 2H), 2.90 (t, *J* = 5.4 Hz, 1H), 2.35 (t, *J* = 8.1 Hz, 1H), 1.96 (tt, *J* = 8.1, 5.3 Hz, 1H), 1.82-1.72 (m, 1H), 1.68 (tt, *J* = 7.6, 5.5 Hz, 1H), 1.43 (d, *J* = 4.9 Hz, 9H).

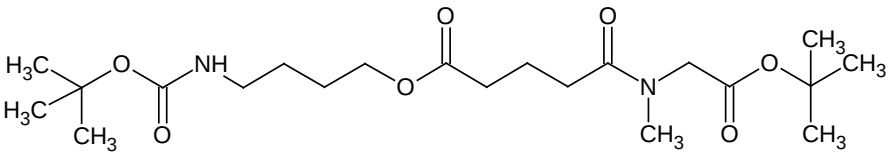

Figure 31. Chemical structure of _N_-Boc-4-aminobutoxy-glutarylsarcosine-*tert*-butyl ester (Boc-N-but-O-glt-Sar-O-tbut).

_N_-Boc-pyrrolidine-3-ol-adipoyl glycine-*tert*-butyl ester (6)

Name of the structure: 3-5-Oxo-5-[(*tert*-butoxycarbonylmethyl)amino]pentyl 1-*tert*-butyl 1,3-pyrrolidine- dicarboxylate.

Appearance: yellowish oil. The molecular weight of the compound was 428.52 g/mol. The yield of the reaction was 53% (Figure 32).

^{1}H NMR (500 MHz, Chloroform-*d*) δ 6.73 (s, 1H), 4.96 (p, *J* = 7.1 Hz, 1H), 4.34 (d, *J* = 12.4 Hz, 1H), 4.10 (dd, *J* = 9.5, 7.0 Hz, 1H), 3.99 (d, *J* = 12.5 Hz, 1H), 3.77 (dt, *J* = 9.5, 7.1 Hz, 1H), 3.51 (dt, *J* = 9.5, 7.1 Hz, 1H), 3.38 (dd, *J* = 9.5, 7.0 Hz, 1H), 2.65 (dt, *J* = 12.4, 3.1 Hz, 1H), 2.58-2.35 (m, 3H), 2.30-2.19 (m, 1H), 2.12-1.96 (m, 2H), 1.87 (qdd, *J* = 12.7, 3.9, 2.5 Hz, 1H), 1.79-1.58 (m, 2H), 1.45 (d, *J* = 20.0 Hz, 18H).

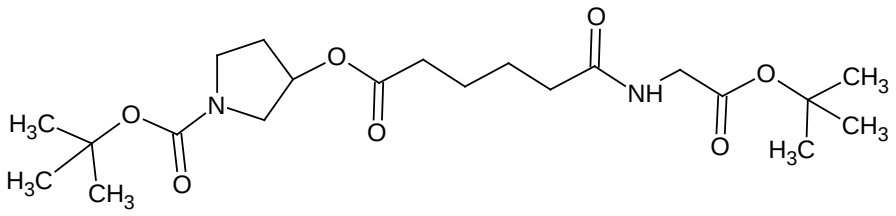

Figure 32. Chemical structure of N-Boc-pyrrolidine-3-ol-adipoyl glycine-t-butyl ester (Boc-3-pyrrol-O-adp-Gly-O-tbut).

N-Boc-piperidine-4-ol-adipoyl glycine *t*-butyl ester (7)

Name of the structure: 4-5-Oxo-5-[(*tert*-butoxycarbonylmethyl)amino]pentyl 1-*tert*-butyl 1,4-piperidine- dicarboxylate.

Appearance: yellowish oil. The molecular weight of the compound was 442.54 g/mol. The yield of the reaction was 48% (Figure 33).

^{1}H NMR (500 MHz, Chloroform-*d*) δ 6.73 (s, 1H), 4.19-4.08 (m, 2H), 3.22 (dt, *J* = 12.4, 7.1 Hz, 1H), 2.52 (t, *J* = 5.4 Hz, 1H), 2.35 (t, *J* = 5.4 Hz, 1H), 2.08-1.97 (m, 1H), 1.91-1.80 (m, 1H), 1.77-1.67 (m, 1H), 1.66-1.56 (m, 1H), 1.45 (d, *J* = 20.0 Hz, 9H).

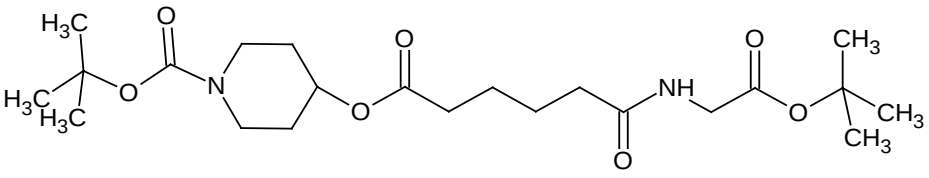

Figure 33. Chemical structure of *N*-Boc-piperidine-4-ol-adipoyl glycine *t*-butyl ester (Boc-4-piper-O-adp-Gly-O-tbut).

N-Boc-4-aminoethoxyethyl-1-ol-glutaryl-Sarcosine-*tert*-butyl ester (14)

Name of the structure: 2-[2-(*tert*-Butoxycarbonylamino)ethoxy]ethyl 5-[*N*-methyl(*tert*-butoxycarbonyl-methyl) amino]-5-oxovalerate.

Appearance: yellow oil. The molecular weight of the compound was 446.54 g/mol. The yield of the reaction was 70% (Figure 34).

^{1}H NMR (500 MHz, Chloroform-*d*) δ 5.34 (s, 1H), δ 4.24-4.14 (m, 2H), 3.77-3.66 (m, 2H), 3.16-3.07 (m, 3H), 2.90 (t, *J* = 5.4 Hz, 1H), 2.35 (t, *J* = 8.2 Hz, 1H), 1.96 (tt, *J* = 8.2, 5.4 Hz, 1H), 1.43 (d, *J* = 4.9 Hz, 9H).

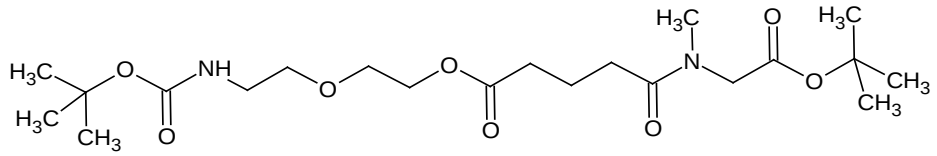

Figure 34. Chemical structure of *N*-Boc-4-aminocyclohexanol–adipoyl sarcosine-*tert*-butyl ester (Boc-N-etOet-O-glt-Sar-O-tbut).

(1*S*,4*R*) *N*-Boc-4-aminocyclohexanol-adipoyl-Glycine-*tert*-butyl ester (15)

Name of the structure: 4-(*tert*-Butoxycarbonylamino)cyclohexyl 6-oxo-6-[(*tert*-butoxy-carbonylmethyl) amino] hexanoate.

Appearance: yellow oil. The molecular weight of the compound was 456.57 g/mol. The yield of the reaction was 24% (Figure 35).

^{1}H NMR (500 MHz, Chloroform-*d*) δ 6.73 (s, 1H), 4.47 (s, 1H), 4.34 (p, *J* = 6.8 Hz, 1H), 4.16 (s, 2H), 3.11 (s, 3H), 2.90 (t, *J* = 5.5 Hz, 2H), 2.35 (t, *J* = 5.3 Hz, 2H), 2.06-1.92 (m, 6H), 1.68-1.56 (m, 2H), 1.58-1.46 (m, 2H), 1.43 (d, *J* = 4.9 Hz, 18H).

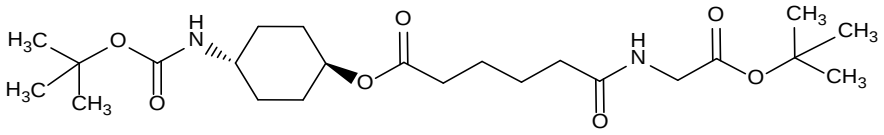

Figure 35. Chemical structure of (1*S*,4*R*) *N*-Boc-4-aminocyclohexanol-adipoyl-Glycine-*tert*-butyl ester (Boc-t,4-N-cyhex-O-adp-Gly-O-tbut).

(1*S*,4*R*) *N*-Boc-4-aminocyclohexanol-glutaryl-Sarcosine-*tert*-butyl ester (16)

Name of the structure: 4-(*tert*-Butoxycarbonylamino)cyclohexyl 5-[*N*-methyl(*tert*-butoxycarbonyl- methyl)amino]-5-oxovalerate.

Appearance: yellow oil. The molecular weight of the compound was 456.58 g/mol. The yield of the reaction was 22.28% (Figure 36).

^{1}H NMR (500 MHz, Chloroform-*d*) δ 4.47 (s, 1H), 4.41-4.36 (m, 1H), 4.16 (s, 2H), 3.73-3.71 (m, 1H), 3.11 (s, 3H), 2.90 (t, *J* = 5.5 Hz, 2H), 2.35 (t, *J* = 5.3 Hz, 2H), 2.06-1.92 (m, 6H), 1.68-1.56 (m, 2H), 1.58-1.46 (m, 2H), 1.43 (d, *J* = 4.9 Hz, 18H).

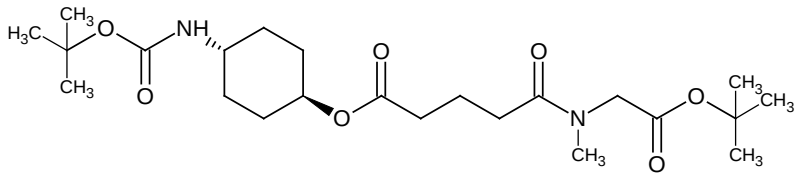

Figure 36: Chemical structure of (1*S*,4*R*) *N*-Boc-4-aminocyclohexanol-glutaryl-Sarcosine-*tert*-butyl ester (Boc-t,4-N-cyhex-O-glt-Sar-O-tbut).

(1*S*,2*S*) *N*-Boc-2-aminocyclopentanol-glutaryl-Sarcosine-*N*-diethylamine-4-nitrobenzamide ester (17)

Name of the structure: (1*S*,2*S*)-2-(*tert*-Butoxycarbonylamino)cyclopentyl 5-(*N*-methyl{2-[2-(*p*-nitrobenzoylamino) ethylamino]-2-oxoethyl}amino)-5-oxovalerate.

Appearance: yellow oil. The molecular weight of the compound was 577.64 g/mol. The yield of the reaction was 7.99% (Figure 37).

^{1}H NMR (500 MHz, Chloroform-*d*) δ 8.33-8.27 (m, 2H), 7.99-7.93 (m, 2H), 7.37 (s, 1H), 6.75 (s, 1H), 5.30 (q, *J* = 7.0 Hz, 1H), 5.07 (d, *J* = 12.5 Hz, 1H), 4.24-4.06 (m, 3H), 3.73 (ddd, *J* = 12.3, 2.8, 1.4 Hz, 1H), 3.48 (td, *J* = 12.0, 2.7 Hz, 1H), 3.37 (td, *J* = 12.0, 2.7 Hz, 1H), 3.08-2.99 (m, 2H), 3.01 (s, 3H), 2.59 (td, *J* = 12.3, 1.1 Hz, 1H), 2.56-2.42 (m, 1H), 2.30-2.16 (m, 3H), 2.07-1.92 (m, 2H), 1.81-1.69 (m, 2H), 1.71-1.54 (m, 2H), 1.44 (s, 10H).

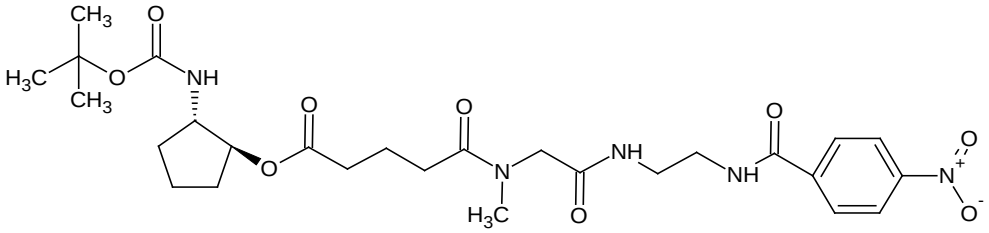

Figure 37. Chemical structure of (1S,2S) *N*-Boc-2-aminocyclopentanolol-glutaryl-Sarcosine-N-diethylamine-4-nitrobenzamide (Boc-2-N-cypent-O-glt-Sar-NetN-CO-ph-NO_2).

(1*S*,3*R*) *N*-3-amino-Boc-cyclopentanol-glutaryl-Sarcosine-*N*-diethylamine-4-nitrobenza (18)

Name of the structure: (1*S*,3*R*)-3-(*tert*-Butoxycarbonylamino)cyclopentyl 5-(*N*-methyl{2-[2-(*p*-nitrobenzoylamino)ethylamino]-2-oxoethyl}amino)-5-oxovalerate.

Appearance: yellow oil. The molecular weight of the compound was 577.64 g/mol. The yield of the reaction was 9.33% (Figure 38).

^{1}H NMR (500 MHz, Chloroform-*d*) δ 9.16 (s, 1H), 8.33-8.27 (m, 2H), 7.99-7.93 (m, 2H), 6.75 (s, 1H), 5.20 (d, *J* = 12.4 Hz, 1H), 4.84 (p, *J* = 6.9 Hz, 1H), 4.47 (s, 1H), 4.08-3.99 (m, 2H), 3.59 (td, *J* = 12.0, 4.2 Hz, 1H), 3.37 (td, *J* = 12.0, 2.7 Hz, 1H), 3.24 (td, *J* = 11.9, 4.2 Hz, 1H), 3.01 (dtd, *J* = 25.4, 12.1, 2.6 Hz, 2H), 2.97 (s, 3H), 2.63 (td, *J* = 12.4, 1.3 Hz, 1H), 2.45 (qdd, *J* = 12.6, 2.7, 1.6 Hz, 1H), 2.36-2.14 (m, 4H), 2.01-1.89 (m, 2H), 1.84 (dt, *J* = 13.0, 7.0 Hz, 1H), 1.44 (s, 9H), 1.41-1.29 (m, 1H).

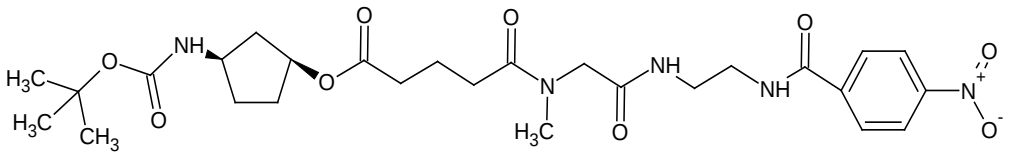

Figure 38. Chemical structure of (1*S*,3*R*) *N*-3-amino-Boc-cyclopentanol-glutaryl-Sarcosine-*N*-diethylamine-4-nitrobenzamide (Boc-3-N-cypent-O-glt-Sar-NetN-CO-ph-NO_2).

(1*S*,4*S*) *N*-Boc-4-aminocyclohexanol-adipoyl-Glycine-tert-butyl ester (19)

Name of the structure: 4-(*tert*-Butoxycarbonylamino)cyclohexyl 6-oxo-6-[(*tert*-butoxycarbonylmethyl) amino] hexanoate.

Appearance: yellow oil. The molecular weight of the compound was 456.58 g/mol. The yield of the reaction was 21.2% (Figure 39).

^{1}H NMR (500 MHz, Chloroform-*d*) δ 6.73 (s, 1H), 4.44 (s, 1H), 4.39 (p, *J* = 6.9 Hz, 1H), 4.17 (s, 2H), 3.68 (p, *J* = 6.9 Hz, 1H), 2.52 (t, *J* = 5.2 Hz, 2H), 2.35 (t, *J* = 8.1 Hz, 2H), 2.08-1.87 (m, 4H), 1.80-1.67 (m, 2H), 1.66-1.56 (m, 4H), 1.49 (ddd, *J* = 12.6, 7.6, 6.3 Hz, 2H), 1.43 (d, *J* = 4.9 Hz, 18H).

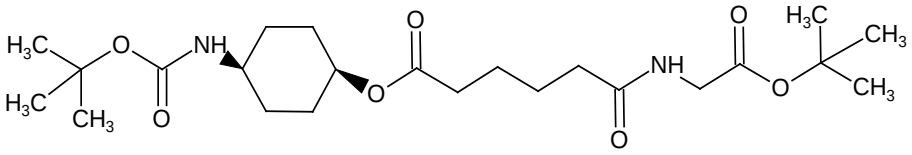

Figure 39. Chemical structure of (1*S*,4*S*) *N*-Boc-4-aminocyclohexanol-adipoyl-Glycine-*tert*-butyl ester (Boc-c,4-N-cyhex-O-adp-Gly-O-tbut).

N-Boc-N'-amidoethyleneamidovaleric-4-ol-glutaryl-Sarcosine-amidoethyleneamino-4-nitrobenzamide (20)

Name of the structure: 1-Methyl-4-oxo-4-[2-(*tert*-butoxycarbonylamino) ethylamino]butyl 5-(*N*-methyl{2-[2-(*p*-nitrobenzoyl- amino)ethylamino]-2-oxoethyl} amino)-5-oxovalerate.

Appearance: yellow oil. The molecular weight of the compound was 636.70 g/mol. The yield of the reaction was 2.86% (Figure 40).

^{1}H NMR (500 MHz, Chloroform-*d*) δ 9.49 (s, 1H), 8.33-8.27 (m, 2H), 7.99-7.93 (m, 2H), 6.75 (s, 1H), 6.19 (s, 1H), 5.24 (d, *J* = 12.5 Hz, 1H), 5.10 (s, 1H), 4.77 (ddddd, *J* = 9.3, 7.9, 6.9, 4.5, 1.6 Hz, 1H), 4.05 (d, *J* = 12.4 Hz, 1H), 3.71-3.46 (m, 4H), 3.41-3.31 (m, 2H), 3.16 (td, *J* = 11.9, 2.9 Hz, 1H), 3.04 (td, *J* = 12.0, 4.1 Hz, 1H), 2.97 (s, 3H), 2.87 (td, *J* = 12.5, 2.6 Hz, 1H), 2.61 (td, *J* = 12.4, 1.4 Hz, 1H), 2.53-2.37 (m, 4H), 2.36-2.20 (m, 3H), 1.83-1.69 (m, 1H), 1.44 (s, 9H), 1.06 (d, *J* = 6.8 Hz, 3H).

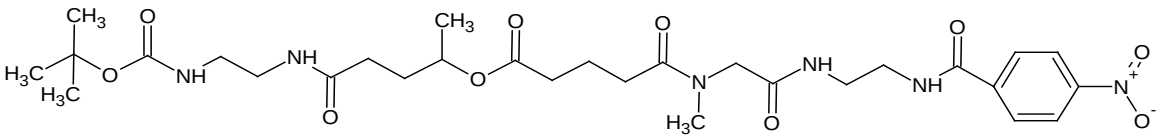

Figure 40. Chemical structure of *N*-Boc-*N'*-amidoethyleneamidovaleric-4-ol-glutaryl-Sarcosine-amidoethyleneamino-4-nitrobenzamide (Boc-NetN-val-secO-glt-Sar-NetN-ph-NO_2).

4.2.2 *Ester hydrolysis testing*

The study of the ester hydrolysis was made by HPLC, a mixture of a hydroalcoholic solution was used due to the precipitation of cmpd. The reason of using a wide range of pH in the buffer (from pH 7.5 ± 0.17) was to prevent the precipitation of the cmpd. Kinetic of ester degradations are shown in Figures 41 and 42 and half-lives are shown in Table III.

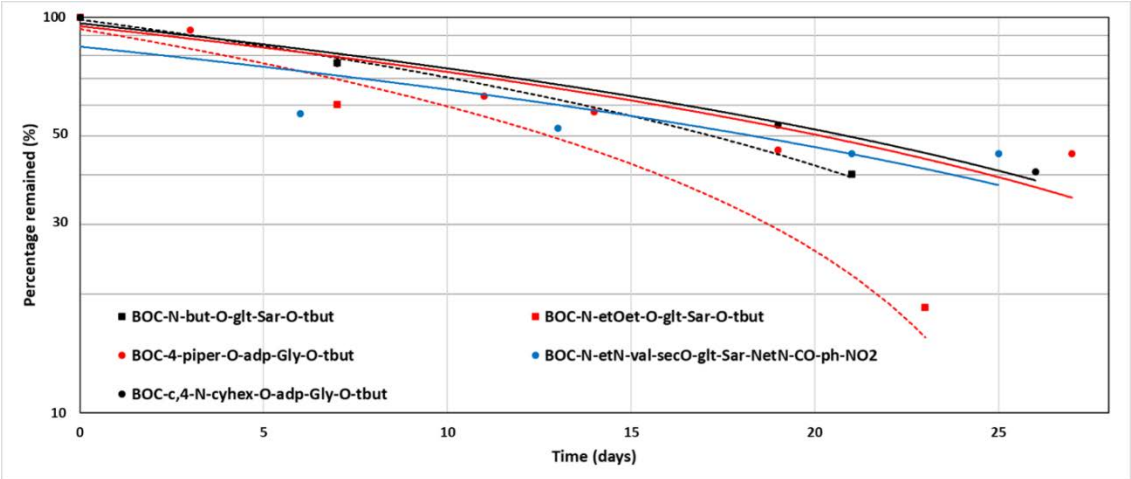

Figure 41. Semi-log representation of the half-live of ester cmpd with less than 25 days. The compound with the ester most labile for hydrolysis was Boc-N-etOet-O-glt-Sar-O-tbut and the compound with the ester most stable for hydrolysis was Boc-c,4-N-cyhex-O-adp-Gly-O-tbut.

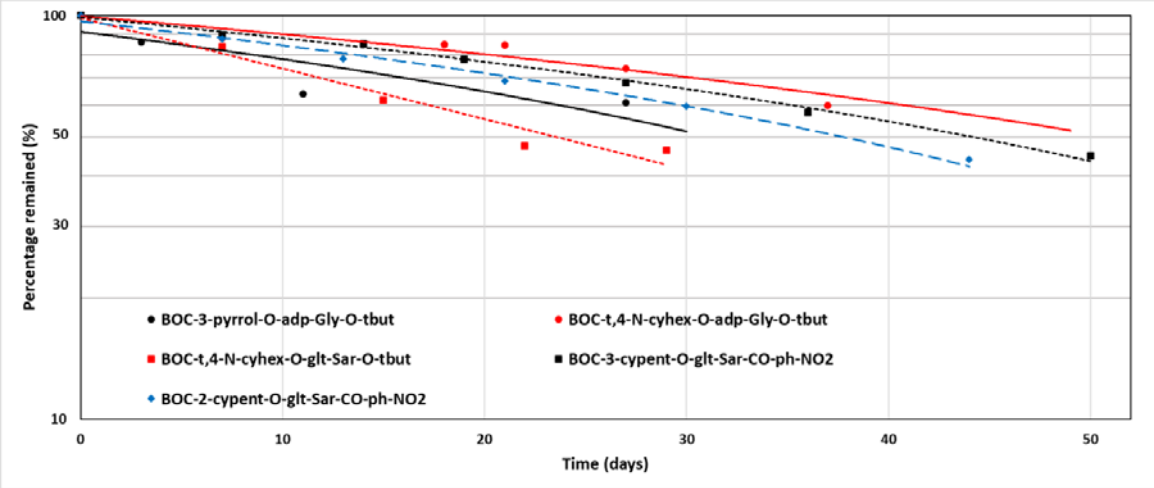

Figure 42. Semi-log representation of the half-live of ester cmpd with more than 25 days. The compound with the ester most labile for hydrolysis was Boc-t,4-N-cyhex-O-glt-Sar-O-tbut and the compound with the ester most stable for hydrolysis was Boc-t,4-N-cyhex-O-adp-Gly-O-tbut. This result suggests that the speed of hydrolysis rate is also affected by the composition in the right side of the molecule.

Table III. Half-lives of the ester compounds

Cmpd	Structure	Half-lives (days)
5	Boc-N-but-O-glt-Sar-O-tbut	17
6	Boc-3-pyrrol-O-adp-Gly-O-tbut	31
7	Boc-4-piper-O-adp-Gly-O-tbut	20
14	Boc-N-etOet-O-glt-Sar-O-tbut	12
15	Boc-t,4-N-cyhex-O-adp-Gly-O-tbut	51
16	Boc-t,4-N-cyhex-O-glt-Sar-O-tbut	24
17	Boc-2-N-cypent-O-glt-Sar-NetN-ph-NO_2	38
18	Boc-3-N-cypent-O-glt-Sar-NetN-ph-NO_2	45
19	Boc-c,4-N-cyhex-O-adp-Gly-O-tbut	21
20	Boc-NetN-val-secO-glt-Sar-NetN-ph-NO_2	25

The same cmpd with different conformation (15 and 19) has shown different hydrolysis rate suggesting that the equatorial conformation of the cyclohexyl structure (15) is more stable than the same structure with axial conformation (19). The results suggest five-

member rings amino-ester compounds are more stable than six-member ring when the right side of the molecule is the same (6 *vs* 7), (17 *vs* 16) and (18 *vs* 16).

Even, after using a wide range of pH (7.5 ± 0.17) and ethanol there were partial precipitations of the cmpd on the walls of the vials and the analytical method was not sensitive and selective. The cmpd with the shortest half-life was the number 14 (12 days) and the one with the longest half-life was the number 15 (51 days).

4.2.3 *Comparison of the behavior of the ester degradation*

Due to the results showed in the ester hydrolysis study where the same amino-alkoxy cmpd attached to different alkyl chains (15 and 16) got different half-lives (51 days and 24 days respectively). Two peptides were synthesized to compare how the length of the alkyl chain might affect to the speed of ester hydrolysis. The peptides were incubated in physiological conditions. The results have shown that the peptide with the shortest dicarboxylic acid alkyl chain (glutaric, 5 carbon chain) had a faster hydrolysis of the ester than the adipic (6 carbon chain) meaning that the right side of the molecule might affect the speed of hydrolysis rate, suggesting that could be affected by side reactions besides hydrolysis and thus, is a factor to consider (Figures 43 and 44, Table IV).

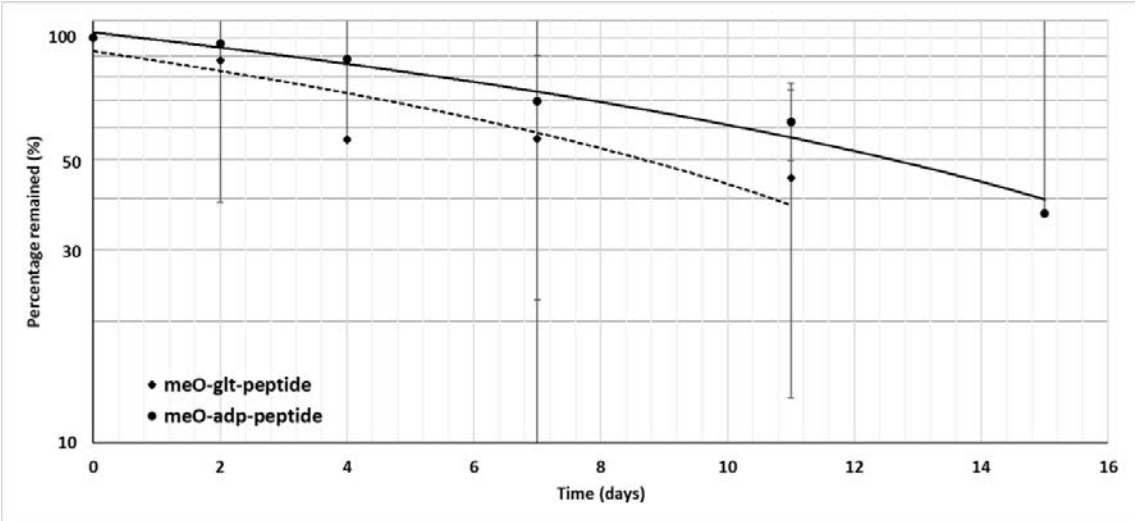

Figure 43. Semi-logarithmic graph of the half-lives of the two peptides with different alkyl chains.

Table IV. Effect of alkyl chain in the half-lives

Peptide	Half-life (days)
meO-glutaric-Sar-GYNLYRVRS	9
meO-adipic-Sar-GYNLYRVRS	13

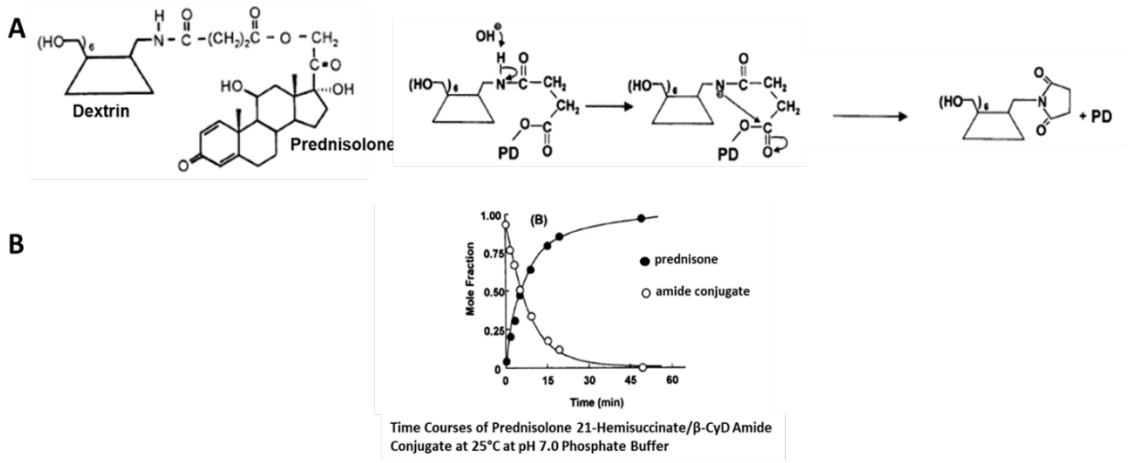

Figure 44. Mechanism of cyclic side reactions. **A:** Chemical mechanism of the cyclic side reaction. **B:** Kinetic graph of the cyclic side reaction rate at physiological conditions. Source: Yano, 2000 (adapted)[323].

4.2.4 *De-blocking of the amino acid carboxylic group of Boc-N-R-O-spacer-aa-O-tbut*

All the ester compounds (see Table I), were reacted with TFA 10% (v/v) to deprotect the carboxylic group of the amino acid (Sar or Gly) to attach the rest of the sequence of the active peptide through the solid-state reaction. Unfortunately, the yield in all the reactions were 0 due to the more rapid de-blocking of the Boc-amine in the left side of the molecule.

4.3 Boc-N-R-O-ahx-DNP compounds

4.3.1 *Characterization of Boc-N-R-O-ahx-DNP esters*

To study the ester degradation only affected by the difference of the amino-alkoxy compound and avoiding the effect of the presence of the length of the alkyl chain. According to the results in Table I, four compounds (*tert*-butyl (4-hydroxybutyl)carbamate; *tert*-butyl 3-hydroxypyrrolidine-1-carboxylate; *tert*-butyl [(1*R*,3*R*)-3-hydroxycyclopentyl]

carbamate and *tert*-butyl (trans-4-hydroxycyclohexyl) carbamate) were selected to synthesize the ester model compounds and compare their speed of degradation of the esters. While the peptide series may be complicated by cyclization reactions whereby the amide nitrogen mat may displace the ester, this is not possible in the model compound, which lacks any amides. Based on the ester hydrolysis rates of the Boc-N-R-O-spacer-aa-O-tbut compounds (Figures 41 and 42), one fast released compound (*tert*-butyl (4-hydroxybutyl) carbamate), one medium released compound (*tert*-butyl 3-hydroxypyrrolidine-1-carboxylate) and two slow released compound (*tert*-butyl (trans-4-hydroxycyclohexyl) carbamate).

4-(*tert*-Butoxycarbonylamino)butyl 6-(2,4-dinitrophenylamino)hexanoate (21)

Appearance: yellow oil. The molecular weight of the compound was 468.50 g/mol. The yield of the reaction was 55.2% (Figure 45).

^{1}H NMR (500 MHz, Chloroform-*d*) δ 8.86 (d, *J* = 2.0 Hz, 1H), 8.24 (dd, *J* = 7.5, 2.0 Hz, 1H), 7.68 (s, 1H), 7.22 (d, *J* = 7.5 Hz, 1H), 5.34 (s, 1H), 4.15 (t, *J* = 7.4 Hz, 2H), 3.48 (t, *J* = 5.3 Hz, 2H), 3.24 (t, *J* = 7.5 Hz, 2H), 2.35 (t, *J* = 5.4 Hz, 2H), 1.82-1.72 (m, 2H), 1.73-1.63 (m, 4H), 1.60 (tt, *J* = 7.7, 5.4 Hz, 2H), 1.44 (s, 9H), 1.38 (tt, *J* = 7.8, 5.7 Hz, 2H).

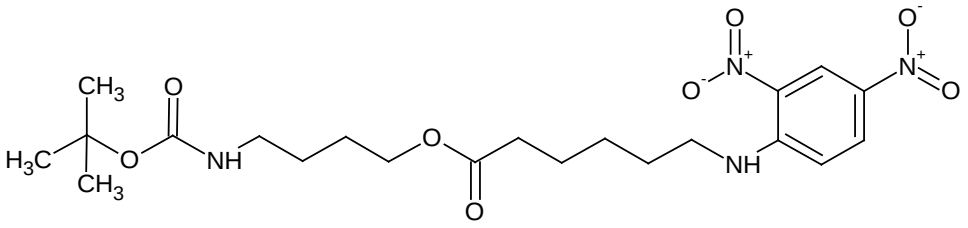

Figure 45. Chemical structure of 4-(*tert*-Butoxycarbonylamino)butyl 6-(2,4-dinitrophenylamino) hexanoate (Boc-N-but-O-ahx-DNP).

3-5-(2,4-Dinitrophenylamino)pentyl 1-*tert*-butyl 1,3-pyrrolidinedicarboxylate (22)

Appearance: yellow oil. The molecular weight of the compound was 466.49 g/mol. The yield of the reaction was 64.75% (Figure 46).

^{1}H NMR (500 MHz, Chloroform-*d*) δ 8.86 (d, *J* = 2.0 Hz, 1H), 8.24 (dd, *J* = 7.5, 2.0 Hz, 1H), 7.22 (d, *J* = 7.5 Hz, 1H), 4.96 (p, *J* = 7.1 Hz, 1H), 4.07 (td, *J* = 12.4, 2.5 Hz, 1H), 3.73 (dt, *J* = 9.5, 7.1 Hz, 1H), 3.61 (dd, *J* = 9.4, 7.1 Hz, 1H), 3.54-3.45 (m, 2H), 3.14 (td, *J* = 12.2, 3.5 Hz, 1H), 2.68 (ddd, *J* = 13.7, 12.6, 1.5 Hz, 1H), 2.61-2.49 (m, 2H), 2.35 (dq, *J* = 14.0, 7.1 Hz, 1H), 2.19 (s, 1H), 1.99-1.88 (m, 1H), 1.65-1.47 (m, 3H), 1.47 (s, 9H), 1.41 (dddd, *J* = 15.7, 12.3, 5.3, 3.5 Hz, 1H), 1.14-1.03 (m, 1H).

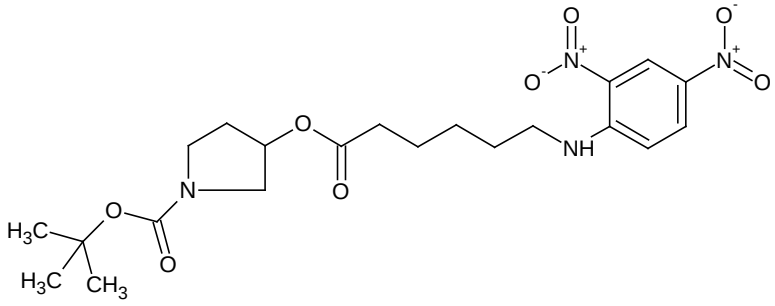

Figure 46. Chemical structure of 3-5-(2,4-Dinitrophenylamino)pentyl 1-*tert*-butyl 1,3-pyrrolidine dicarboxylate (Boc-3-pyrrol-O-ahx-DNP).

(1*R*,3*S*)-3-(*tert*-Butoxycarbonylamino)cyclopentyl 6-(2,4-dinitrophenylamino) hexanoate (23)

Appearance: yellow oil. The molecular weight of the compound was 480.51 g/mol. The yield of the reaction was 65.8% (Figure 47).

^{1}H NMR (500 MHz, Chloroform-*d*) δ 9.99 (s, 1H), 8.86 (d, *J* = 2.0 Hz, 1H), 8.24 (dd, *J* = 7.5, 2.0 Hz, 1H), 7.22 (d, *J* = 7.5 Hz, 1H), 4.89-4.79 (m, 1H), 4.66 (s, 1H), 3.75-3.66 (m, 1H), 3.25 (pd, *J* = 12.4, 3.4 Hz, 2H), 2.57 (ddt, *J* = 12.2, 6.1, 1.5 Hz, 1H), 2.57-2.47 (m, 1H), 2.16-2.01 (m, 2H), 1.91-1.81 (m, 4H), 1.84-1.76 (m, 1H), 1.75-1.62 (m, 1H), 1.58 (dddt, *J* = 15.2, 8.2, 3.5, 1.3 Hz, 1H), 1.44 (s, 9H), 1.48-1.35 (m, 1H), 1.34-1.21 (m, 1H).

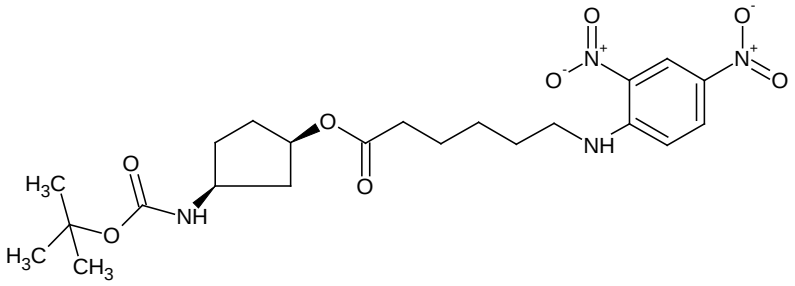

Figure 47. Chemical structure of (1*R*,3*S*)-3-(*tert*-Butoxycarbonylamino)cyclopentyl 6-(2,4-dinitrophenylamino)hexanoate (Boc-3-*N*-cypent-O-ahx-DNP).

4-(*tert*-Butoxycarbonylamino)cyclohexyl 6-(2,4-dinitrophenylamino)hexanoate (24)

Appearance: yellow oil. The molecular weight of the compound was 494.54 g/mol. The yield of the reaction was 77.6% (Figure 48).

^{1}H NMR (500 MHz, Chloroform-*d*) δ 8.86 (d, *J* = 2.0 Hz, 1H), 8.24 (dd, *J* = 7.5, 2.0 Hz, 1H), 7.69 (s, 1H), 7.22 (d, *J* = 7.5 Hz, 1H), 4.47 (s, 1H), 4.40 (p, *J* = 6.9 Hz, 1H), 3.67 (p, *J* = 6.9 Hz, 1H), 3.48 (t, *J* = 7.6 Hz, 2H), 2.35 (t, *J* = 8.1 Hz, 2H), 2.07-1.92 (m, 4H), 1.72-1.55 (m, 6H), 1.55-1.45 (m, 2H), 1.44 (s, 9H), 1.38 (t, *J* = 7.8 Hz, 2H).

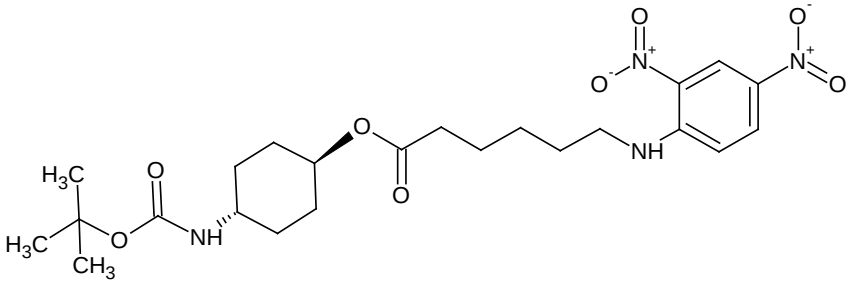

Figure 48. Chemical structure of 4-(*tert*-Butoxycarbonylamino)cyclohexyl 6-(2,4-dinitrophenylamino) hexanoate (Boc-t,4-*N*-cyhex-O-ahx-DNP).

4.3.3 *Ester hydrolysis kinetics of Boc-N-R-O-ahx-DNP cmpd*

The study of the ester hydrolysis was made by HPLC, in a HEPES buffer solution at pH of 7.4. Kinetics of ester degradations are shown in Figure 49. The half-lives are shown in Table III and are compared with the same esters of the previous study (Table V).

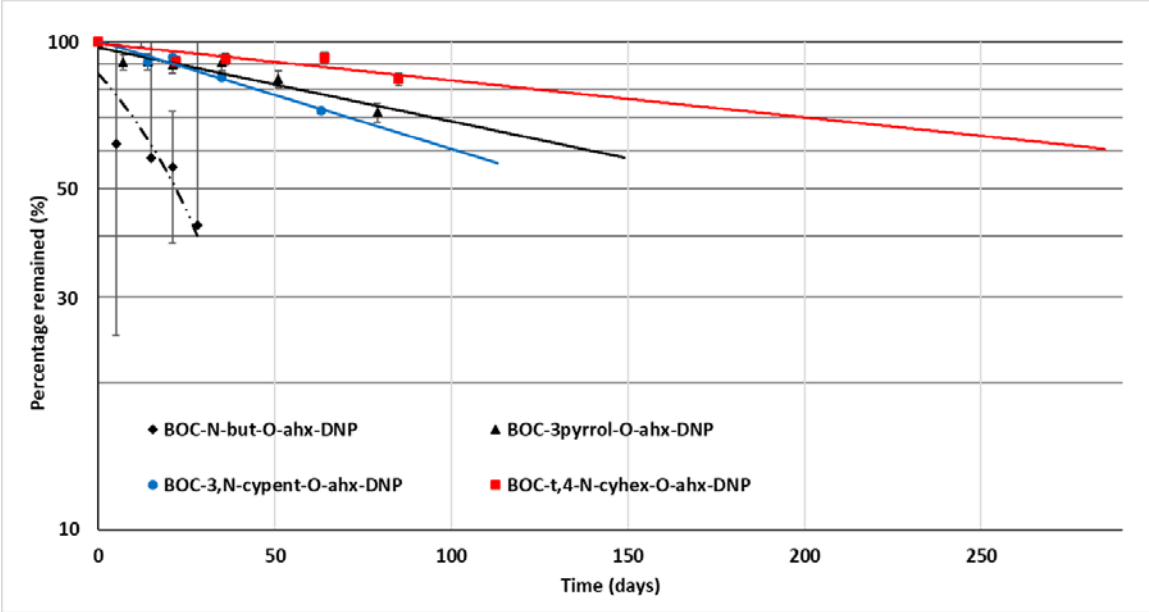

Figure 49. Semi-log representation of the half-live of the model ester compounds Boc-N-but-O-ahx-DNP, Boc-3-pyrrol-O-ahx-DNP, Boc-3-N-cypent-O-ahx-DNP and Boc-t,4-N-cyhex-O-ahx-DNP.

Table V. Half-lives of the model ester compounds

Cmpd	**Structure**	**Half-lives (days)**	**Proportion half-lives increased***
21	Boc-N-but-O-ahx-DNP	21	1:1.4
22	Boc-3pyrrol-O-ahx-DNP	160	1:5.2
23	Boc-3-N-cypent-O-ahx-DNP	120	1:2.7
24	Boc-t,4-N-cyhex-O-ahx-DNP	290	1:5.7

*****Ester half-lives compared with the ester half-lives of the compounds 5, 6, 18 and 15 respectively (Table III).

The results have shown, in all cases, a reduction of the speed of degradation of the esters in physiological conditions, especially the ester compounds made with a secondary alcohol, the speed of degradation was reduced between 5 and 6 times. Semi-log loss curves and half-lives showed that the speed of cleavage was Boc-N-but-O-ahx-DNP <Boc-3-N-cypent-O-ahx-DNP <Boc-3-pyrrol-O-ahx-DNP <Boc-t,4-N-cyhex-O-ahx-DNP. The half-life of the cmpd made with amino-cyclopentanol (23) is shorter than the cmpd 22 made with 3-pyrrolidine, when in the previous study was the opposite.

The half-lives shown on Table III are probably representative of the relative hydrolysis rates of simple carboxyl ester prodrugs for these bridging carbamates since there is no opportunity for 5-, 6- or 7-membered cyclic intermediates with distal amide nitrogen atoms, as in the case of amides/peptides.

However, the N-Boc group is very sterically crowded and electron donating thus may influence the ester hydrolysis. Therefore, we sought to compare kinetics of hydrolysis with the corresponding bridged carbamates on the relevant CDEX OH groups.

4.3.4 *Attachment of the N-R-O-ahx-DNP cmpd to the nanogel CDEX*

a) Deprotection of the amine

Before the conjugation of the amino-ester compounds to the nanogel, the amine had to be de blocked via Boc removal. The final compounds were the following (Figure 50).

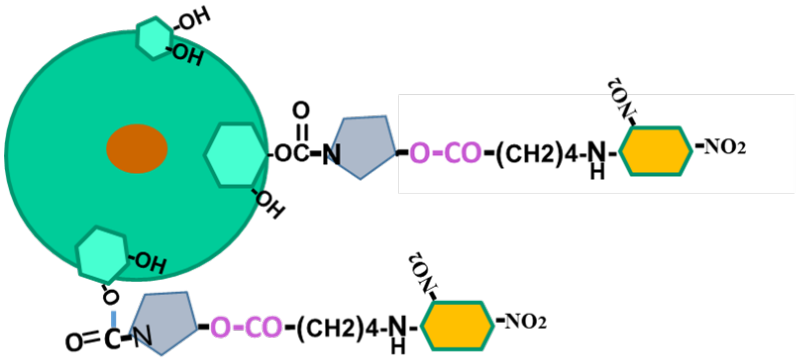

Figure 50. Schematic representation of a conjugate NP: NP-OCON-3-pyrrol-O-ahx-DNP.

4-Aminobutyl 6-(2,4-dinitrophenylamino)hexanoate (25)

Appearance: yellow oil. The molecular weight of the compound was 368.39 g/mol. The yield of the reaction was 100% (Figure 51).

^{1}H NMR (500 MHz, DMSO-d_6) δ 8.77 (s, 1H), 8.24 (dd, J = 7.5, 2.0 Hz, 1H), 7.22 (d, J = 7.5 Hz, 1H), 4.12 (t, J = 4.8 Hz, 2H), 3.48 (t, J = 7.6 Hz, 2H), 2.66 (t, J = 5.1 Hz, 2H), 2.34 (t, J = 8.0 Hz, 2H), 1.72-1.53 (m, 8H), 1.38 (p, J = 5.7 Hz, 2H), 1.05 (s, 2H).

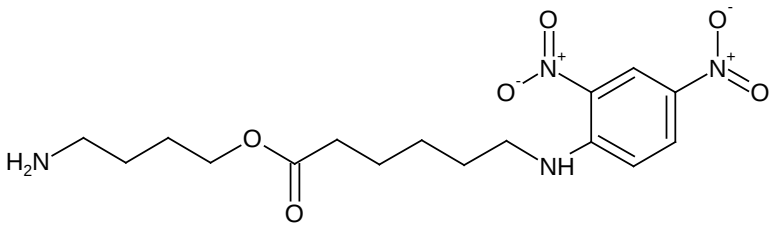

Figure 51. Chemical structure of 4-Aminobutyl 6-(2,4-dinitrophenylamino)hexanoate (NH_2-but-O-ahx-DNP).

3-Pyrrolidinyl 6-(2,4-dinitrophenylamino)hexanoate (26)

Appearance: yellow oil. The molecular weight of the compound was 366.37 g/mol. The yield of the reaction was 100% (Figure 52).

^{1}H NMR (500 MHz, DMSO-d_6) δ 8.86 (d, J = 2.0 Hz, 1H), 8.77 (s, 1H), 8.24 (dd, J = 7.5, 2.0 Hz, 1H), 7.22 (d, J = 7.5 Hz, 1H), 4.95 (p, J = 7.1 Hz, 1H), 3.34-3.26 (m, 1H), 3.21-3.12 (m, 2H), 3.06 (dt, J = 9.5, 7.1 Hz, 1H), 2.98 (dt, J = 9.5, 7.0 Hz, 1H), 2.75 (dd, J = 9.5, 7.0 Hz, 1H), 2.48 (td, J = 12.8, 1.5 Hz, 1H), 2.25 (dq, J = 12.2, 1.9 Hz, 1H), 2.05-1.87 (m, 2H), 1.76-1.64 (m, 2H), 1.55-1.44 (m, 1H), 1.48-1.34 (m, 2H), 1.31 (tt, J = 11.6, 3.1 Hz, 1H), 1.09 (ddtd, J = 13.9, 12.3, 3.4, 1.8 Hz, 1H).

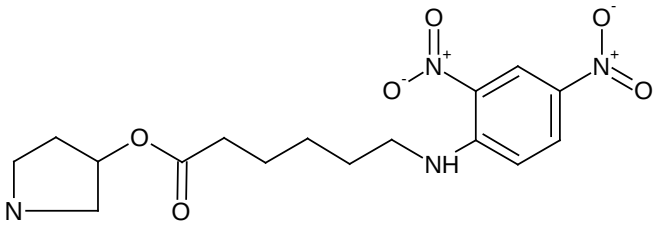

Figure 52. Chemical structure of 3-Pyrrolidinyl 6-(2,4-dinitrophenylamino)hexanoate (3-pyrrol-O-ahx-DNP).

(1*R*,3*S*)-3-Aminocyclopentyl 6-(2,4-dinitrophenylamino)hexanoate (27)

Appearance: yellow oil. The molecular weight of the compound was 380.40 g/mol. The yield of the reaction was 100% (Figure 53).

^{1}H NMR (500 MHz, DMSO-d_6) δ 8.86 (d, *J* = 2.0 Hz, 1H), 8.77 (s, 1H), 8.24 (dd, *J* = 7.5, 2.0 Hz, 1H), 7.22 (d, *J* = 7.5 Hz, 1H), 4.82 (p, *J* = 6.9 Hz, 1H), 3.58-3.50 (m, 1H), 3.00 (td, *J* = 12.3, 1.4 Hz, 1H), 2.72 (p, *J* = 6.9 Hz, 1H), 2.24-2.12 (m, 2H), 1.97 (dt, *J* = 13.0, 7.0 Hz, 1H), 1.92-1.72 (m, 4H), 1.49 (s, 2H), 1.43-1.20 (m, 4H), 1.20-1.06 (m, 2H), 1.07-0.94 (m, 1H).

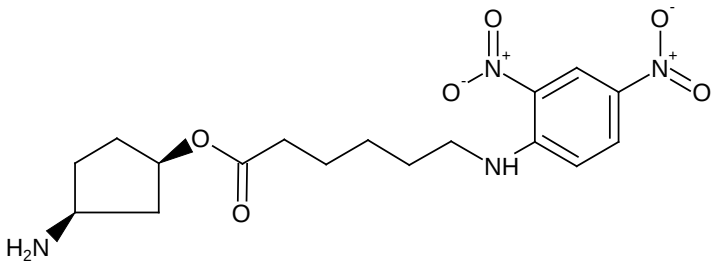

Figure 53. Chemical structure of (1*R*,3*S*)-3-Aminocyclopentyl 6-(2,4-dinitrophenylamino)hexanoate (3-NH_2-cypent-O-ahx-DNP).

4-Aminocyclohexyl 6-(2,4-dinitrophenylamino)hexanoate (28)

Appearance: yellow oil. The molecular weight of the compound was 394.43 g/mol. The yield of the reaction was 100% (Figure 54).

^{1}H NMR (500 MHz, DMSO-d_6) δ 8.86 (d, *J* = 2.0 Hz, 1H), 8.77 (s, 1H), 8.24 (dd, *J* = 7.5, 2.0 Hz, 1H), 7.22 (d, *J* = 7.5 Hz, 1H), 4.24 (p, *J* = 6.9 Hz, 1H), 3.48 (t, *J* = 7.6 Hz, 2H), 2.41 (p, *J* = 7.0 Hz, 1H), 2.32 (t, *J* = 8.2 Hz, 2H), 1.81-1.53 (m, 9H), 1.48-1.25 (m, 6H), 1.30 (s, 3H).

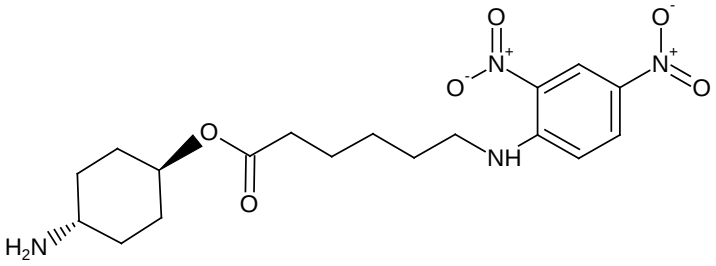

Figure 54. Chemical structure of 4-Aminocyclohexyl 6-(2,4-dinitrophenylamino)hexanoate (t,4-NH_2-cyhex-O-ahx-DNP).

b) CDEX activation and DNP cmpd conjugation

The activation of CDEX with *p*-nPCOCl was checked by the chromogenic method. The *p*-nitrophenolate by spectrum shown a range of 57-154 of the OH groups have been activated.

All the compounds were analyzed by spectrophotometry UV-Vis to quantify the amount of ester-DNP cmpd/ NP. The sizes were analyzed, by dynamic light scattering in triplicate (Figure 55, Table VI).

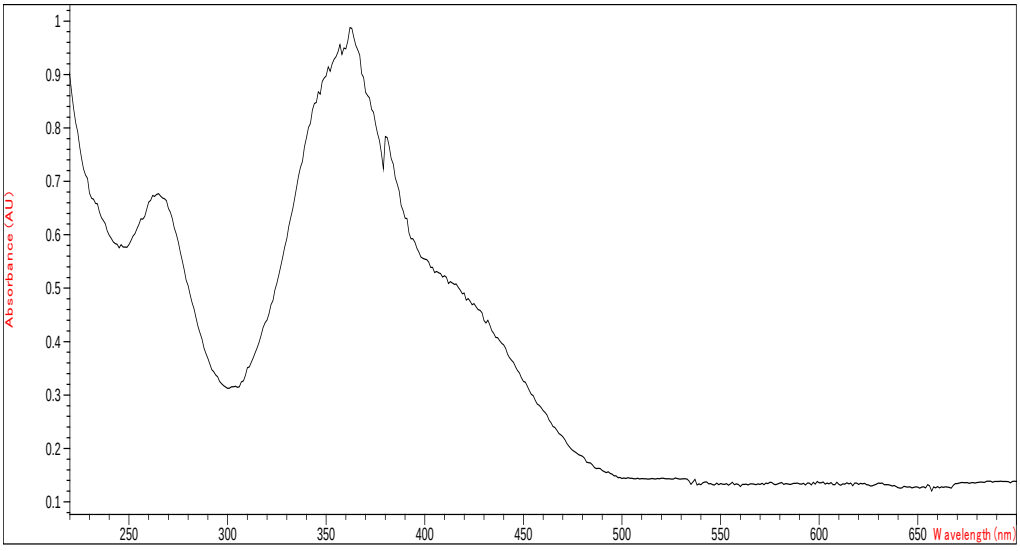

Figure 55. UV-vis spectrum of the 3-pyrrol-O-ahx-DNP conjugated with the nanocarrier (CDEX70-3-pyrrol-O-ahx-DNP). λ_{max} DNP = 360 nm.

Table VI. CDEX characterization

Cmpd	DNP/CDEX	Particle diameter (nm)	% CDEX mass recovered
25	17	102.6±6	61.54
26	30	179±21	9.35
27	2	187±19	70.1
28	3	228±44	90

The results have shown a low yield of conjugation of the DNP cmpd. However the 3-pyrrolidinyl compound gave the highest coupling, making it favored for high yield conjugation.

UV-Vis quantification of the compounds shows a height of the DNP peaks at 360 nm, subtracting only the high background scattering at 600 nm, leads to calculation of DNP/NP which appears in Table II, based on the molar extinction of (λ = 360 nm, ε_{DNP}: 16,622 M^{-1} cm^{-1}). Due to the minimum light scattering of the NP at this wavelength in comparison with the conjugate NP with ethanolamine, we could consider this measurement precise. Conjugation results suggest that the nature of the reactive amine is critical to achieve good conjugate results. According to the observed results, the order of reactive amines are: 3-pyrrolidine- >NH_2-but- >NH_2-cyclohexyl = NH_2-cyclopentyl.

c) *In vitro* release studies of DNP-ester compounds from CDEX

The four CDEX70 conjugates with the amino-ester-DNP compounds were incubated in HEPES buffer, pH 7.4 at 37 °C. At different day time-points filterable free DNP compounds (3 kDa MWCO centrifugal filter) were identified by UV-VIS spectroscopy, (λmax = 360 nm). Semi-log loss curves and half-life have showed that the speed of cleavage was CDEX70-N-but-O-ahx-DNP <CDEX70-3-pyrrol-O-ahx-DNP <CDEX70-3-N-cypent-O-ahx-DNP <CDEX70-4-N-cyhex-O-ahx-DNP (Figure 56 and Table VII). The behavior of the ester hydrolysis of three of these compounds was different with their predecessors [Boc-N-R-O-ahx-DNP Figure 49 and Table V (cmpd 22, 23 and 24)]. But it was the same as the first ester hydrolysis study with the Boc-N-R-O-spacer-aa-O-tbut cmpd (Figures 41 and 42 and Table III; cmpd 5, 6, 18 and 15), where the ester cmpd made with secondary alcohols have slower hydrolysis rate than the ester made with the primary alcohol. On this case, the

hydrolysis of the esters is only affected by the nature of amino-alkoxy compound of the left side of the molecule and not by the length of the alkyl chain of the right side of the molecule.

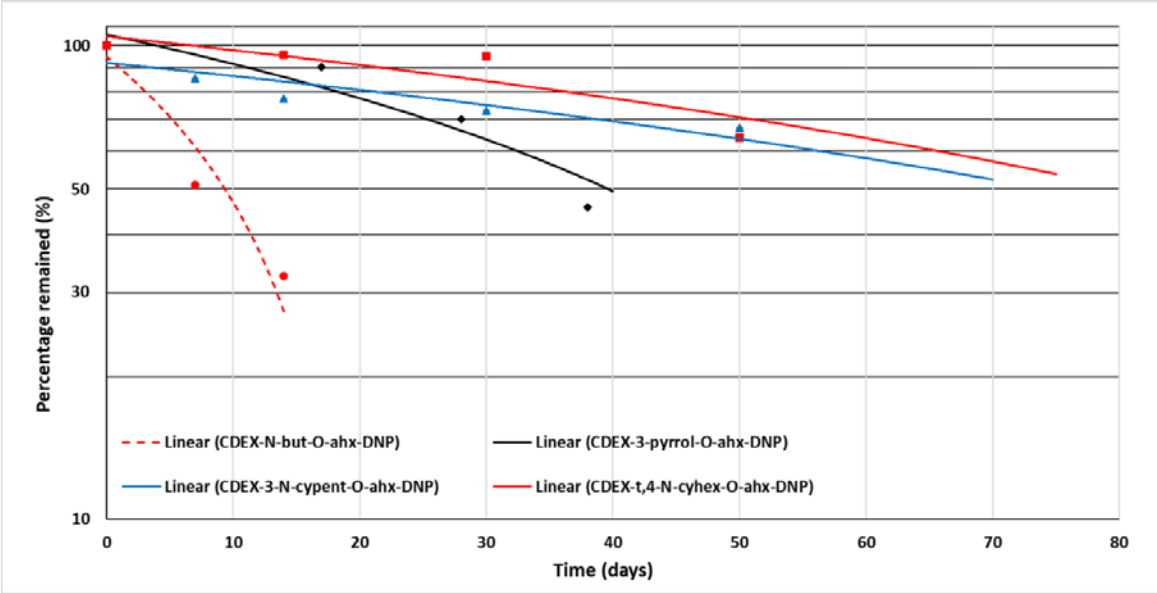

Figure 56. Semi-log representation of the half-life of the hydrolysis of the DNP amino ester compound conjugates to NP affected by the nature of the amino-alcoxy cmpd.

Table VII. Half-lives of the DNP-ester conjugates to NP

Cmpd	Structure	Half-lives (days)
28	CDEX70-N-but-O-ahx-DNP	9
29	CDEX70-3-pyrrol-O-ahx-DNP	40
30	CDEX70-3-N-cypent-O-ahx-DNP	74
31	CDEX70-4-N-cyhex-O-ahx-DNP	81

4.4 *In vitro* release studies of dicarboxypeptide prodrugs from CDEX

4.4.1 *Attempted alpha aminoacyl group t-butyl esters deprotection to yield peptide cap*

To attach an aminoalkoxy-ester bridged Gly or Sar to the distal resin-linked peptide to give aminoalkyl-prodrug, the t-butyl esters on the right hand sides of the molecules have to be

deprotected. 0.1 mEq of the compounds (5-7, 14-20) were dissolved, separately, in a solution of 10% (v/v) TFA in DCM. The reactions were carried out at RT over 24 h.

Progress was checked by TLC (DCM: MeOH; 9:1). When complete, 20 volumes of toluene were added to the mixture and carboxylic products were dried under vacuum and extracted with a mixture of water:DCM, the isolated aqueous phase then lyophilized (Figure 57). The designed synthesis pathway to get the final ester prodrug peptide was to react the free carboxylic acid of the Boc-amidoalkoxy (adp or glt)-capped amino acid (Sar or Gly) with the extending peptide chain immobilized on a resin through a solid state reaction. After attaching the rest of the peptide sequence, the compound was treated with TFA to release the peptide from the resin and de-block the amine of the left side of the molecule (Figure 58).

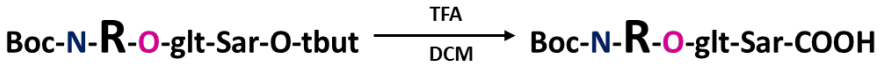

Figure 57. Scheme of the deprotection of the sarcosine carboxylic group of aminoalkoxy-ester bridge.

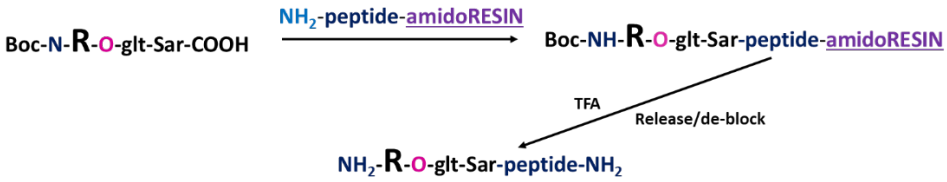

Figure 58. Scheme of the solid-state reaction and de blocking of the ester prodrug peptide.

Unfortunately, we found that the acid deprotection reaction step removed the *N*-Boc group much more rapidly than it removed the t-butyl ester. This required our establishing another route to give the desired intermediate shown on the top left of Figure 25, needed for appending to the peptide during solid-state synthesis. Our successful new route is described in the synthesis of the cmpd 22.

4.4.1 *Characterization of the peptide prodrug*

Due to the problems on the de-blocking step of the amino acid carboxylic group of the previous compounds, an alternative synthesis pathway was used to get the prodrug ester.

6-{[1-(*tert*-butoxycarbonyl)pyrrolidin-3-yl]oxy}-6-oxohexanoic acid (32)

Appearance: yellow-orange oil. The molecular weight of the compound was 315.36 g/mol. The yield of the reaction was 46.6% (Figure 59).

^{1}H NMR (500 MHz, Chloroform-*d*) δ 4.96 (p, *J* = 7.1 Hz, 1H), 4.10 (dd, *J* = 9.5, 7.0 Hz, 1H), 3.78 (dt, *J* = 9.5, 7.1 Hz, 1H), 3.52 (dt, *J* = 9.5, 7.1 Hz, 1H), 3.37 (dd, *J* = 9.4, 7.1 Hz, 1H), 2.63 (td, *J* = 12.5, 1.5 Hz, 1H), 2.40-2.30 (m, 2H), 2.32-2.22 (m, 3H), 2.08-1.77 (m, 3H), 1.66-1.55 (m, 1H), 1.47 (s, 9H).

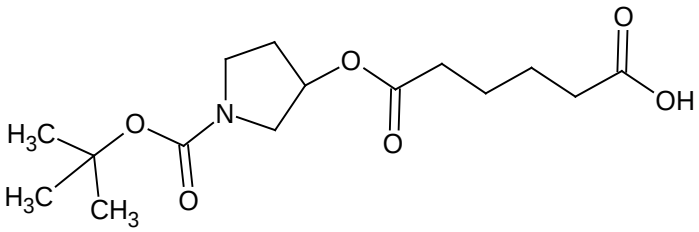

Figure 59. Chemical structure of 6-{[1-(*tert*-butoxycarbonyl)pyrrolidin-3-yl]oxy}-6-oxohexanoic acid (Boc-3-pyrrol-O-adp-OH).

Ester prodrug 3-pyrrolidine-O-adipic-N-Sar-Tyr-Asn-Leu-Tyr-Arg-Val-Arg-Ser-amide (33)

Appearance: white powder. The molecular weight of the compound was 1,337.55 g/mol. The yield of the reaction was 26% (Figure 60).

To demonstrate the purity of the compound, it was checked by mass spectrometry (Figure 61).

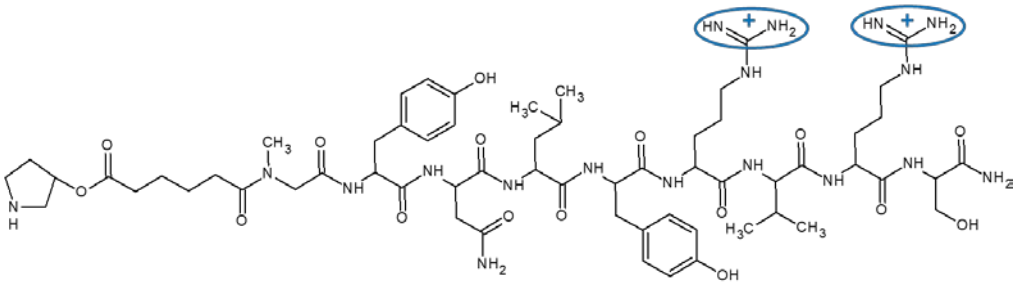

Figure 60: Chemical structure of 3-pyrrolilidine-O-adipic-N-Sar-Tyr-Asn-Leu-Tyr-Arg-Val-Arg-Ser-amide (3-pyrrol-O-11 peptide). Highlighted the region of the structure with positive charges.

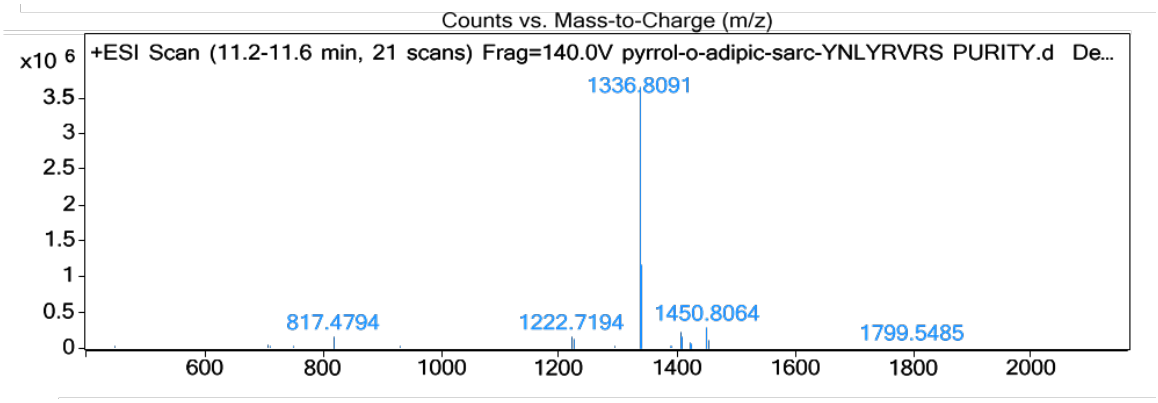

Figure 61. Mass spectrometry of the compound 3-pyrrolidine-O-adipic-N-Sar-Tyr-Asn-Leu-Tyr-Arg-Val-Arg-Ser-amide.

4.4.2 *Characterization of CDEX70-3-pyrrol-O-11 peptide*

The first quantification was the analysis of *p*-nP attached to CDEX70 UV-VIS (ʎ = 400 nm; $\varepsilon_{pNP\text{-}OH}$ = 18,100 M^{-1} cm^{-1}). The amount of *p*-nitrophenyl groups per CDEX particle is 108 (29% of the free hydroxyl groups of dextran).

The analysis for the conjugation reaction were the yield of the reaction, the size by dynamic light scattering and the ζ by electrophoretic light scattering (n = 3). The amount of peptide was quantified by UV (ʎ = 275 nm; ε_{Tyr} = 2,200 M^{-1} cm^{-1}) and by BCA (Table IX). On this case we have to take as valid the result by UV (Tyr). BCA was inaccurate due to the length and the MW of the peptide are under the recommended specifications for this technique.

Table IX. Characterization of CDEX70-3-pyrrol-O-11 peptide

Amount *p*-nP/CDEX	108
% CDEX mass recovered (%)	78
Particle diam. (nm)	178±9.4
ζ (mV)	2.3±0.4
Peptide/CDEX by UV	57
Peptide/CDEX by BCA	30*
Positive charges/CDEX	114

*The peptide quantification was taken to be that established by UV Tyr spectrum. UV (based on Tyr molar extinction of 2,200 at 275 nm). BCA is considered less accurate when peptide is appended to carrier, where free peptide is used as BCA reference standard.

4.4.3 *Stability test of 3-pyrrol-O-11 peptide*

The peptide 3-pyrrol-O-11 was checked by HPLC in several reaction conditions, the peptide itself, the peptide in presence of *p*-nP-OH, TEA, DMSO at 45 °C in N_2 atmosphere during 3 d and the quench step, mixed with *m*-dPEG®$_4$-amine (Figures 62-64).

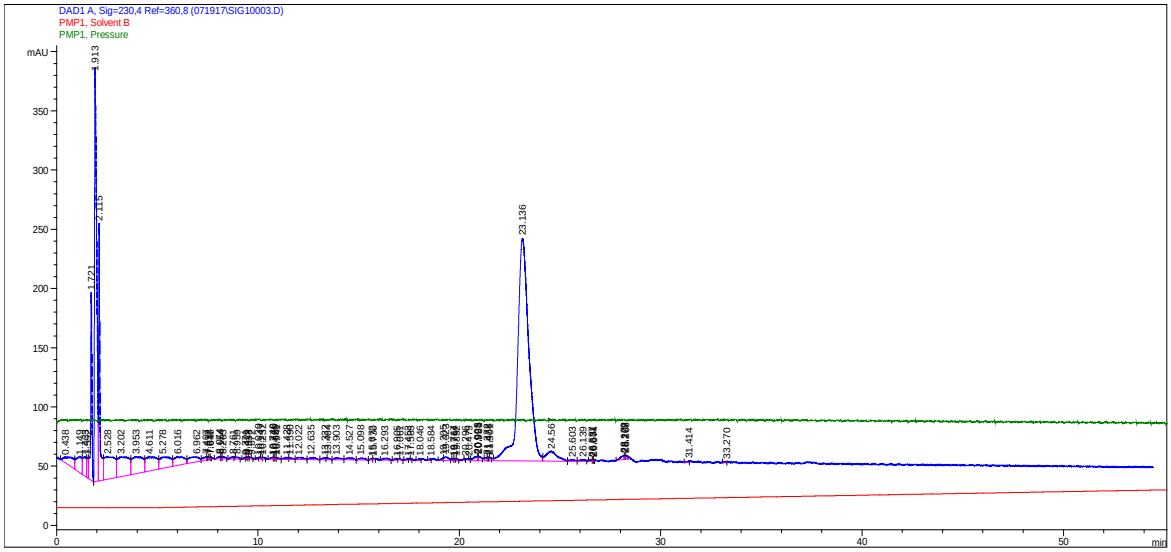

Figure 62. Chromatogram of 3-pyrrol-O-11 peptide (100 µg/mL in water), reference standard (Retention of time: 23.1 min).

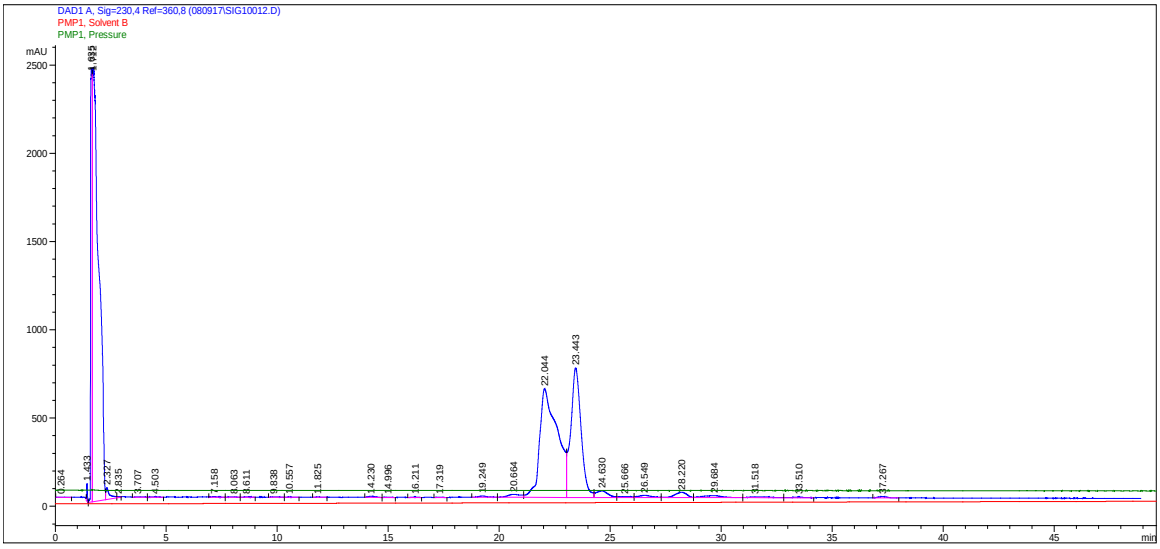

Figure 63. Chromatogram of 3-pyrrol-O-11 peptide in the reaction conditions. There is a new peak (Retention of time: 22.0 minutes) due to the degradation of the prodrug peptide in the reaction conditions.

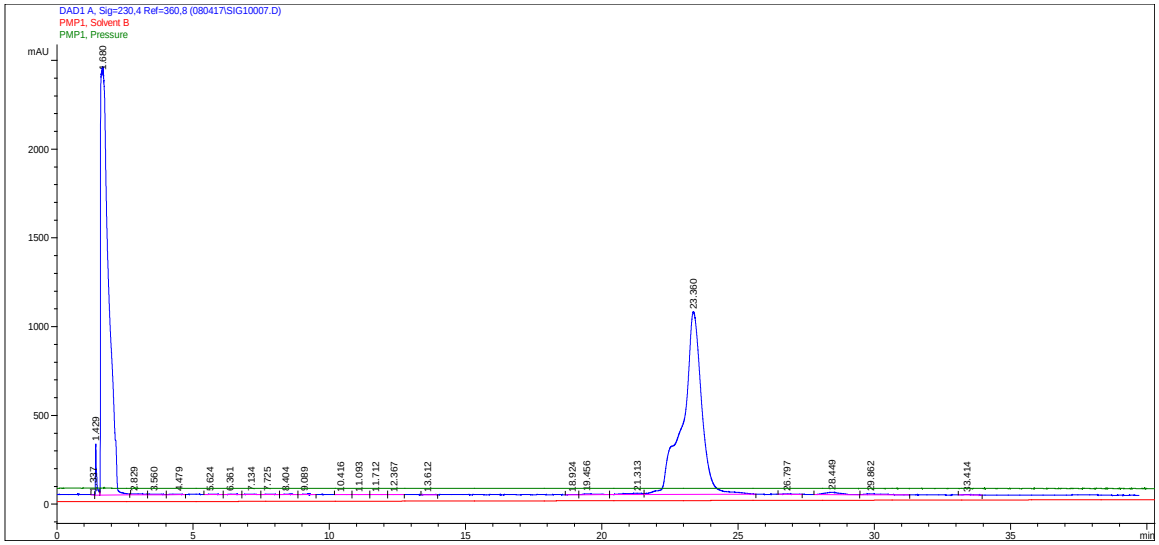

Figure 64. Chromatogram of 3-pyrrol-O-11 peptide in the quench step (mixed with *m*-dPEG®$_4$-amine). There was a change on the shape of the peak, due to the degradation of the prodrug peptide.

4.4.4 *In vitro rate of the active peptide release from CDEX70-3-pyrrol-O-11 peptide*

0.44 mg/mL of the CDEX70 conjugate containing 76 µM linked 11 peptide was incubated in HEPES buffer, pH 7.4 at 37 °C. At 0, 3 and 12 day time-points filterable peptide (10 kDa MWCO centrifugal filter, speed: 14,000 g, time: 10 min, RT) was identified by UV spectrum of the filtrate, where 100 µM peptide has peak (λ = 275 nm; ε_{Tyr} = 2,200 M^{-1} cm^{-1}). Filtrate was checked by the validated analytical method, by HPLC using the peptide 11 as reference standard. A semi-log loss curve (n = 3) shows half-life of 28 days, releasing bioactive peptide at approximately 2% per day of the nanoparticle-bound amount (Figures 65-69). In comparison of the release rate of the DNP-ester compound made with 3-pyrrolidinol (cmpd 28) attached to the NP ($t_{½}$ = 40 days) (Table VII). Suggests that there is some type of side reactions besides the hydrolysis reaction giving new side compounds which appear as new peaks in the chromatogram (Figure 68) but even this circumstance, the mayor compound recovered from the release study was the peptide 11.

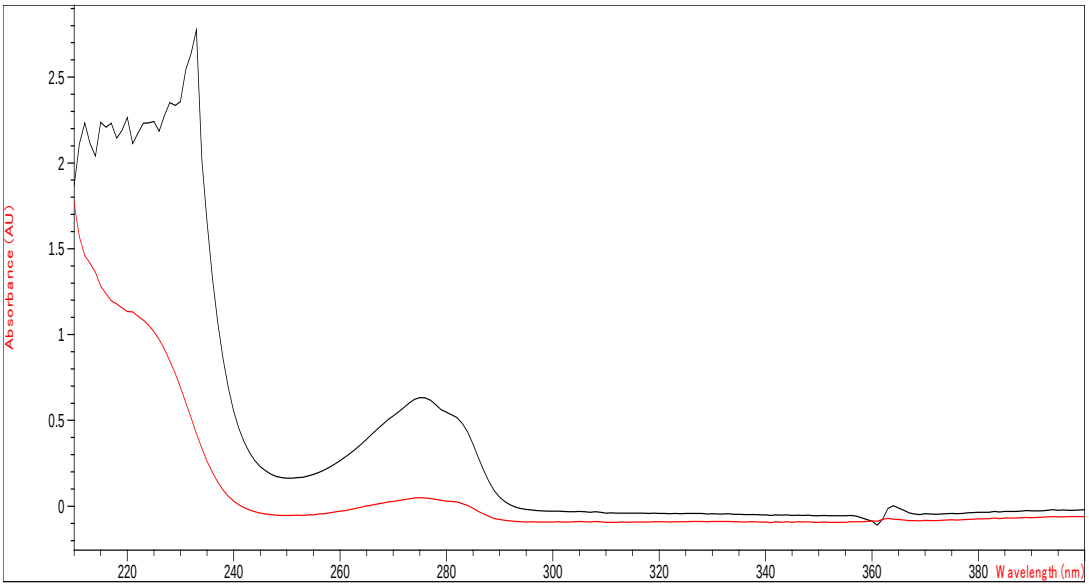

Figure 65. UV spectrum of CDEX70-3-pyrrol-O-11 peptide (in black) and 11 peptide released from the nanocarrier (in red). ʎmax = 275 nm.

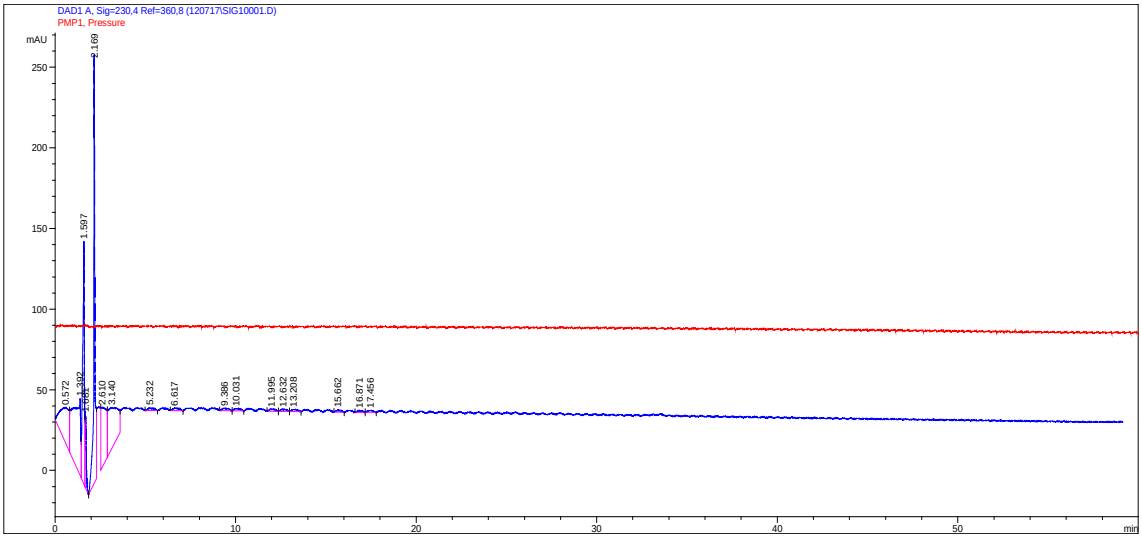

Figure 66. Chromatogram of the phosphate buffer, vehicle where the sample was dissolved.

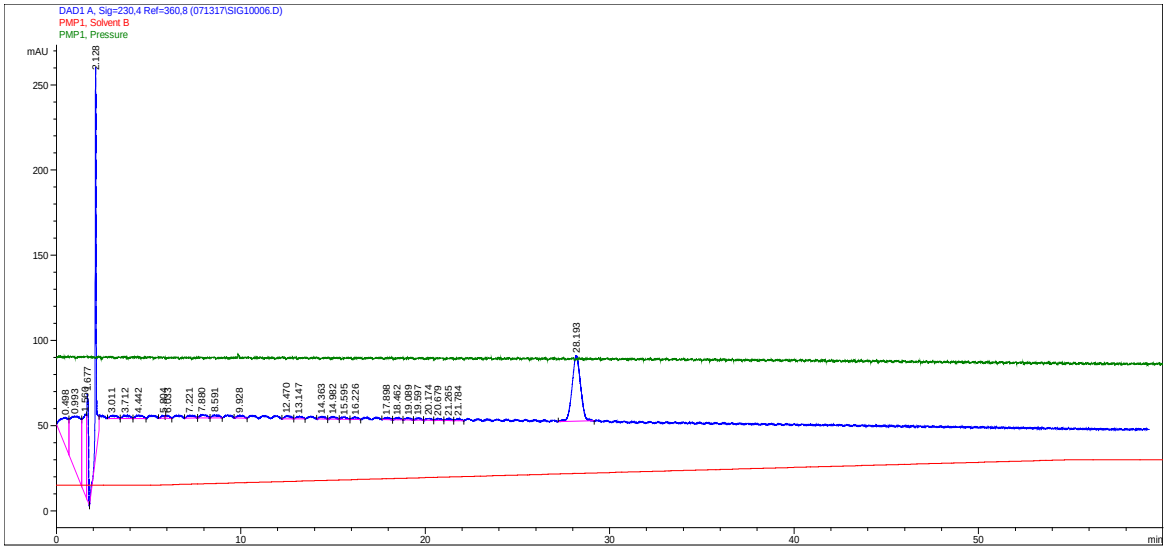

Figure 67. Chromatogram of 11 peptide (100 µg/mL in water), reference standard. Retention of time: 28.2 min.

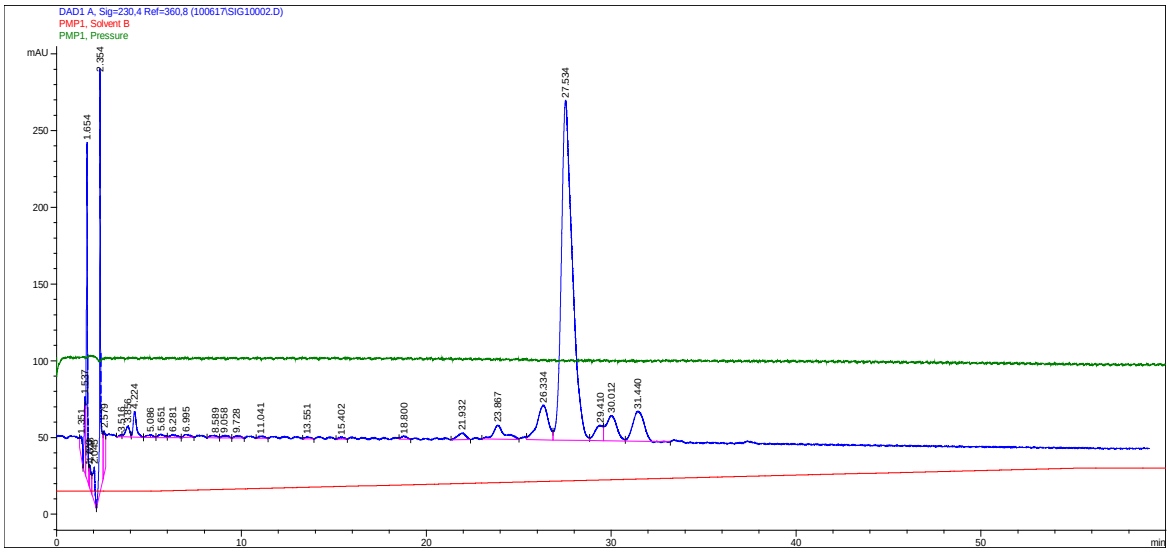

Figure 68. Chromatogram of 11 peptide released from CDEX70-3-pyrrol-O-11 peptide. Retention of time: 27.5 min. Other peaks might be new compounds of side reactions.

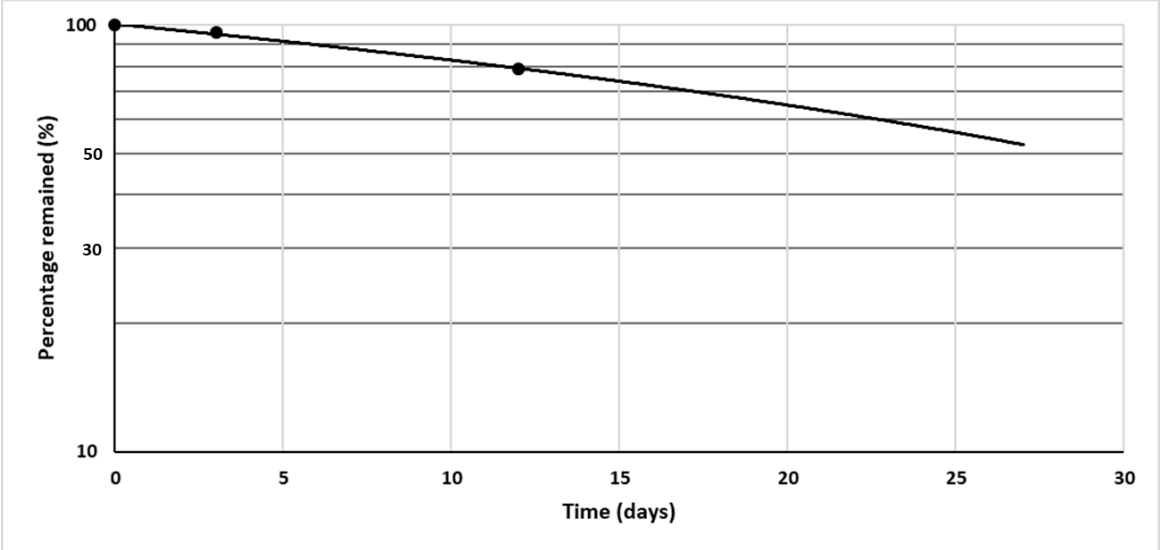

Figure 69. Semi-log representation of the half-life of the conjugate CDEX70-3-pyrrol-O-11 peptide.

4.5 In vivo efficacy experiment of CDEX70-3-pyrrol-O-11 peptide study in mice eye

All the mice were euthanized after 30 days post injection. The eyes were collected and the surface of vessels in the retina was calculated. Figure 70 shows a bar graph of the mean area of CNV in μm^2 after two weeks after the laser treatment. There is a difference between the vehicle and the CDEX70-3-pyrrol-O-11 peptide, but according to the statistics there was not difference between vehicle *vs* free peptide and free peptide *vs* CDEX70-3-pyrrol-O-11 peptide. As a preliminary experiment, the NPC shows a slightly improve in comparison with the free 11 peptide. This will require further experiments to achieve a solid result which shows a significance efficacy improve of CDEX70-3-pyrrol-O-11 peptide *vs* free 11 peptide.

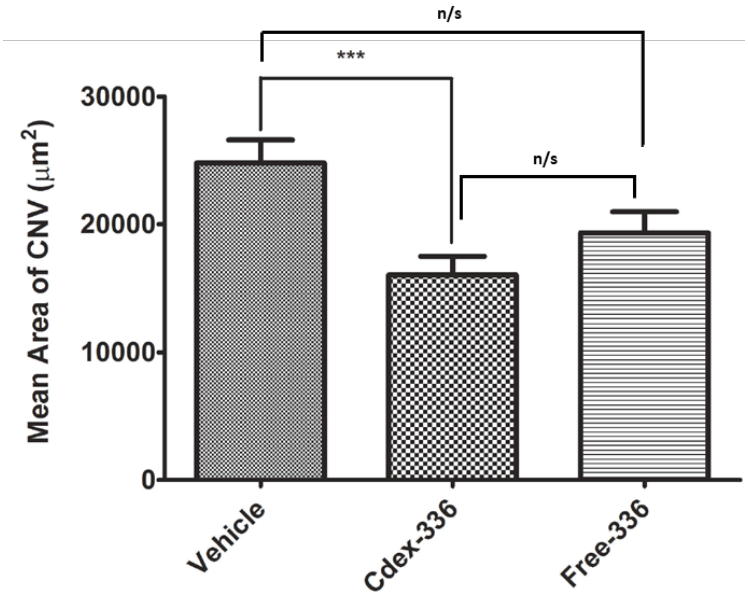

Figure 70. Bars representation of the mean area of CNV in the retina of mice eyes at 14 days after the laser treatment. The statistical analysis (one way ANOVA) has shown that there is a difference between vehicle *vs* CDEX70-3-pyrrol-O- adipic-11 peptide but not in the other two cases. (P value: 0.0012; P <0.05). (336 stands for 11 peptide).

Discussion

Sustained intraocular drug delivery for posterior disease is an urgent need in ophthalmology [324]. Both increased lifespan and improved neonatology have increased devastating neovascular diseases in the very elderly and also the very youngest and smallest in humanity, as with exudative AMD and ROP [101, 325]. Diabetes, also with increasing incidence, leads to similar neovascular disease [58, 326], while glaucoma and posterior inflammation take an enormous toll, adding to the worldwide suffering from blindness [327]. Drug exposure to the relevant intraocular and choroidal tissues is a challenging problem as these are not readily accessed from the circulation or through eye drops. Both protein agents and especially small molecules, given via IVT injection, exit the eye rapidly, with each repeated injection taking a great toll on this fragile organ, in already very burdened patients [199, 207, 210, 211, 216]. Making a single IVT injection last for several months is thus a major goal in visual science[328]. Recent studies find that microparticles induce a strong and damaging foreign body reaction in primate eyes [283], and that

intraocular tissues are exceptionally sensitive to even low amounts of endotoxin [329]. These observations place additional hurdles in the developmental paths microparticles and liposome or micellar carriers, the latter being difficult to free of endotoxin and both difficult to sterilize [330].

Nanotechnology presents the new alternative for posterior delivery of drugs and genes, to reduce injection frequency, improve compliance and patient outcome, and includes a variety of devices and materials to enhance access [331]. MP and NP, comprising liposome or micellar structures, have also been utilized, including for gene therapy [332]. Several cases have described new prolonged drug delivery systems as a thermosensitive gel as drug delivery system using a polymer called poly(ethylene glycol)-poly(serinol hexamethylene urethane) (ESHU), which turns from sol to gel at 37 degrees and releasing bevacizumab in 17 weeks [333]. In this formulation the particle size was impossible to control, driving it to the formation of aggregates and giving as a result large particles that could trigger inflammation.

Here we defined a sterile-filterable, cationic NP system for sustained IVT residence, where diameter <100 nm makes foreign body response unlikely. No signs of inflammation were observed in the eyes of any of our test animals.

Our strategy was the design of a conjugated dextran nanoparticle, CDEX (condensed dextran) formed from dextran polymer (Mw: 70,000 g/mol). It was chosen because of its extensive use in parenteral administrations as plasma expander and reducing blood viscosity and its use for ophthalmic drugs in the current medicine [334-337]and its property of excretion through the kidney. As condensing agent, it is possible to use fatty acids [338, 339] or cholesterol. Using cholesterol chloroformate as condensing agent provides dextran the capacity of solubility in organic solvents, forcing the dextran polymer to form compact nanoparticles and enables the transport of hydrophilic drug molecules. CDEX takes on a conformation leaving inside the hydrophobic domain core with the property of loading small lipophilic drug on its core (without exceeding 10 –100 µg/mg), such as brimonidine, sirolimus, doxorubicin, or taxanes. Kinetic release studies are necessary to support this application. The outside surface of the nanoparticle facing the aqueous environment has 365 glycosyl monomers sites to potentially carry hydrophilic drugs as peptides [316, 340]. Approximately half of 125 activated *p*-nP carbonates were pyrrolidine-PEG-peptide linked in our rabbit eye experiments, the remainder being discharged with amino-PEG.

Alternatively, in a similar case, it should have been possible to replace the 60-65 PEG-amine groups with a pyrrolidin-3-ol ester of any carboxylated drug. More than 100 such prodrug molecules could be simultaneously appended with more intense charging. Other alternatives are anti-VEGF proteins. These can likely be attached at 1-3 moles per NPC through disulfide bonds with cysteine peptides where intraocular glutathione drives release, or via esters bridging protein-SH and NPC cysteines through bifunctional linkers, related to those discussed here. Another option is to link small-molecule carboxylated drugs as diclofenac, methotrexate and peptides directly or, preferably, using amine-ester bridges, such as those we have characterized. Adherence to IVT HA, without use of charge interactions, has also been recently employed, attempting to prolong the IVT residence of anti-VEGF proteins. Fusion of an anti-VEGF Fab fragment and 97-amino-acid LINK domain of a hyaladherin protein (TSG-6) gave 30-fold higher IVT Fab fusion protein at 30 days, post-injection IVT in rabbits, compared with ranibizumab at 21 days [341]. Possible liabilities include a novel epitope at the fusion site, and the LINK region affecting CNS function of the same protein [342].

In our approach, NPC adherence relies only on multiple weak charge associations with HA, without resorting to novel recombinant protein fusions. The advantages of the NP are its solubility in aqueous solution, its size of 38-58 nm and the transparency. These features avoid the risk of their precipitation in the vitreous, the small size prevents the attack by macrophages and the transparency avoids opacity inside the eye.

Manufacturing lipid NP is problematic because of their high affinity for endotoxin [330], inserted in their structure, and the finding that tissue-contacting vitreous is exceptionally sensitive to endotoxin [329]. Cationic particles, as described here, also attract anionic endotoxin micelles but, without surface lipid, the latter can be removed by immobilized poly-histidine [343], when needed.

Our first specific aim was to prolong NP residence in the vitreous through poly-cationic interaction of carriers with poly-anionic vitreal components. Using L-Arg makes a safer cationic NP due the capacity of cells to detoxify L-Arg through the presence in the retina of type 2 enzyme of peptidyl arginine deiminases (PAD), which converts them into citrulline [344-346]. The slow diffusion of the particles increases the time of enzymatic detoxification [316]. We have synthesized two different (without bioactivity) anchor peptides with five amino acid sequences each and a small PEG chain of 8 units followed

by a pyrrolidine group. To reduce the immunogenicity in the *in vivo* experiment, the sequences were mimicked from three proteins which are naturally present in the vitreous. The PEDF protein (residues 66-70) [133] for the two arginine peptide and Hsp20 chaperone protein and the type A α-Crystallin protein (residues 121-125) [347] for the three arginine peptide, also in both peptides, there is tyrosine to identify and quantify the amount of peptide per particle. The success in the high controlled conjugation of peptides per NP through a carbamate bond lies on two factors:

1) The *p*-nPCOCl activation which has a higher coupling yield than *N,N*-Carbonyldiimidazole (CDI) [316] due to the high sensitivity of CDI to atmospheric moisture, been affected even in unopened containers [348]. With these new conditions, we have typically activated 150 hydroxyl groups of the NP, with certainly of quantification, and the ability to confirm complete discharge of all *p*-nP groups.

2) Modification of the linker by secondary amines (pyrrolidine) that are more reactive to conjugate compounds than primary amines, reaching a difference of 50% of conjugates. This observation is corroborated with the conjugation of the DNP ester compounds (Table VI).

Controlling the amount of base is crucial for the conjugation process: large amount of this reagent reacts with tyrosine changing its maximum absorbance, and thus to its structure a possibly to its safety and efficacy effects (data not shown). Thus, we conclude that the unexpected reactivity here arises from a favorable reaction of 3-substitued pyrrolidines (carboxyl or hydroxyl) with *p*-nP mixed carbonates.

If it is desired to have an exceptionally stable ester prodrug such as was found here in the case of (trans) 4-aminocyclohexanol, (half-life near 80 days) its attachment would be hampered by the low direct yield it displayed in CDEX carbamate formation. It would probably be necessary to first cap the cyclohexylamine group with a pyrrolidyl group to affect simultaneously both a good yield and maximal prodrug stability.

We have used two different techniques to quantify the amount of peptides per CDEX, BCA (a protein quantification assay based on colorimetry) and UV, which quantifies the amino-acid tyrosine. Tyr is present in both peptides. With the two quantification methods, we have similar values of peptides per CDEX, more than 60. The observed difference could be due to the fact that the peptides are in the threshold to be quantified by BCA but the CDEX particle might affect the background when measured by UV. As an alternative

quantification method we propose to use in the future the nitration reaction of Tyr by tetranitromethane, as described by Bakhoj and Heegaard in 1999 [349]. This will move the Tyr absorbance to a longer wavelength (NO_2-Tyr 360-400 nm), far from the confounding light scattering of the NPs. We have demonstrated that *p*-nPCOCl activation pathway increases the chances of conjugating more peptides than the CDI activation pathway [316]. Most importantly, the active intermediate can be isolated. Moreover, the *p*-nP charge levels can be evaluated in real time to keep the synthesis well controlled and reproducible.

As *in vivo* model, we selected the rabbit eye due to the similarities with the human eye and because there are not significant differences in pharmacokinetics between the human and rabbit vitreous. [277, 350]. As a major improvement, we have used as cyanine7 (Cy7) dye instead of the rhodamine (Rh), as in the Li *et al*. publication. The advantages of using Cy7 instead of Rh are that 1) Cy7 is 60 times more sensitive than Rh and 2) its maximum wavelength is in the long visible spectrum (745 nm) while the Rh maximum is 540 nm [351]. With this wavelength is highly improbable that a signal overlap occurs between the probe and the tyrosine (λ = 275 nm) during the experiment. With Rh, fluorescence detection must be accomplished through the pupil, requiring specialized equipment and eye immobilization. We succeed in measuring Cy7 fluorescence in a simple IVIS instrument designed for luminescence studies in rodents. This rapidly quantified 800 nm emission through the sclera and lid, in freely moving eyes of mildly anesthetized young rabbits. A recent study used Cy7 injected in the hearts of rabbits, which allowed to track the distribution of the dye *ex vivo* using a chamber very similar to the IVIS instrument. The same dye was also used to track bone-targeted NP in mice using the IVIS instrument. [352, 353]. Regardless of the type of particle used for intraocular delivery, we have demonstrated that Cy7 labeling enables simplified time-residence measurement in eyes of small- to medium-sized animals, which should itself be a significant contribution to imaging in ophthalmology.

We might preformulate the NPC with Healon [182] to increase their residence in the vitreous of patients who have a lack of HA due to their age or after being operated of vitrectomy. We should test the residence of this mixture in a rabbit vitrectomy model.

Our second aim was the design of the amino ester bridge, as used in the peptide 11. To characterize a range of useful bridged esters, we selected the amino alcohol compounds for the left side of the molecule. We expanded on a report from the US Environment Protection

Agency (EPA) (2006)[321] where they studied the ester hydrolysis in unbuffered water of varied organic esters. They observed that the rate of hydrolysis is related to the nature of the hydroxyl group used to generate the ester bond (primary, secondary or tertiary). For the right side of the molecule, we selected glutaryl and adipoyl according to the description of how the length of the alkyl chains affect ester stability [354].

The synthesis of complex esters presented many challenges, since esters are energetically uphill from their component carboxylic acids and alcohols. They are also highly reactive dehydrating agents, which are not readily applicable to peptides or carbohydrate polymers. Phase transfer reaction was a successful reaction to get the amino ester prodrugs: we did not reach the same range of yields as other authors (up to 80%) [355], probably due to solvent replacement. Moreover, our potassium compounds precipitated in *N,N*-dimethylformamide (DMF), possibly due the nature of the mixed solvent we used which requires an optimization of conditions. On the other hand, with the transesterification reaction, it was difficult to obtain good yields of ester product. It is critical for the product to eliminate the MeOH generated during the reaction. The presence of MeOH reacts with the ester product giving the starting material. Low yields were reached with secondary alcohols due to their low reactivity on this type of reaction [356-359].

Ester hydrolysis rate studies of the Boc-N-R-O-spacer-aa-O-tbut cmpd have shown that the nature of the hydroxyl groups affects the speed of ester hydrolysis, being the speed of degradation secondary alcohols >primary alcohols[321]. The molecule conformation affects the speed of hydrolysis, especially when bulky substituents such as Boc or polysaccharide are present. The axial conformation (19) reduces the steric influence of the electron density on the oxygen and thus, a reduction in the non-bonded repulsions which increases the probability of the nucleophiles attacking the ester, when compared to the same compound with the equatorial conformation (15) in which the ester is more protected [360]. The same reasoning can be applied when we compare a five-member rings to a six-member rings cmpd, (6 *vs* 7; 17 *vs* 16 and 18 *vs* 16). The proximity of the high electron density of the Boc group reduces the steric influence on the ester bond. As appears the EPA study[321].

The length of the alkyl chain affects the rate of hydrolysis due to the steric effect [354], but an ester breakdown could accelerate it, due to internal cyclization reactions where the amide or N-methyl-amide nitrogen of the amino acids (Gly or Sar) attack the carbonyl

group of the ester, displacing the amino-alcohol. Increasing the distance between the amine of the amino acid and the carbonyl group is critical to improve the probability to avoid side reactions [323]. The ester hydrolysis of the model compound corroborated all our findings, the proximity of high electron density of the Boc group and the elongation of the amine from the ester reduce the speed of ester hydrolysis. Moreover, the flat aromatic conformation of the pyrrolidine reduces the possibility of water reaching the ester bond and causing the cleavage [361]. In the future, to reduce the ester hydrolysis by external conditions, we will have to carefully select the conformation of the rings, the length of the alkyl chains and the use of methylate amines in the amino acids. We propose to study this with different alkyl chains to understand the relationship between the alkyl length chain and the speed of hydrolysis. The suberic (8 carbon) dicarboxylic acid may minimize cyclic side reactions as well.

The conjugation of the free amine-DNP ester compounds has shown high of DNP/ NP when a secondary amine (pyrrolidine) reacts (data not shown). There is not literature about carbamoylation reactions with *p*-nP and the nature of the amines. Release studies from DNP have shown the real effect of amino-alcohols on the speed of hydrolysis without interference from cyclization side reactions [323] and the steric influence of the electron density [360].

Our third aim was to select a potent anti-angiogenic and anti-CNV peptide amenable to prodrug linkage, hoping to extend the duration of its IVT action. The active anti-angiogenic PEDF region is located in the 34-mer epitope, an anti-angiogenic 34-amino acid N-terminal peptide has been shortened to 18 residues[135], which it was truncated to 9 amino acids (P3-11), that retains anti-angiogenic activity (Figures 5, 71 and 72).

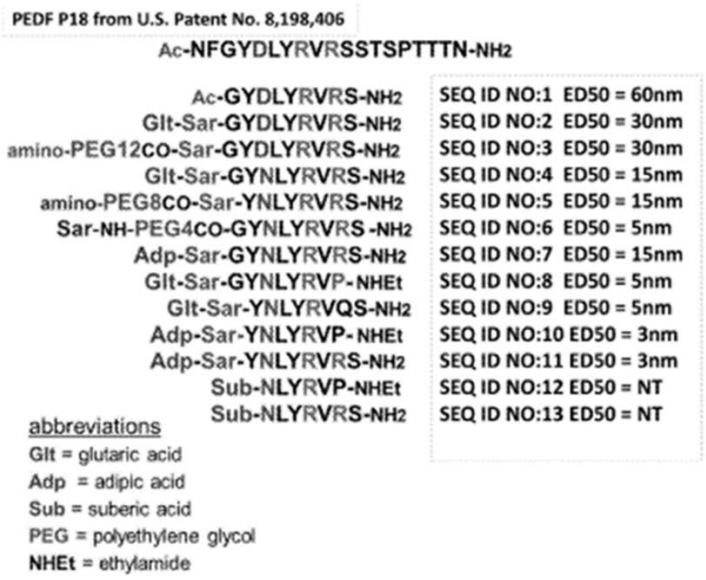

Figure 71. Novel modified peptides and new peptide sequences as exemplified by SEQ ID Nos: 1–13. The ED_{50} (50% effective dose), is the measure of anti-angiogenic potency obtained by quantitative assessment of apoptosis of activated human EC. Source: Henkin et al, 2017 [237].

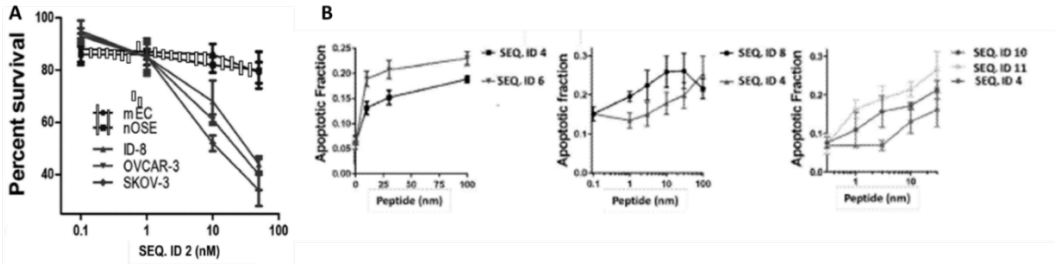

Figure 72. ED_{50} *in vitro* experiment of the anti-angiogenic peptides. A. Selective killing of the ovarian cancer cells by SEQ ID N0:2. Ovarian cancer cells (ID-8, OVCAR-3 and SKOV-3 cell lines) normal ovarian epithelial cells (nOSE) and unstimulated mouse endothelial cells (mEC) were treated with increasing concentrations of SEQ ID N0:2 and survival was measured using a WST assay. **B.** Relative potency of peptides at inducing EC apoptosis. Human microvascular EC (HMVEC) were seeded on glass coverslips and grown in EGM, supplemented with defined growth factors and full serum (5%) to 80–90% confluence. The cells were trans-ferred overnight in the medium with 1% serum, w/o growth factors. VEGF (10 ng/mL) was added to induce pro-angiogenic function/survival. Peptides were added at indicated concentrations. After 48 h the cells were fixed in 1% buffered paraformaldehyde and apoptosis detected by in situ TUNEL. Apoptotic cells were quantified in ≈10x fields per condition and apoptotic fraction (apoptotic/total cells) calculated for each condition. Apoptosis induced in EC by indicated peptides (SEQ ID N0:6, 8, 10, and 11) is compared to SEQ ID N0:4. Source: Henkin et al, 2017[237].

After the initial screening, Peptide Seq ID No: 1 was tested *ex vivo* in a choroidal sprouting assay. Results showed an antiangiogenic choroidal activity (Figure 73). *In vivo* experiment of the Laser-induced CNV in mice of the most potent peptides, adipic-SEQ No. 10 (10

peptide) and adipic-SEQ No. 11 (11 peptide), were showed a significant anti-angiogenic effect of choroidal vascularization (Figure 74).

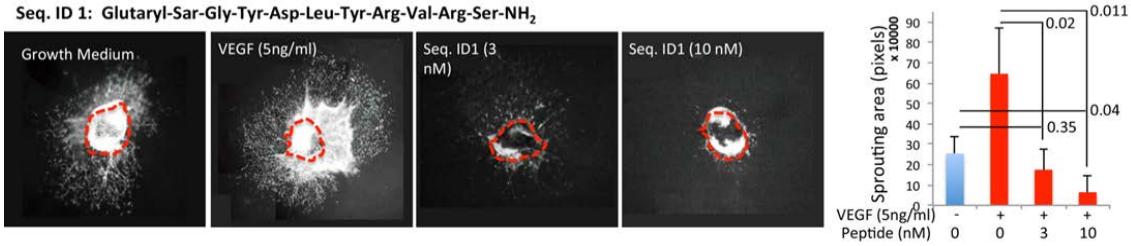

Figure 73. Inhibition of choroidal angiogenesis by conjugable P3-11. Choroidal explants from Actin-GFP mice are plated in Matrigel and maintained with or without VEGF for additional capillary spouting. Peptide Glt-Sar-P3-11 was added in the presence of VEGF. Fluorescence images were taken and sprouting area measured after 6 days using Elements software (Nikon). Statistical significance was determined by pairwise comparisons with two-tailed Student's t-test. P<0.05 was set as significant. Source: Henkin lab. Northwestern University (manuscript in preparation).

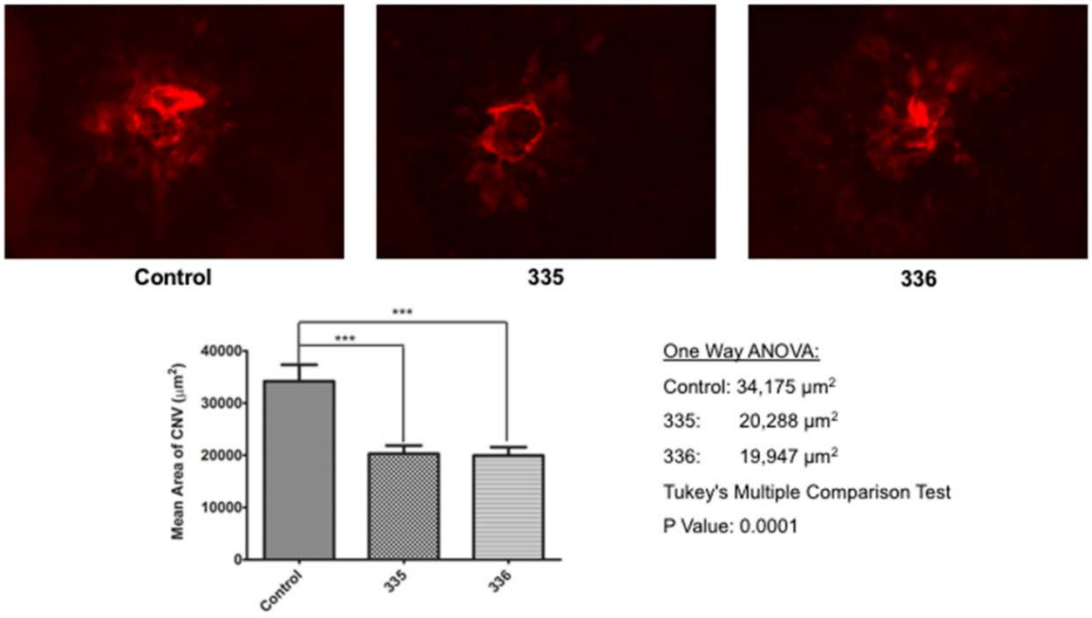

Figure 74. *In vivo* experiment of the Laser-induced CNV in mice of the 10 peptide (named 335) and 11 peptide (named 336). The statistical analysis (one way ANOVA) shows a significant difference between 10 peptide *vs* control and 11 peptide *vs* control. (P<0.001). Source: Henkin lab and Sheibani lab. University of Wisconsin-Madison (manuscript in preparation).

Due to the potency and polarity of the 10 peptide, was administrated at 10 mM as eye drops in mice using the Laser-induced CNV model. Peptide was administered every 2 days, 18 days before the laser-induced lesion, skipping the weekends. Results showed statistical difference with the control Figure 75. In rabbits, the amount of peptide which reached the

posterior area was not significant due to the difference of size of the eye and the thickness of tissues. This peptide might not be useful for the posterior area of the eye but could have applications in the front of the eye (manuscript in preparation).

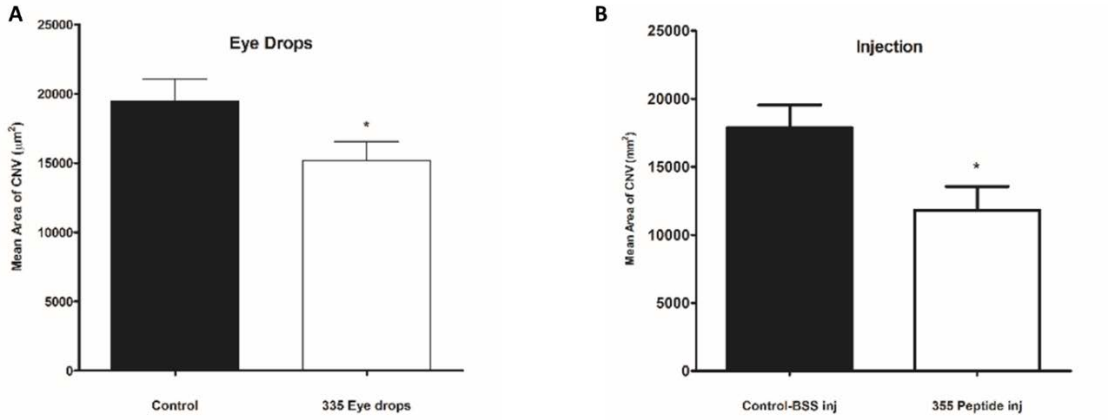

Figure 75. *In vivo* experiment of the Laser-induced CNV in mice of the 10 peptide (named 335). A: Administration of 335 10 mM by eye drops. The statistical analysis (one way ANOVA) shows a significant difference between 10 peptide *vs* control. ($P<0.1$). **B:** Administration of 335 2 mM by intravitreal injection. The statistical analysis (one way ANOVA) shows a significant difference between 10 peptide *vs* control. ($P<0.1$). Source: Henkin lab and Sheibani lab. University of Wisconsin-Madison (manuscript in preparation).

11 peptide (also known as 336) is a potent antiangiogenic (ED_{50} = 3 nM) and containins 2 Arg residues, that might allow it to simultaneously be an anchor and a prodrug. This peptide also contains *N*-terminal adipic half amide intended for ester prodrug formation, and a modified compensating internal sequence change, where an Asp-3 from PEDF is exchanged to asparagine. It was potent by IVT injection in blocking laser induced mouse CNV, when injected 2-4 days before laser induction. This requires a slow hydrolysis ester prodrug of 11 peptide attached to CDEX.

Since the deprotection of the Boc-amine (cmpd 6, intended 11 peptide prodrug precursor) was faster than the *tert*-butyl-carboxyl ester in the de-blocking reaction (due to the second-order dependence upon the acid concentration[362], we had to redesign the synthesis pathway achieving the desired compound in a one-step synthesis pathway. During the reaction we used and excess of the double diacyl chloride compound to reduce the probability of producing the bis-ester. For the future, we will adjust the number of equivalents to increase the yield. The conjugation of the peptide to CDEX following the

same procedure as the previous compounds yielded the targeted number of conjugates per NP (57 peptides per NPC).

The half-life of hydrolysis of the ester of CDEX70-3-pyrrol-O-11 (28 days) matches the half-life of hydrolysis of Boc-3-pyrrol-O-adp-Gly-O-tbut. The proximity of the nanocarrier to the ester had the same function as the Boc but with different behavior. Meanwhile the Boc group repelled the proximity of the water to the ester bond due to its hydrophobicity. Due to its size, CDEX would only modestly protect the ester bond from attack by water. Another reason is that the peptide has the amino acid sarcosine instead the amino acid glycine as the previous study. Sarcosine is a methylated glycine on its N terminus, and it should be less internally reactive to cyclization releasing the 11 peptide sooner than expected, as described by Yano in 2000 [363].

Preliminary results have shown only a mild improvement in terms of efficacy when using the NPC *vs* the free peptide in an *in vivo* model of Laser-induced CNV (Figure 70). The release of the free peptide was longer than expected, due to the ionic bonds between the Arg and HA. This will require further experiments spacing the time between the IVT injection and the laser induction to clearly demonstrate the efficacy of NPC. These results are consistent with the prolonged protection by CDEX70-3-pyrrol-O-11 peptide given at day-14 before laser induction, against CNV, compared with no treatment the difference being statistically significant. The free peptide given at day-14 still shows a tendency to be protective, although it is not statistically significant. We are starting new experiments with injections at day-28, in which we expect that all the free peptide will be eliminated at the time of the laser induction but our NPC will still be pharmacologically active.

Here we have described some key factors, which increase ester hydrolysis rates. Even, on these circumstances, we got two ester prodrugs with different prolonged hydrolysis rates. After we have shown the variables that, we have to control to get high yields of conjugation with the NP. The efficacy results were not conclusive due the space of time between the injection and the laser induction.

Conclusions/ Conclusiones

Conclusions

1. 60 pyrrolidine-PEG-peptides with 2 L-arginines and 3 L-arginines per nanoparticle were loaded due to the high controlled conjugation factors: 1. the activation of the nanoparticles with *p*-nitrophenyl chloroformate and 2. using pyrrolidine as a reactive amine in the carbamoylation reaction. Preload of p-nitrophenyl suggests that 50-80 anchor peptides along with 2-50 ester prodrug aminoalkoxyesters is an attainable target.

2. The presence of positive charges (L-arginines) and the increase of zeta potential decrease the rate of diffusion of the conjugate nanoparticles, and they reduce their rate of intravitreal elimination. The half-life of residence has been related to zeta potentials (range +3.9 to +6.3 mV), results that suggest that reproducible half-life of 1-3 weeks is attainable with 2 and 3 L-arginines peptide conjugates at 60 peptides per nanoparticle load.

3. Two arginines peptides conjugated to nanoparticles at 12 mg/mL have not shown any type of inflammation response in rabbit eyes. The slow diffusion of the particles not exceeded the enzymatic detoxification capacity.

4. Three amine ester compounds have been described conjugated to condensed dextran nanoparticles with a half-life between 40 and 81 days. The distance of the amine group to the ester bond has a critical effect on the prevention of side reactions cyclization. Suberic peptides may improve this (9 membered rings form slowly).

5. A pyrrolidin-ester peptide prodrug conjugated to a nanoparticle has been designed with a half-life of 28 days. Efficacy studies in the laser-induced CNV model have shown promising preliminary results, although it has not found differences between the free peptide and the nanoparticle, due to the short space of time between the administration of the compounds and the laser-induced lesion.

Conclusiones

1. Se han conjugado 60 pirrolidin-PEG-péptidos con 2 L-argininas y 3 L-argininas por nanopartícula debido al control de los factores de la reacción de conjugación: 1. la activación de las nanopartículas con cloroformiato de *p*-nitrofenilo y 2. el uso de pirrolidina como amina reactiva en la reacción de carbamilación. La carga de *p*-nitrofenilo sugiere que 50-80 péptidos de anclaje junto con 2-50 profármacos de amino-éster es un objetivo alcanzable.

2. La presencia de cargas positivas (L-argininas) y el aumento del potencial zeta disminuyen la velocidad de difusión de las nanopartículas conjugadas, reduciendo a su vez la velocidad de eliminación intravítrea. Se ha relacionado la vida media de residencia con los potenciales zeta (rango +3.9 a +6.3 mV), resultados que sugieren que la vida media de 1 a 3 semanas es alcanzable con péptidos de 2 y 3 L-argininas conjugando 60 péptidos por nanopartícula.

3. Los péptidos de dos argininas conjugados a nanopartículas a una concentración de 12 mg/mL no han mostrado ningún tipo de respuesta inflamatoria en ojo de conejo, debido a que la lenta difusión de las partículas no excede la capacidad desintoxicación enzimática.

4. Se han descrito tres compuestos amino-estér conjugados a nanopartículas de dextrano condensado que poseen una vida media entre 40 y 81 días. La distancia del grupo amina al enlace éster tiene un efecto crítico para la prevención de reacciones secundarias de

ciclación. Péptidos subéricos podrían mejorar esto (la velocidad de formación de anillos de 9 miembros es muy lenta).

5. Se ha diseñado un profármaco formado por un péptido de pirrolidín-éster conjugado a una nanopartícula con una vida media de 28 días. Los estudios preliminares de eficacia en el modelo CNV inducido por láser han mostrado unos resultados prometedores, aunque no han mostrado diferencia con el péptido libre debido al corto espacio de tiempo entre la administración de los compuestos y la inducción de la lesión ocular con el láser.

Future directions

The IVT diffusion of the NP described here in rabbit eyes corroborates the results of Xu et al, 2013 [12] and Li et al, 2017 [316] in a different experimental system, and, importantly, without cell damage in a live animal, with intact circulation and eye drainage, rather than in isolated bovine eyes post slaughter. The presence of positive charges (arginines) and the increase of zeta potential, decrease the rate of diffusion of the NPC, reducing their rate of IVT elimination. We related the half-life of residence to zeta potentials (range +3.9 to +6.3 mV), results suggesting that reproducible $t_{1/2}$ of 1-3 weeks is attainable with 2R- and 3R-peptides conjugates at 60 peptides/ NP load. This, combined with the previous results with Rh tagged NPC [316], suggests that the use of a 4R-peptide, available in 5-8 amino acid fragments of protamine 1, attached at similar loading, could yield a zeta potential in the range of +10 to +15 mV reaching a half-life of residence of 6-8 weeks. Pharmacokinetic, vitreous capacity and safety studies would be performance to assure the safety and efficacy of the 4R-NPC.

Here we concluded that doubling NPC zeta potential roughly increases ocular residence half-life by 2.5 to 3- fold in going from 2R to 3R conjugates. The original Rh-tagged NPC underwent doubling of zeta potential where the linked peptide went from 2-3 Arg, and doubled again when increasing from 3-4 Arg [316]. Thus, we extrapolate that a 4 Arg peptide, similarly loaded, would increase rabbit eye half-life to between 40-60 days. With an ester prodrug attached, intraocular cargo available at times after injection would decline both NPC lost from the eye and the ester lost by hydrolysis. Having largely succeeded in achieving our specific aims, we now wish to show the usefulness of their convergence in offering the promise of addressing an unmet medical need. Thus, we now extrapolate our results to a real world-situation concerning the current treatment of AMD, for which our finding may improve therapy. Lucentis (ranibizumab), approved and widely used for therapy of AMD, is a 50kDa Fab fragment which binds and neutralizes VEGF. Its typical IVT dose in affected elder eyes is 500 µg and it is typically injected at 4 to 6-week intervals. Given its half-life of 8 days the total available in the eye is expected to be 50 µg, 14 µg, and 2 µg at 4, 6 and 8 weeks post-injection, respectively. Not surprisingly, discussions with Genentech indicate they would be pleased to have a release system which maintains >4 µg at 90 days, or beyond. This would reduce the burden on patients significantly.

We should vary some CDEX conditions to improve its capacity. 1. The cholesterol core percentage and the collesterollinkage to the sugar through carbamates instead carbonate bonds (eg: link *N*-Boc-amino-PEG_3-amine to *p*-nP activated dextran, then add the cholesterol chloroformate to amine after Boc removal). 2. The dextran size (40 *vs* 70 kDa) to maximize the conjugation yield of peptides to CDEX. Moreover, we need to demonstrate carboxy drugs (eg: diclofenac) conjugation and release rates and show delivery as amino-pyrrolidine ester on surface. Also, if half the surface Arg (say 90 Arg) are loaded to bind phosphate groups of nucleic acid, the genetic material should slowly be released when phosphates are replaced by HA carboxylates as the the NPC slowly spread out in vitreous. Arg deiminases will release even more as these reach the cells on the inner eye surface [313] [364] [345]. As another strategy, we propose to study lipophilic drugs imbibed in the core (eg: rapamycin, brimonidine, doxorubicin).

We have defined small amino alcohol bridges where the amine links stably to polycationic CDEX NPC, the OH group is esterified to ordinary COOH groups. Two of these bridges are especially useful and we find they respectively give 40-day and 80-day spontaneous ester hydrolysis half-lives respectively under physiologic conditions.

Our experience suggests that each additional L-Arg residue (after 2 Arg) per small conjugated peptide, doubles the zeta potential at similar anchor-peptide loading. Also, we observed that doubling zeta potential increases IVT residence half-life by 2.5-3 fold. We thus believe that using a 4 Arg peptide at loads of 50-60 peptides per NPC, we will achieve rabbit IVT residence half-lives of 40-60 days.

As we have two ester bridges with different slow hydrolysis rates (ester made with pyrrolidin-ol: $t_{1/2}$ = 40 days and ester made with t,4-aminocyclohexanol $t_{1/2}$ = 80 days) we can prepare NPC with varied loads of 4R anchor peptide aiming for two different zeta potentials, one in the range of +10- +12 mV and another of the range of +12- +15 mV). With these values, we anticipate approximately $t_{1/2}$ residences of 40 days for the first one and 60 days for the second one. Assuming 600 µg of ranibizumab is injected in 1:1 mass ratio with NPC, the rate of release of the peptide is approximately 1 µg per day, after 90 days. The dose will be 1 µg/eye but assuming the accumulation of drug from the previous days, the total IVT content will be on day 90, 8 µg/eye. Figure 76 shows the formulas that we have used to make these calculations. In Table XI, appears the calculation based on a first order decay of the release rate of ranibizumab esterified to our carriers, as a function of time post IVT injection. The calculations were made for two residence half-lives.

$$\frac{C}{C_o} = e^{-kt} \qquad -k = t_{1/2} / 0.693$$

1/(k) = fractional loss per day

Figure 76. This formula describes monoexponential decay in monocompartimental model. We calculated first order loss of Fab fragment by NPC IVT-exit diffusion or by ester hydrolysis.

Table XI Amount of Fab per day per eye released from the NPC

	Particle residence $t_{1/2}$	40 days	40 days	60 days	60 days
	Ester hydrolysis $t_{1/2}$	40 days	80 days	40 days	80 days
	Daily loss factor, k	0.017	0.0087	0.017	0.0087
Fraction remaining on	Day 30	0.35 (210 µg)	0.45 (270 µg)	0.15 (90 µg)	0.19 (114 µg)
	Day 70			0.132 (79 µg)	0.238 (143 µg)
	Day 90			0.08 (47 µg)	0.166 (99 µg)
	Day 120	0.017 (10 µg)	0.047 (28 µg)	0.033 (20 µg)	0.09 (54 µg)
µg/day/eye day	Day 30	3.6	2.3	1.5	1.0
	Day 70	1.4	1.2	1.34	1.24
	Day 90			0.8	0.86
	Day 120	0.17	0.24	0.34	0.47

Underlined: k value.

Liquefaction of the vitreous is a regular process that increases with the age. After the 60's the production of liquid vitreous reaches a 50% affecting the diffusion of the NP [177]. As in our study we used young rabbits, one might think that the residence of the NP cannot be extrapolated to elderly people. However, rabbit eye NPC capacity is expected to be at least several-fold lower than human eyes, which have been estimated to contain 6-8 times greater HA content per mL. The residence of the NP extrapolated to human vitreous could show a slower speed of diffusion. Also, according to Denlinger and Balazs[178], while the liquefaction of the vitreous, the amount of hyaluronic acid increases after the 70's and this could partially substitute the lack of viscosity conjugating more peptides with arginines to create ionic bonds with these new poly-anion molecules. This can be best addressed by comparing NPC diffusion directly when added to freshly obtained rabbit vitreous, with human samples from enucleation surgery or cadavers.

Our results on the 2R-NPC samples have shown a correlation between the fluorescence signal and concentration with 3 and 6 mg/mL samples. This proportionality was remained

during the entire study until the experiment reached after the third week, where the signal value of 3 and 6 mg/mL samples were the same as 0 mg/mL, background.

By contrast, the sample of 12 mg/mL (200 μg of NPC) was rapidly lost, even the time 0 measurement was lower than the measured value with 3 mg/mL. This suggests that the loaded positive charges on the surface of the NPC, exceeded the retention capacity of the hyaluronic acid that when the volume of the vitreous is 1.5-2 mL vitreous. Extrapolating to the human eye, which has a vitreous volume of 4 mL, the same dose of 2R-NPC should be effectively even we could increase the dose, the amount of 2R conjugate peptides or use 3R and 4R peptides. With this particular behavior, the histological studies have not shown any damage in tissues even in the case of the overloaded eyes. Thus, we conclude that cell capacity for L-Arg detoxification is adequate even when diffusion is relatively fast.

In achieving the specific aims of this project, we generated some important and promising contributions to science and medicine. We have identified novel PEDF peptides active vs. CNV, by a non-VEGF mechanism. These may well augment current anti-VEGF therapy, which is less than ideal and may be useful in treating ROP where current Avastin injections are of concern because of their lasting activity systemically in infants. We have developed a promising long-term delivery system for the posterior eye, and systematically discovered a route to ester prodrugs, defining a predictable and useful range of half-lives. We developed a method of quantitatively imaging Cy7-tagged carriers inside the vitreous, using commonly available IVIS instruments. In next steps we hope to collaborate with pharmaceutical partners in the ocular field, in an attempt to improve their current drug delivery by IVT injection.

We also identified a small neutral PEDF peptide (10 peptide) which shows promise in treating anterior neovascular eye disease/corneal disease bi simple eye drop administration. Many such conditions (eg; keratitis) cause significant blindness.

Bibliography

1. Jonasson, P.S., et al., *Strength of the porcine proximal femoral epiphyseal plate: the effect of different loading directions and the role of the perichondrial fibrocartilaginous complex and epiphyseal tubercle - an experimental biomechanical study.* J Exp Orthop, 2014. **1**(1): p. 4.
2. Willis, J.R., et al., *Vision-Related Functional Burden of Diabetic Retinopathy Across Severity Levels in the United States.* JAMA Ophthalmol, 2017. **135**(9): p. 926-932.
3. Booth, B.A., et al., *Sustained-release ophthalmic drug delivery systems for treatment of macular disorders: present and future applications.* Drugs Aging, 2007. **24**(7): p. 581-602.
4. Gaudana, R., et al., *Ocular drug delivery.* AAPS J, 2010. **12**(3): p. 348-60.
5. Del Amo, E.M., et al., *Pharmacokinetic aspects of retinal drug delivery.* Prog Retin Eye Res, 2017. **57**: p. 134-185.

6. Fagan, X.J. and S. Al-Qureshi, *Intravitreal injections: a review of the evidence for best practice.* Clin Exp Ophthalmol, 2013. **41**(5): p. 500-7.
7. Falavarjani, K.G. and Q.D. Nguyen, *Adverse events and complications associated with intravitreal injection of anti-VEGF agents: a review of literature.* Eye (Lond), 2013. **27**(7): p. 787-94.
8. Gibson, J.M. and S. McGinnigle, *Diabetes: Intravitreous ranibizumab for proliferative diabetic retinopathy.* Nat Rev Endocrinol, 2016. **12**(3): p. 130-1.
9. Shen, J., et al., *Ocular pharmacokinetics of intravitreally administered brimonidine and dexamethasone in animal models with and without blood-retinal barrier breakdown.* Invest Ophthalmol Vis Sci, 2014. **55**(2): p. 1056-66.
10. Rosenfeld, P.J., et al., *Tolerability and efficacy of multiple escalating doses of ranibizumab (Lucentis) for neovascular age-related macular degeneration.* Ophthalmology, 2006. **113**(4): p. 623 e1.
11. Jager, R.D., et al., *Risks of intravitreous injection: a comprehensive review.* Retina, 2004. **24**(5): p. 676-98.
12. Xu, Q., et al., *Nanoparticle diffusion in, and microrheology of, the bovine vitreous ex vivo.* J Control Release, 2013. **167**(1): p. 76-84.
13. Klein, R., B.E. Klein, and K.L. Linton, *Prevalence of age-related maculopathy. The Beaver Dam Eye Study.* Ophthalmology, 1992. **99**(6): p. 933-43.
14. Farnoodian, M., et al., *Negative regulators of angiogenesis: important targets for treatment of exudative AMD.* Clin Sci (Lond), 2017. **131**(15): p. 1763-1780.
15. Bird, A.C., et al., *An international classification and grading system for age-related maculopathy and age-related macular degeneration. The International ARM Epidemiological Study Group.* Surv Ophthalmol, 1995. **39**(5): p. 367-74.
16. Jung, J.J., et al., *The incidence of neovascular subtypes in newly diagnosed neovascular age-related macular degeneration.* Am J Ophthalmol, 2014. **158**(4): p. 769-779 e2.
17. Bressler, N.M., S.B. Bressler, and S.L. Fine, *Age-related macular degeneration.* Surv Ophthalmol, 1988. **32**(6): p. 375-413.
18. van Lookeren Campagne, M., et al., *Mechanisms of age-related macular degeneration and therapeutic opportunities.* J Pathol, 2014. **232**(2): p. 151-64.
19. Bhutto, I. and G. Lutty, *Understanding age-related macular degeneration (AMD): relationships between the photoreceptor/retinal pigment epithelium/Bruch's membrane/choriocapillaris complex.* Mol Aspects Med, 2012. **33**(4): p. 295-317.

20. Genentech. *AGE-RELATED MACULAR DEGENERATION (AMD).* 2017; Available from: https://www.gene.com/patients/disease-education/age-related-macular-degeneration.
21. Schmidt-Erfurth, U., et al., *Guidelines for the management of neovascular age-related macular degeneration by the European Society of Retina Specialists (EURETINA).* Br J Ophthalmol, 2014. **98**(9): p. 1144-67.
22. Singh, A., *Systemic changes in neovascular age-related macular degeneration.* Dan Med J, 2014. **61**(6): p. B4872.
23. Curcio, C.A., N.E. Medeiros, and C.L. Millican, *Photoreceptor loss in age-related macular degeneration.* Invest Ophthalmol Vis Sci, 1996. **37**(7): p. 1236-49.
24. Blaauwgeers, H.G., et al., *Polarized vascular endothelial growth factor secretion by human retinal pigment epithelium and localization of vascular endothelial growth factor receptors on the inner choriocapillaris. Evidence for a trophic paracrine relation.* Am J Pathol, 1999. **155**(2): p. 421-8.
25. McLeod, D.S., et al., *Enhanced expression of intracellular adhesion molecule-1 and P-selectin in the diabetic human retina and choroid.* Am J Pathol, 1995. **147**(3): p. 642-53.
26. Wangsa-Wirawan, N.D. and R.A. Linsenmeier, *Retinal oxygen: fundamental and clinical aspects.* Arch Ophthalmol, 2003. **121**(4): p. 547-57.
27. Friedman, E. and S.R. Chandra, *Choroidal blood flow. 3. Effects of oxygen and carbon dioxide.* Arch Ophthalmol, 1972. **87**(1): p. 70-1.
28. Flugel, C., et al., *Species differences in choroidal vasodilative innervation: evidence for specific intrinsic nitrergic and VIP-positive neurons in the human eye.* Invest Ophthalmol Vis Sci, 1994. **35**(2): p. 592-9.
29. Hogan, M.J., *Ultrastructure of the choroid. Its role in the pathogenesis of chorioretinal disease.* Trans Pac Coast Otoophthalmol Soc Annu Meet, 1961. **42**: p. 61-87.
30. Chen, L., et al., *Distribution of the collagen IV isoforms in human Bruch's membrane.* Br J Ophthalmol, 2003. **87**(2): p. 212-5.
31. Pauleikhoff, D., et al., *Correlation between biochemical composition and fluorescein binding of deposits in Bruch's membrane.* Ophthalmology, 1992. **99**(10): p. 1548-53.

32. Aisenbrey, S., et al., *Retinal pigment epithelial cells synthesize laminins, including laminin 5, and adhere to them through alpha3- and alpha6-containing integrins.* Invest Ophthalmol Vis Sci, 2006. **47**(12): p. 5537-44.
33. Hewitt, A.T., K. Nakazawa, and D.A. Newsome, *Analysis of newly synthesized Bruch's membrane proteoglycans.* Invest Ophthalmol Vis Sci, 1989. **30**(3): p. 478-86.
34. Del Priore, L.V., et al., *Extracellular matrix ligands promote RPE attachment to inner Bruch's membrane.* Curr Eye Res, 2002. **25**(2): p. 79-89.
35. Del Priore, L.V. and T.H. Tezel, *Reattachment rate of human retinal pigment epithelium to layers of human Bruch's membrane.* Arch Ophthalmol, 1998. **116**(3): p. 335-41.
36. Gong, J., et al., *Effects of extracellular matrix and neighboring cells on induction of human embryonic stem cells into retinal or retinal pigment epithelial progenitors.* Exp Eye Res, 2008. **86**(6): p. 957-65.
37. Tezel, T.H., L.V. Del Priore, and H.J. Kaplan, *Reengineering of aged Bruch's membrane to enhance retinal pigment epithelium repopulation.* Invest Ophthalmol Vis Sci, 2004. **45**(9): p. 3337-48.
38. Strauss, O., *The retinal pigment epithelium in visual function.* Physiol Rev, 2005. **85**(3): p. 845-81.
39. Marshall, J., *The ageing retina: physiology or pathology.* Eye (Lond), 1987. **1 (Pt 2)**: p. 282-95.
40. Curcio, C.A., *Photoreceptor topography in ageing and age-related maculopathy.* Eye (Lond), 2001. **15**(Pt 3): p. 376-83.
41. Barron, M.J., et al., *Mitochondrial abnormalities in ageing macular photoreceptors.* Invest Ophthalmol Vis Sci, 2001. **42**(12): p. 3016-22.
42. Kim, S.Y., et al., *Morphometric analysis of the macula in eyes with disciform age-related macular degeneration.* Retina, 2002. **22**(4): p. 471-7.
43. Green, W.R. and C. Enger, *Age-related macular degeneration histopathologic studies. The 1992 Lorenz E. Zimmerman Lecture.* Ophthalmology, 1993. **100**(10): p. 1519-35.
44. Handa, J.T., et al., *Increase in the advanced glycation end product pentosidine in Bruch's membrane with age.* Invest Ophthalmol Vis Sci, 1999. **40**(3): p. 775-9.

45. Uchiki, T., et al., *Glycation-altered proteolysis as a pathobiologic mechanism that links dietary glycemic index, aging, and age-related disease (in nondiabetics).* Aging Cell, 2012. **11**(1): p. 1-13.

46. Weikel, K.A., et al., *Natural history of age-related retinal lesions that precede AMD in mice fed high or low glycemic index diets.* Invest Ophthalmol Vis Sci, 2012. **53**(2): p. 622-32.

47. Margolis, R. and R.F. Spaide, *A pilot study of enhanced depth imaging optical coherence tomography of the choroid in normal eyes.* Am J Ophthalmol, 2009. **147**(5): p. 811-5.

48. Spaide, R.F., H. Koizumi, and M.C. Pozzoni, *Enhanced depth imaging spectral-domain optical coherence tomography.* Am J Ophthalmol, 2008. **146**(4): p. 496-500.

49. Ding, X., et al., *Choroidal thickness in healthy Chinese subjects.* Invest Ophthalmol Vis Sci, 2011. **52**(13): p. 9555-60.

50. Kim, Y.G., et al., *Analysis of spectral domain optical coherence tomography findings in occult macular dystrophy.* Acta Ophthalmol, 2011. **89**(1): p. e52-6.

51. Wood, A., et al., *Retinal and choroidal thickness in early age-related macular degeneration.* Am J Ophthalmol, 2011. **152**(6): p. 1030-1038 e2.

52. Friedman, E., *A hemodynamic model of the pathogenesis of age-related macular degeneration.* Am J Ophthalmol, 1997. **124**(5): p. 677-82.

53. Friedman, E., et al., *Ocular blood flow velocity in age-related macular degeneration.* Ophthalmology, 1995. **102**(4): p. 640-6.

54. McLeod, D.S. and G.A. Lutty, *High-resolution histologic analysis of the human choroidal vasculature.* Invest Ophthalmol Vis Sci, 1994. **35**(11): p. 3799-811.

55. Apte, R.S., et al., *Macrophages inhibit neovascularization in a murine model of age-related macular degeneration.* PLoS Med, 2006. **3**(8): p. e310.

56. Izumi-Nagai, K., et al., *Interleukin-6 receptor-mediated activation of signal transducer and activator of transcription-3 (STAT3) promotes choroidal neovascularization.* Am J Pathol, 2007. **170**(6): p. 2149-58.

57. Folkman, J., *Seminars in Medicine of the Beth Israel Hospital, Boston. Clinical applications of research on angiogenesis.* N Engl J Med, 1995. **333**(26): p. 1757-63.

58. Aiello, L.P., et al., *Vascular endothelial growth factor in ocular fluid of patients with diabetic retinopathy and other retinal disorders.* N Engl J Med, 1994. **331**(22): p. 1480-7.
59. Sheridan, C.M., et al., *Expression of hypoxia-inducible factor-1alpha and -2alpha in human choroidal neovascular membranes.* Graefes Arch Clin Exp Ophthalmol, 2009. **247**(10): p. 1361-7.
60. Asahara, T., et al., *VEGF contributes to postnatal neovascularization by mobilizing bone marrow-derived endothelial progenitor cells.* EMBO J, 1999. **18**(14): p. 3964-72.
61. Guerin, E., et al., *SDF1-alpha is associated with VEGFR-2 in human choroidal neovascularisation.* Microvasc Res, 2008. **75**(3): p. 302-7.
62. Sengupta, N., et al., *Paracrine modulation of CXCR4 by IGF-1 and VEGF: implications for choroidal neovascularization.* Invest Ophthalmol Vis Sci, 2010. **51**(5): p. 2697-704.
63. Barleon, B., et al., *Migration of human monocytes in response to vascular endothelial growth factor (VEGF) is mediated via the VEGF receptor flt-1.* Blood, 1996. **87**(8): p. 3336-43.
64. Clauss, M., et al., *Vascular permeability factor: a tumor-derived polypeptide that induces endothelial cell and monocyte procoagulant activity, and promotes monocyte migration.* J Exp Med, 1990. **172**(6): p. 1535-45.
65. Grossniklaus, H.E. and W.R. Green, *Choroidal neovascularization.* Am J Ophthalmol, 2004. **137**(3): p. 496-503.
66. Steen, B., et al., *Matrix metalloproteinases and metalloproteinase inhibitors in choroidal neovascular membranes.* Invest Ophthalmol Vis Sci, 1998. **39**(11): p. 2194-200.
67. Folkman, J. and M. Klagsbrun, *Vascular physiology. A family of angiogenic peptides.* Nature, 1987. **329**(6141): p. 671-2.
68. Gao, G., et al., *Unbalanced expression of VEGF and PEDF in ischemia-induced retinal neovascularization.* FEBS Lett, 2001. **489**(2-3): p. 270-6.
69. Carmeliet, P. and R.K. Jain, *Angiogenesis in cancer and other diseases.* Nature, 2000. **407**(6801): p. 249-57.
70. Bhutto, I.A., et al., *Reduction of endogenous angiogenesis inhibitors in Bruch's membrane of the submacular region in eyes with age-related macular degeneration.* Arch Ophthalmol, 2008. **126**(5): p. 670-8.

71. Masters, S.L. and D. De Nardo, *Innate immunity.* Curr Opin Immunol, 2014. **26**: p. v-vi.
72. Kumar, H., T. Kawai, and S. Akira, *Pathogen recognition by the innate immune system.* Int Rev Immunol, 2011. **30**(1): p. 16-34.
73. Blann, A.D., *Endothelial cell activation, injury, damage and dysfunction: separate entities or mutual terms?* Blood Coagul Fibrinolysis, 2000. **11**(7): p. 623-30.
74. Sprague, A.H. and R.A. Khalil, *Inflammatory cytokines in vascular dysfunction and vascular disease.* Biochem Pharmacol, 2009. **78**(6): p. 539-52.
75. Jager, R.D., W.F. Mieler, and J.W. Miller, *Age-related macular degeneration.* N Engl J Med, 2008. **358**(24): p. 2606-17.
76. Crabb, J.W., et al., *Drusen proteome analysis: an approach to the etiology of age-related macular degeneration.* Proc Natl Acad Sci U S A, 2002. **99**(23): p. 14682-7.
77. Johnson, L.V., et al., *Complement activation and inflammatory processes in Drusen formation and age related macular degeneration.* Exp Eye Res, 2001. **73**(6): p. 887-96.
78. Johnson, L.V., et al., *A potential role for immune complex pathogenesis in drusen formation.* Exp Eye Res, 2000. **70**(4): p. 441-9.
79. Lawler, J.W., H.S. Slayter, and J.E. Coligan, *Isolation and characterization of a high molecular weight glycoprotein from human blood platelets.* J Biol Chem, 1978. **253**(23): p. 8609-16.
80. Wight, T.N., et al., *Light microscopic immunolocation of thrombospondin in human tissues.* J Histochem Cytochem, 1985. **33**(4): p. 295-302.
81. Naganuma, H., et al., *Quantification of thrombospondin-1 secretion and expression of alphavbeta3 and alpha3beta1 integrins and syndecan-1 as cell-surface receptors for thrombospondin-1 in malignant glioma cells.* J Neurooncol, 2004. **70**(3): p. 309-17.
82. Bornstein, P., *Diversity of function is inherent in matricellular proteins: an appraisal of thrombospondin 1.* J Cell Biol, 1995. **130**(3): p. 503-6.
83. Tan, K. and J. Lawler, *The interaction of Thrombospondins with extracellular matrix proteins.* J Cell Commun Signal, 2009. **3**(3-4): p. 177-87.
84. Chen, H., et al., *Binding and degradation of thrombospondin-1 mediated through heparan sulphate proteoglycans and low-density-lipoprotein receptor-related*

protein: localization of the functional activity to the trimeric N-terminal heparin-binding region of thrombospondin-1. Biochem J, 1996. **318 (Pt 3)**: p. 959-63.

85. Calzada, M.J., et al., *Recognition of the N-terminal modules of thrombospondin-1 and thrombospondin-2 by alpha6beta1 integrin.* J Biol Chem, 2003. **278**(42): p. 40679-87.
86. Uno, K., et al., *Impaired expression of thrombospondin-1 in eyes with age related macular degeneration.* Br J Ophthalmol, 2006. **90**(1): p. 48-54.
87. Sheibani, N., et al., *Thrombospondin-1, a natural inhibitor of angiogenesis, is present in vitreous and aqueous humor and is modulated by hyperglycemia.* Biochem Biophys Res Commun, 2000. **267**(1): p. 257-61.
88. Evans, J. and R. Wormald, *Is the incidence of registrable age-related macular degeneration increasing?* Br J Ophthalmol, 1996. **80**(1): p. 9-14.
89. Wu, Z., et al., *Attenuation of retinal vascular development and neovascularization in transgenic mice over-expressing thrombospondin-1 in the lens.* Dev Dyn, 2006. **235**(7): p. 1908-20.
90. Lopez-Dee, Z., K. Pidcock, and L.S. Gutierrez, *Thrombospondin-1: multiple paths to inflammation.* Mediators Inflamm, 2011. **2011**: p. 296069.
91. Becerra, S.P., et al., *Pigment epithelium-derived factor behaves like a noninhibitory serpin. Neurotrophic activity does not require the serpin reactive loop.* J Biol Chem, 1995. **270**(43): p. 25992-9.
92. Becerra, S.P., *Focus on Molecules: Pigment epithelium-derived factor (PEDF).* Exp Eye Res, 2006. **82**(5): p. 739-40.
93. He, X., et al., *PEDF and its roles in physiological and pathological conditions: implication in diabetic and hypoxia-induced angiogenic diseases.* Clin Sci (Lond), 2015. **128**(11): p. 805-23.
94. Tombran-Tink, J. and L.V. Johnson, *Neuronal differentiation of retinoblastoma cells induced by medium conditioned by human RPE cells.* Invest Ophthalmol Vis Sci, 1989. **30**(8): p. 1700-7.
95. Duh, E.J., et al., *Pigment epithelium-derived factor suppresses ischemia-induced retinal neovascularization and VEGF-induced migration and growth.* Invest Ophthalmol Vis Sci, 2002. **43**(3): p. 821-9.
96. Bouck, N., *PEDF: anti-angiogenic guardian of ocular function.* Trends Mol Med, 2002. **8**(7): p. 330-4.

97. Plunkett, B.A., et al., *Decreased expression of pigment epithelium derived factor (PEDF), an inhibitor of angiogenesis, in placentas of unexplained stillbirths.* Reprod Biol, 2008. **8**(2): p. 107-20.

98. Dawson, D.W., et al., *Pigment epithelium-derived factor: a potent inhibitor of angiogenesis.* Science, 1999. **285**(5425): p. 245-8.

99. Huang, Q., et al., *PEDF-deficient mice exhibit an enhanced rate of retinal vascular expansion and are more sensitive to hyperoxia-mediated vessel obliteration.* Exp Eye Res, 2008. **87**(3): p. 226-41.

100. Hartnett, M.E. and A. Capone, Jr., *Advances in diagnosis, clinical care, research, and treatment in retinopathy of prematurity.* Eye Brain, 2016. **8**: p. 27-29.

101. Ludwig, C.A., et al., *The Epidemiology of Retinopathy of Prematurity in the United States.* Ophthalmic Surg Lasers Imaging Retina, 2017. **48**(7): p. 553-562.

102. Mintz-Hittner, H.A., M.M. Geloneck, and A.Z. Chuang, *Clinical Management of Recurrent Retinopathy of Prematurity after Intravitreal Bevacizumab Monotherapy.* Ophthalmology, 2016. **123**(9): p. 1845-55.

103. Hu, Q., et al., *Long-Term Relief of Cerebral Radiation Necrosis Treated with Low-Dose Bevacizumab - a Report of 2 Cases.* Oncol Res Treat, 2017. **40**(3): p. 133-137.

104. Adams, G.G., et al., *Treatment trends for retinopathy of prematurity in the UK: active surveillance study of infants at risk.* BMJ Open, 2017. **7**(3): p. e013366.

105. Hartnett, M.E., *Pathophysiology and mechanisms of severe retinopathy of prematurity.* Ophthalmology, 2015. **122**(1): p. 200-10.

106. Hartnett, M.E., *Vascular endothelial growth factor antagonist therapy for retinopathy of prematurity.* Clin Perinatol, 2014. **41**(4): p. 925-43.

107. Sato, T., et al., *Serum concentrations of bevacizumab (avastin) and vascular endothelial growth factor in infants with retinopathy of prematurity.* Am J Ophthalmol, 2012. **153**(2): p. 327-333 e1.

108. Pertl, L., et al., *A Systematic Review and Meta-Analysis on the Safety of Vascular Endothelial Growth Factor (VEGF) Inhibitors for the Treatment of Retinopathy of Prematurity.* PLoS One, 2015. **10**(6): p. e0129383.

109. Gao, S., et al., *PEDF mediates pathological neovascularization by regulating macrophage recruitment and polarization in the mouse model of oxygen-induced retinopathy.* Sci Rep, 2017. **7**: p. 42846.

110. Longeras, R., et al., *A PEDF-derived peptide inhibits retinal neovascularization and blocks mobilization of bone marrow-derived endothelial progenitor cells.* Exp Diabetes Res, 2012. **2012**: p. 518426.

111. Filleur, S., et al., *Two functional epitopes of pigment epithelial-derived factor block angiogenesis and induce differentiation in prostate cancer.* Cancer Res, 2005. **65**(12): p. 5144-52.

112. Amaral, J. and S.P. Becerra, *Effects of human recombinant PEDF protein and PEDF-derived peptide 34-mer on choroidal neovascularization.* Invest Ophthalmol Vis Sci, 2010. **51**(3): p. 1318-26.

113. Penn, J.S., M.M. Henry, and B.L. Tolman, *Exposure to alternating hypoxia and hyperoxia causes severe proliferative retinopathy in the newborn rat.* Pediatr Res, 1994. **36**(6): p. 724-31.

114. Capozzi, M.E., et al., *Peroxisome proliferator-activated receptor-beta/delta regulates angiogenic cell behaviors and oxygen-induced retinopathy.* Invest Ophthalmol Vis Sci, 2013. **54**(6): p. 4197-207.

115. Bretz, C.A., et al., *NFAT isoforms play distinct roles in TNFalpha-induced retinal leukostasis.* Sci Rep, 2015. **5**: p. 14963.

116. Zhang, S.X., et al., *Pigment epithelium-derived factor (PEDF) is an endogenous antiinflammatory factor.* FASEB J, 2006. **20**(2): p. 323-5.

117. Park, K., et al., *Overexpression of pigment epithelium-derived factor inhibits retinal inflammation and neovascularization.* Am J Pathol, 2011. **178**(2): p. 688-98.

118. Barnstable, C.J. and J. Tombran-Tink, *Neuroprotective and antiangiogenic actions of PEDF in the eye: molecular targets and therapeutic potential.* Prog Retin Eye Res, 2004. **23**(5): p. 561-77.

119. Ogata, N., et al., *Pigment epithelium derived factor as a neuroprotective agent against ischemic retinal injury.* Curr Eye Res, 2001. **22**(4): p. 245-52.

120. Tombran-Tink, J. and C.J. Barnstable, *PEDF: a multifaceted neurotrophic factor.* Nat Rev Neurosci, 2003. **4**(8): p. 628-36.

121. Cayouette, M., et al., *Pigment epithelium-derived factor delays the death of photoreceptors in mouse models of inherited retinal degenerations.* Neurobiol Dis, 1999. **6**(6): p. 523-32.

122. Cao, W., et al., *Pigment epithelium-derived factor protects cultured retinal neurons against hydrogen peroxide-induced cell death.* J Neurosci Res, 1999. **57**(6): p. 789-800.

123. Curcio, C.A., et al., *Human photoreceptor topography*. J Comp Neurol, 1990. **292**(4): p. 497-523.
124. Houenou, L.J., et al., *Pigment epithelium-derived factor promotes the survival and differentiation of developing spinal motor neurons.* J Comp Neurol, 1999. **412**(3): p. 506-14.
125. Volpert, O.V., et al., *Inducer-stimulated Fas targets activated endothelium for destruction by anti-angiogenic thrombospondin-1 and pigment epithelium-derived factor*. Nat Med, 2002. **8**(4): p. 349-57.
126. Malchiodi-Albedi, F., et al., *PEDF (pigment epithelium-derived factor) promotes increase and maturation of pigment granules in pigment epithelial cells in neonatal albino rat retinal cultures.* Int J Dev Neurosci, 1998. **16**(5): p. 423-32.
127. Farnoodian, M., et al., *Expression of pigment epithelium-derived factor and thrombospondin-1 regulate proliferation and migration of retinal pigment epithelial cells.* Physiol Rep, 2015. **3**(1).
128. Sparrow, J.R. and M. Boulton, *RPE lipofuscin and its role in retinal pathobiology.* Exp Eye Res, 2005. **80**(5): p. 595-606.
129. Sparrow, J.R., D. Hicks, and C.P. Hamel, *The retinal pigment epithelium in health and disease.* Curr Mol Med, 2010. **10**(9): p. 802-23.
130. Mustafi, D., et al., *Photoreceptor phagocytosis is mediated by phosphoinositide signaling.* FASEB J, 2013. **27**(11): p. 4585-95.
131. Filleur, S., et al., *Characterization of PEDF: a multi-functional serpin family protein.* J Cell Biochem, 2009. **106**(5): p. 769-75.
132. Alberdi, E.M., J.E. Weldon, and S.P. Becerra, *Glycosaminoglycans in human retinoblastoma cells: heparan sulfate, a modulator of the pigment epithelium-derived factor-receptor interactions.* BMC Biochem, 2003. **4**: p. 1.
133. Bernard, A., et al., *Laminin receptor involvement in the anti-angiogenic activity of pigment epithelium-derived factor.* J Biol Chem, 2009. **284**(16): p. 10480-90.
134. Zhang, H., et al., *PEDF and 34-mer inhibit angiogenesis in the heart by inducing tip cells apoptosis via up-regulating PPAR-gamma to increase surface FasL.* Apoptosis, 2016. **21**(1): p. 60-8.
135. Mirochnik, Y., et al., *Short pigment epithelial-derived factor-derived peptide inhibits angiogenesis and tumor growth.* Clin Cancer Res, 2009. **15**(5): p. 1655-63.

136. Wang, X., et al., *P18 peptide, a functional fragment of pigment epithelial-derived factor, inhibits angiogenesis in hepatocellular carcinoma via modulating VEGF/VEGFR2 signalling pathway.* Oncol Rep, 2017. **38**(2): p. 755-766.

137. Matsui, T., Y. Higashimoto, and S. Yamagishi, *Laminin receptor mediates anti-inflammatory and anti-thrombogenic effects of pigment epithelium-derived factor in myeloma cells.* Biochem Biophys Res Commun, 2014. **443**(3): p. 847-51.

138. Poon, S.L., et al., *37-kDa laminin receptor precursor mediates GnRH-II-induced MMP-2 expression and invasiveness in ovarian cancer cells.* Mol Endocrinol, 2011. **25**(2): p. 327-38.

139. Song, T., et al., *Expression of 67-kDa laminin receptor was associated with tumor progression and poor prognosis in epithelial ovarian cancer.* Gynecol Oncol, 2012. **125**(2): p. 427-32.

140. Khusal, R., et al., *In vitro inhibition of angiogenesis by antibodies directed against the 37kDa/67kDa laminin receptor.* PLoS One, 2013. **8**(3): p. e58888.

141. Gong, H.Y., et al., *[Embryo-fetus development toxicity of a novel PPAR-delta agonist in rat].* Yao Xue Xue Bao, 2014. **49**(11): p. 1536-42.

142. Gong, Q., et al., *Proapoptotic PEDF functional peptides inhibit prostate tumor growth--a mechanistic study.* Biochem Pharmacol, 2014. **92**(3): p. 425-37.

143. Bishop, P.N., *Structural macromolecules and supramolecular organisation of the vitreous gel.* Prog Retin Eye Res, 2000. **19**(3): p. 323-44.

144. Bishop, P.N., et al., *Extraction and characterization of the tissue forms of collagen types II and IX from bovine vitreous.* Biochem J, 1994. **299 (Pt 2)**: p. 497-505.

145. Bishop, P., D. McLeod, and S. Ayad, *Extraction and characterisation of the intact form of bovine vitreous type IX collagen.* Biochem Biophys Res Commun, 1992. **185**(1): p. 392-7.

146. Le Goff, M.M. and P.N. Bishop, *Adult vitreous structure and postnatal changes.* Eye (Lond), 2008. **22**(10): p. 1214-22.

147. Bos, K.J., et al., *Collagen fibril organisation in mammalian vitreous by freeze etch/rotary shadowing electron microscopy.* Micron, 2001. **32**(3): p. 301-6.

148. Bishop, P.N., D. McLeod, and A. Reardon, *Effects of hyaluronan lyase, hyaluronidase, and chondroitin ABC lyase on mammalian vitreous gel.* Invest Ophthalmol Vis Sci, 1999. **40**(10): p. 2173-8.

149. EA, B., *Importance of the vitreous body in retinal surgery with special emphasis on re-operation,* in *Physiology of the vitreous body*, S. CL, Editor. 1960, C.V.Mosby Co: St. Louis. p. 29-57.
150. Teng, C.C. and H.H. Chi, *Vitreous changes and the mechanism of retinal detachment.* Am J Ophthalmol, 1957. **44**(3): p. 335-56.
151. Riordan-Eva P, W., JP, *Vaughan & Asbury's General Ophthalmology*. 17th ed. 2010, Melbourne, Australia: The MCGraw-Hill Companies, Inc.
152. Fatt, I., *Hydraulic flow conductivity of the vitreous gel.* Invest Ophthalmol Vis Sci, 1977. **16**(6): p. 565-8.
153. Arciniegas, A. and L.E. Amaya, *Bio-structural model of the human eye.* Ophthalmologica, 1980. **180**(4): p. 207-11.
154. Foulds, W.S., *Is your vitreous really necessary? The role of the vitreous in the eye with particular reference to retinal attachment, detachment and the mode of action of vitreous substitutes.* Eye (Lond), 1987. **1 (Pt 6)**: p. 641-64.
155. Jacobson, B., et al., *Inhibition of vascular endothelial cell growth and trypsin activity by vitreous.* Exp Eye Res, 1985. **41**(5): p. 581-95.
156. Aretz, S., et al., *In-depth mass spectrometric mapping of the human vitreous proteome.* Proteome Sci, 2013. **11**(1): p. 22.
157. Murthy, K.R., et al., *Proteomic analysis of human vitreous humor.* Clin Proteomics, 2014. **11**(1): p. 29.
158. Angi, M., et al., *Proteomic analyses of the vitreous humour.* Mediators Inflamm, 2012. **2012**: p. 148039.
159. Sebag, J., *The vitreous*, ed. H.J. WJ. 1992, St. Louis: Saunders.
160. Noulas, A.V., et al., *Pig vitreous gel: macromolecular composition with particular reference to hyaluronan-binding proteoglycans.* Biochimie, 2002. **84**(4): p. 295-302.
161. Necas, J.B., L.; Brauner, P.; Kolar, J., *Hyaluronic acid (hyaluronan): a review.* Veterinarni Medicine, 2008. **53**(8): p. 397-411.
162. Lapcik, L., Jr., et al., *Hyaluronan: Preparation, Structure, Properties, and Applications.* Chem Rev, 1998. **98**(8): p. 2663-2684.
163. Denlinger, J.L., G. Eisner, and E.A. Balazs, *Age-related changes in the vitreus and lens of rhesus monkeys (Macaca mulatta).* Exp Eye Res, 1980. **31**(1): p. 67-79.

164. Garcia-Abuin, A.G.-D., D.; Navaza, J. M.; Regueiro, L.; Vidal-Tato, I., *Viscosimetric behaviour of hyaluronic acid in different aqueous solutions.* Carbohydrate Polymers, 2011. **85**(3): p. 500-505.

165. Nagashima, S.M., Y.; Miyazaki, T.; Ishida, E.; Tanaka, K.; Goto, T., *Fabrication of Apatite-Hyaluronic Acid Hybrids.* Bioceramics Development and Applications, 2011. **1**: p. 1-3.

166. Brewton, R.G., D.W. Wright, and R. Mayne, *Structural and functional comparison of type IX collagen-proteoglycan from chicken cartilage and vitreous humor.* J Biol Chem, 1991. **266**(8): p. 4752-7.

167. Reardon, A., et al., *The large chondroitin sulphate proteoglycan versican in mammalian vitreous.* Matrix Biol, 1998. **17**(5): p. 325-33.

168. Theocharis, D.A., et al., *Hyaluronan and chondroitin sulfate proteoglycans in the supramolecular organization of the mammalian vitreous body.* Connect Tissue Res, 2008. **49**(3): p. 124-8.

169. Mayne, R., et al., *Isolation and characterization of the chains of type V/type XI collagen present in bovine vitreous.* J Biol Chem, 1993. **268**(13): p. 9381-6.

170. Zhidkova, N.I., S.K. Justice, and R. Mayne, *Alternative mRNA processing occurs in the variable region of the pro-alpha 1(XI) and pro-alpha 2(XI) collagen chains.* J Biol Chem, 1995. **270**(16): p. 9486-93.

171. news, C.a.E. *Sulfation Code Found In Chondroitin Sulfate*. [cited 2018; Available from: https://pubs.acs.org/cen/news/84/i33/8433sulfation.html.

172. Kroll, P., W. Wiegand, and J. Schmidt, *Vitreopapillary traction in proliferative diabetic vitreoretinopathy [ssee comments]*. Br J Ophthalmol, 1999. **83**(3): p. 261-4.

173. Balazs, E.A.F., M. T., *Age related changes in the physical and chemical structure of human vitreus*, in *Third International Congress of Eye Research*. 1978: Osaka.

174. Balazs, E.A.D., J. L., *Aging changes in the vitreus*. Aging and human visual function, ed. R.K. Sekuler, D.; Desmukes, K. 1982, New York: Alan R. Liss.

175. Breen, M., J.W. Bizzell, and H.G. Weinstein, *A galactosamine containing proteoglycan in human vitreous.* Exp Eye Res, 1977. **24**(4): p. 409-12.

176. Kamei, A. and A. Totani, *Isolation and characterization of minor glycosaminoglycans in the rabbit vitreous body*. Biochem Biophys Res Commun, 1982. **109**(3): p. 881-7.

177. Tozer, K., M.W. Johnson, and J. Sebag, *Vitreous Aging and Posterior Vitreous Detachment*, in *Vitreousin Health and Disease*, P. Bishop, Editor. 2014, Springer: New York, New York. p. 131-150.
178. Denlinger, J.L. and E.A. Balazs, *Hyaluronan and Other Carbohydrates in the Vitreus*, in *Vitreous in Health and Disease*, J. Sebag, Editor. 2014, Springer: New York, New York. p. 13-20.
179. Monnier, V.M., R.R. Kohn, and A. Cerami, *Accelerated age-related browning of human collagen in diabetes mellitus.* Proc Natl Acad Sci U S A, 1984. **81**(2): p. 583-7.
180. van Dijk, H.W., et al., *Decreased retinal ganglion cell layer thickness in patients with type 1 diabetes.* Invest Ophthalmol Vis Sci, 2010. **51**(7): p. 3660-5.
181. Sebag, J., et al., *Biochemical abnormalities in vitreous of humans with proliferative diabetic retinopathy.* Arch Ophthalmol, 1992. **110**(10): p. 1472-6.
182. Pape, L.G. and E.A. Balazs, *The use of sodium hyaluronate (Healon) in human anterior segment surgery.* Ophthalmology, 1980. **87**(7): p. 699-705.
183. Ellis, L.M. and D.J. Hicklin, *Pathways mediating resistance to vascular endothelial growth factor-targeted therapy.* Clin Cancer Res, 2008. **14**(20): p. 6371-5.
184. Tolentino, M.J., et al., *Vascular endothelial growth factor is sufficient to produce iris neovascularization and neovascular glaucoma in a nonhuman primate.* Arch Ophthalmol, 1996. **114**(8): p. 964-70.
185. Sessa, C., et al., *Biomarkers of angiogenesis for the development of antiangiogenic therapies in oncology: tools or decorations?* Nat Clin Pract Oncol, 2008. **5**(7): p. 378-91.
186. Mordenti, J., et al., *Comparisons of the intraocular tissue distribution, pharmacokinetics, and safety of 125I-labeled full-length and Fab antibodies in rhesus monkeys following intravitreal administration.* Toxicol Pathol, 1999. **27**(5): p. 536-44.
187. Collins, T., et al., *Quantifying the relationship between inhibition of VEGF receptor 2, drug-induced blood pressure elevation and hypertension.* Br J Pharmacol, 2018. **175**(4): p. 618-630.
188. Spanel-Borowski, K. and A. Mayerhofer, *Formation and regression of capillary sprouts in corpora lutea of immature superstimulated golden hamsters.* Acta Anat (Basel), 1987. **128**(3): p. 227-35.

189. Dejana, E., R. Spagnuolo, and G. Bazzoni, *Interendothelial junctions and their role in the control of angiogenesis, vascular permeability and leukocyte transmigration.* Thromb Haemost, 2001. **86**(1): p. 308-15.

190. Ferrara, N. and T. Davis-Smyth, *The biology of vascular endothelial growth factor.* Endocr Rev, 1997. **18**(1): p. 4-25.

191. Andreoli, C.M. and J.W. Miller, *Anti-vascular endothelial growth factor therapy for ocular neovascular disease.* Curr Opin Ophthalmol, 2007. **18**(6): p. 502-8.

192. Kimoto, K. and T. Kubota, *Anti-VEGF Agents for Ocular Angiogenesis and Vascular Permeability.* J Ophthalmol, 2012. **2012**: p. 852183.

193. Al-Latayfeh, M., et al., *Antiangiogenic therapy for ischemic retinopathies.* Cold Spring Harb Perspect Med, 2012. **2**(6): p. a006411.

194. Chang, J.H., et al., *Corneal neovascularization: an anti-VEGF therapy review.* Surv Ophthalmol, 2012. **57**(5): p. 415-29.

195. Ruckman, J., et al., *2'-Fluoropyrimidine RNA-based aptamers to the 165-amino acid form of vascular endothelial growth factor (VEGF165). Inhibition of receptor binding and VEGF-induced vascular permeability through interactions requiring the exon 7-encoded domain.* J Biol Chem, 1998. **273**(32): p. 20556-67.

196. Bell, C., et al., *Oligonucleotide NX1838 inhibits VEGF165-mediated cellular responses in vitro.* In Vitro Cell Dev Biol Anim, 1999. **35**(9): p. 533-42.

197. Schmidt-Erfurth, U.M., et al., *Guidance for the treatment of neovascular age-related macular degeneration.* Acta Ophthalmol Scand, 2007. **85**(5): p. 486-94.

198. Park, S.C., D. Su, and C. Tello, *Anti-VEGF therapy for the treatment of glaucoma: a focus on ranibizumab and bevacizumab.* Expert Opin Biol Ther, 2012. **12**(12): p. 1641-7.

199. Osaadon, P., et al., *A review of anti-VEGF agents for proliferative diabetic retinopathy.* Eye (Lond), 2014. **28**(5): p. 510-20.

200. Schmidt-Erfurth, U., et al., *Intravitreal aflibercept injection for neovascular age-related macular degeneration: ninety-six-week results of the VIEW studies.* Ophthalmology, 2014. **121**(1): p. 193-201.

201. Gaudreault, J., et al., *Preclinical pharmacokinetics of Ranibizumab (rhuFabV2) after a single intravitreal administration.* Invest Ophthalmol Vis Sci, 2005. **46**(2): p. 726-33.

202. Chen, Y., et al., *Selection and analysis of an optimized anti-VEGF antibody: crystal structure of an affinity-matured Fab in complex with antigen.* J Mol Biol, 1999. **293**(4): p. 865-81.

203. Ferrara, N., H.P. Gerber, and J. LeCouter, *The biology of VEGF and its receptors.* Nat Med, 2003. **9**(6): p. 669-76.

204. Moshfeghi, A.A. and C.A. Puliafito, *Pegaptanib sodium for the treatment of neovascular age-related macular degeneration.* Expert Opin Investig Drugs, 2005. **14**(5): p. 671-82.

205. Lowe, J., et al., *Ranibizumab inhibits multiple forms of biologically active vascular endothelial growth factor in vitro and in vivo.* Exp Eye Res, 2007. **85**(4): p. 425-30.

206. Bakri, S.J., et al., *Pharmacokinetics of intravitreal ranibizumab (Lucentis).* Ophthalmology, 2007. **114**(12): p. 2179-82.

207. Zayit-Soudry, S., et al., *Safety evaluation of repeated intravitreal injections of bevacizumab and ranibizumab in rabbit eyes.* Retina, 2010. **30**(4): p. 671-81.

208. Stewart, M.W., *Clinical and differential utility of VEGF inhibitors in wet age-related macular degeneration: focus on aflibercept.* Clin Ophthalmol, 2012. **6**: p. 1175-86.

209. Varey, A.H., et al., *VEGF 165 b, an antiangiogenic VEGF-A isoform, binds and inhibits bevacizumab treatment in experimental colorectal carcinoma: balance of pro- and antiangiogenic VEGF-A isoforms has implications for therapy.* Br J Cancer, 2008. **98**(8): p. 1366-79.

210. Popescu, V., et al., *Clinical use of Bevacizumab in treating refractory glaucoma.* J Med Life, 2015. **8**(1): p. 8-12.

211. Stewart, M.W., et al., *Pharmacokinetic rationale for dosing every 2 weeks versus 4 weeks with intravitreal ranibizumab, bevacizumab, and aflibercept (vascular endothelial growth factor Trap-eye).* Retina, 2012. **32**(3): p. 434-57.

212. Bakri, S.J., et al., *Pharmacokinetics of intravitreal bevacizumab (Avastin).* Ophthalmology, 2007. **114**(5): p. 855-9.

213. Cilley, J.C., et al., *Bevacizumab in the treatment of colorectal cancer.* Expert Opin Biol Ther, 2007. **7**(5): p. 739-49.

214. Pozarowska, D. and P. Pozarowski, *The era of anti-vascular endothelial growth factor (VEGF) drugs in ophthalmology, VEGF and anti-VEGF therapy.* Cent Eur J Immunol, 2016. **41**(3): p. 311-316.

215. Yu, L., X.H. Liang, and N. Ferrara, *Comparing protein VEGF inhibitors: In vitro biological studies.* Biochem Biophys Res Commun, 2011. **408**(2): p. 276-81.

216. Stewart, M.W. and P.J. Rosenfeld, *Predicted biological activity of intravitreal VEGF Trap.* Br J Ophthalmol, 2008. **92**(5): p. 667-8.

217. Stewart, W.S., *What are the half-live of ranibizumab and aflibercept (VEGF Trap-eye) in human eyes? Calculations with a mathematical model.* Eye Reports, 2011. **1**(e5): p. 12-14.

218. Nowak, W., et al., *System and measurement method for binocular pupillometry to study pupil size variability.* Biomed Eng Online, 2014. **13**: p. 69.

219. Rofagha, S., et al., *Seven-year outcomes in ranibizumab-treated patients in ANCHOR, MARINA, and HORIZON: a multicenter cohort study (SEVEN-UP).* Ophthalmology, 2013. **120**(11): p. 2292-9.

220. Bergers, G. and D. Hanahan, *Modes of resistance to anti-angiogenic therapy.* Nat Rev Cancer, 2008. **8**(8): p. 592-603.

221. Spaide, R.F. and Y.L. Fisher, *Intravitreal bevacizumab (Avastin) treatment of proliferative diabetic retinopathy complicated by vitreous hemorrhage.* Retina, 2006. **26**(3): p. 275-8.

222. Simo, R. and C. Hernandez, *Intravitreous anti-VEGF for diabetic retinopathy: hopes and fears for a new therapeutic strategy.* Diabetologia, 2008. **51**(9): p. 1574-80.

223. Armstrong, L.C. and P. Bornstein, *Thrombospondins 1 and 2 function as inhibitors of angiogenesis.* Matrix Biol, 2003. **22**(1): p. 63-71.

224. Wang, S., C.M. Sorenson, and N. Sheibani, *Lack of thrombospondin 1 and exacerbation of choroidal neovascularization.* Arch Ophthalmol, 2012. **130**(5): p. 615-20.

225. Zhang, X. and J. Lawler, *Thrombospondin-based antiangiogenic therapy.* Microvasc Res, 2007. **74**(2-3): p. 90-9.

226. Wang, S., et al., *Suppression of thrombospondin-1 expression during uveal melanoma progression and its potential therapeutic utility.* Arch Ophthalmol, 2012. **130**(3): p. 336-41.

227. Haviv, F., et al., *Thrombospondin-1 mimetic peptide inhibitors of angiogenesis and tumor growth: design, synthesis, and optimization of pharmacokinetics and biological activities.* J Med Chem, 2005. **48**(8): p. 2838-46.

228. Gologorsky, D., A. Thanos, and D. Vavvas, *Therapeutic interventions against inflammatory and angiogenic mediators in proliferative diabetic retinopathy.* Mediators Inflamm, 2012. **2012**: p. 629452.

229. Hoekstra, R., et al., *Phase I study of the thrombospondin-1-mimetic angiogenesis inhibitor ABT-510 with 5-fluorouracil and leucovorin: a safe combination.* Eur J Cancer, 2006. **42**(4): p. 467-72.

230. Garside, S.A., et al., *A thrombospondin-mimetic peptide, ABT-898, suppresses angiogenesis and promotes follicular atresia in pre- and early-antral follicles in vivo.* Endocrinology, 2010. **151**(12): p. 5905-15.

231. Bouck, N.P., D.W. Dawson, and P.R. Gillis, *Methods and compositions for inhibiting angiogenesis*, N. University, Editor. 2001: USA.

232. Ho, T.C., et al., *PEDF induces p53-mediated apoptosis through PPAR gamma signaling in human umbilical vein endothelial cells.* Cardiovasc Res, 2007. **76**(2): p. 213-23.

233. Kadoya, M., et al., *Pigment epithelium-derived factor inhibits the growth of human esophageal squamous cell carcinoma by suppressing neovascularization.* Hokkaido Igaku Zasshi, 2015. **90**(1): p. 17-29.

234. Yang, H. and H.E. Grossniklaus, *Constitutive overexpression of pigment epithelium-derived factor inhibition of ocular melanoma growth and metastasis.* Invest Ophthalmol Vis Sci, 2010. **51**(1): p. 28-34.

235. Stellmach, V., et al., *Prevention of ischemia-induced retinopathy by the natural ocular antiangiogenic agent pigment epithelium-derived factor.* Proc Natl Acad Sci U S A, 2001. **98**(5): p. 2593-7.

236. Mori, K., et al., *Regression of ocular neovascularization in response to increased expression of pigment epithelium-derived factor.* Invest Ophthalmol Vis Sci, 2002. **43**(7): p. 2428-34.

237. Henkin, J., et al., *Modified pigment epithelium-derived factor (PEDF) peptides and uses thereof for treating neovascular diseases, inflammatory diseases, cancer, and for cytoprotection*, N. University, Editor. 2017, Northwestern University: USA.

238. Rautio, J., et al., *Prodrugs: design and clinical applications.* Nat Rev Drug Discov, 2008. **7**(3): p. 255-70.

239. Huttunen, K.M., H. Raunio, and J. Rautio, *Prodrugs--from serendipity to rational design.* Pharmacol Rev, 2011. **63**(3): p. 750-71.

240. Notari, R.E., *Prodrug design.* Pharmacol Ther, 1981. **14**(1): p. 25-53.

241. Sinkula, A.A. and S.H. Yalkowsky, *Rationale for design of biologically reversible drug derivatives: prodrugs.* J Pharm Sci, 1975. **64**(2): p. 181-210.

242. Stella, V.J., W.N. Charman, and V.H. Naringrekar, *Prodrugs. Do they have advantages in clinical practice?* Drugs, 1985. **29**(5): p. 455-73.

243. Hamad, M.O., et al., *Synthesis and hydrolytic behavior of two novel tripartate codrugs of naltrexone and 6beta-naltrexol with hydroxybupropion as potential alcohol abuse and smoking cessation agents.* Bioorg Med Chem, 2006. **14**(20): p. 7051-61.

244. Leppanen, J., et al., *Design and synthesis of a novel L-dopa-entacapone codrug.* J Med Chem, 2002. **45**(6): p. 1379-82.

245. Bodor, N. and P. Buchwald, *Drug targeting via retrometabolic approaches.* Pharmacol Ther, 1997. **76**(1-3): p. 1-27.

246. Bodor, N. and P. Buchwald, *Soft drug design: general principles and recent applications.* Med Res Rev, 2000. **20**(1): p. 58-101.

247. Stella, V.J., *Prodrugs as therapeutics.* Expert Opinion on Therapeutic Patents, 2004. **14**(3): p. 277-280.

248. Majumdar, S. and K.B. Sloan, *Synthesis, hydrolyses and dermal delivery of N-alkyl-N-alkyloxycarbonylaminomethyl (NANAOCAM) derivatives of phenol, imide and thiol containing drugs.* Bioorg Med Chem Lett, 2006. **16**(13): p. 3590-4.

249. Peyrottes, S., et al., *SATE pronucleotide approaches: an overview.* Mini Rev Med Chem, 2004. **4**(4): p. 395-408.

250. Fozard, J.R., *BP-294 Ste Civile Bioprojet.* Curr Opin Investig Drugs, 2000. **1**(1): p. 86-9.

251. Rouleau, A., et al., *Bioavailability, antinociceptive and antiinflammatory properties of BP 2-94, a histamine H3 receptor agonist prodrug.* J Pharmacol Exp Ther, 1997. **281**(3): p. 1085-94.

252. Simplicio, A.L., J.M. Clancy, and J.F. Gilmer, *Beta-aminoketones as prodrugs with pH-controlled activation.* Int J Pharm, 2007. **336**(2): p. 208-14.

253. Ettmayer, P., et al., *Lessons learned from marketed and investigational prodrugs.* J Med Chem, 2004. **47**(10): p. 2393-404.

254. Beaumont, K., et al., *Design of ester prodrugs to enhance oral absorption of poorly permeable compounds: challenges to the discovery scientist.* Curr Drug Metab, 2003. **4**(6): p. 461-85.

255. Liederer, B.M. and R.T. Borchardt, *Enzymes involved in the bioconversion of ester-based prodrugs.* J Pharm Sci, 2006. **95**(6): p. 1177-95.

256. Ehrnebo, M., S.O. Nilsson, and L.O. Boreus, *Pharmacokinetics of ampicillin and its prodrugs bacampicillin and pivampicillin in man.* J Pharmacokinet Biopharm, 1979. **7**(5): p. 429-51.

257. Jusko, W.J. and G.P. Lewis, *Comparison of ampicillin and hetacillin pharmacokinetics in man.* J Pharm Sci, 1973. **62**(1): p. 69-76.

258. Potter, P.M. and R.M. Wadkins, *Carboxylesterases--detoxifying enzymes and targets for drug therapy.* Curr Med Chem, 2006. **13**(9): p. 1045-54.

259. Persson, G., O. Pahlm, and Y. Gnosspelius, *Oral bambuterol versus terbutaline in patients with asthma.* Current therapeutic research, 1995. **56**(5): p. 457-465.

260. Ghate, D. and H.F. Edelhauser, *Ocular drug delivery.* Expert Opin Drug Deliv, 2006. **3**(2): p. 275-87.

261. Kim, S.H., et al., *Transport barriers in transscleral drug delivery for retinal diseases.* Ophthalmic Res, 2007. **39**(5): p. 244-54.

262. Shah, S.S., et al., *Drug delivery to the posterior segment of the eye for pharmacologic therapy.* Expert Rev Ophthalmol, 2010. **5**(1): p. 75-93.

263. Dias, C.S., B.S. Anand, and A.K. Mitra, *Effect of mono- and di-acylation on the ocular disposition of ganciclovir: physicochemical properties, ocular bioreversion, and antiviral activity of short chain ester prodrugs.* J Pharm Sci, 2002. **91**(3): p. 660-8.

264. van Deemter, M., et al., *Trypsin-mediated enzymatic degradation of type II collagen in the human vitreous.* Mol Vis, 2013. **19**: p. 1591-9.

265. Ghate, D. and H.F. Edelhauser, *Barriers to glaucoma drug delivery.* J Glaucoma, 2008. **17**(2): p. 147-56.

266. Urtti, A., *Challenges and obstacles of ocular pharmacokinetics and drug delivery.* Adv Drug Deliv Rev, 2006. **58**(11): p. 1131-5.

267. Hussain, A. and J.E. Truelove, *Prodrug approaches to enhancement of physicochemical properties of drugs IV: novel epinephrine prodrug.* J Pharm Sci, 1976. **65**(10): p. 1510-2.

268. Anderson, J.A., *Systemic absorption of topical ocularly applied epinephrine and dipivefrin.* Arch Ophthalmol, 1980. **98**(2): p. 350-3.

269. Mandell, A.I., F. Stentz, and A.E. Kitabchi, *Dipivalyl epinephrine: a new pro-drug in the treatment of glaucoma.* Ophthalmology, 1978. **85**(3): p. 268-75.

270. Wei, C.P., J.A. Anderson, and I. Leopold, *Ocular absorption and metabolism of topically applied epinephrine and a dipivalyl ester of epinephrine.* Invest Ophthalmol Vis Sci, 1978. **17**(4): p. 315-21.

271. Kaback, M.B., et al., *The effects of dipivalyl epinephrine on the eye.* Am J Ophthalmol, 1976. **81**(6): p. 768-72.

272. Kohn, A.N., et al., *Clinical comparison of dipivalyl epinephrine and epinephrine in the treatment of glaucoma.* Am J Ophthalmol, 1979. **87**(2): p. 196-201.

273. Yasukawa, T., et al., *Intraocular sustained drug delivery using implantable polymeric devices.* Adv Drug Deliv Rev, 2005. **57**(14): p. 2033-46.

274. Del Amo, E.M. and A. Urtti, *Current and future ophthalmic drug delivery systems. A shift to the posterior segment.* Drug Discov Today, 2008. **13**(3-4): p. 135-43.

275. Musch, D.C., et al., *Treatment of cytomegalovirus retinitis with a sustained-release ganciclovir implant. The Ganciclovir Implant Study Group.* N Engl J Med, 1997. **337**(2): p. 83-90.

276. Jaffe, G.J., et al., *Long-term follow-up results of a pilot trial of a fluocinolone acetonide implant to treat posterior uveitis.* Ophthalmology, 2005. **112**(7): p. 1192-8.

277. Del Amo, E.M. and A. Urtti, *Rabbit as an animal model for intravitreal pharmacokinetics: Clinical predictability and quality of the published data.* Exp Eye Res, 2015. **137**: p. 111-24.

278. Kidron, H., et al., *Prediction of the vitreal half-life of small molecular drug-like compounds.* Pharm Res, 2012. **29**(12): p. 3302-11.

279. Bochot, A., et al., *Intravitreal delivery of oligonucleotides by sterically stabilized liposomes.* Invest Ophthalmol Vis Sci, 2002. **43**(1): p. 253-9.

280. Sun, J., et al., *Sustained Release of Brimonidine from a New Composite Drug Delivery System for Treatment of Glaucoma.* ACS Appl Mater Interfaces, 2017. **9**(9): p. 7990-7999.

281. Li, F., et al., *Controlled release of bevacizumab through nanospheres for extended treatment of age-related macular degeneration.* Open Ophthalmol J, 2012. **6**: p. 54-8.

282. Giordano, G.G., et al., *Biodegradation and tissue reaction to intravitreous biodegradable poly(D,L-lactic-co-glycolic)acid microspheres.* Curr Eye Res, 1995. **14**(9): p. 761-8.

283. Thackaberry, E.A., et al., *Evaluation of the Toxicity of Intravitreally Injected PLGA Microspheres and Rods in Monkeys and Rabbits: Effects of Depot Size on Inflammatory Response.* Invest Ophthalmol Vis Sci, 2017. **58**(10): p. 4274-4285.

284. Allen, T.M. and P.R. Cullis, *Drug delivery systems: entering the mainstream.* Science, 2004. **303**(5665): p. 1818-22.

285. Oku, N., *Anticancer therapy using glucuronate modified long-circulating liposomes.* Adv Drug Deliv Rev, 1999. **40**(1-2): p. 63-73.

286. Sapra, P., P. Tyagi, and T.M. Allen, *Ligand-targeted liposomes for cancer treatment.* Curr Drug Deliv, 2005. **2**(4): p. 369-81.

287. van Rooijen, N. and R. van Nieuwmegen, *Liposomes in immunology: multilamellar phosphatidylcholine liposomes as a simple, biodegradable and harmless adjuvant without any immunogenic activity of its own.* Immunol Commun, 1980. **9**(3): p. 243-56.

288. Lopez-Berestein, G., et al., *Effects of sterols on the therapeutic efficacy of liposomal amphotericin B in murine candidiasis.* Cancer Drug Deliv, 1983. **1**(1): p. 37-42.

289. Diaz-Llopis, M., et al., *Liposomally-entrapped ganciclovir for the treatment of cytomegalovirus retinitis in AIDS patients. Eperimental toxicity and pharmacokinetics, and clinical trial.* Doc Ophthalmol, 1992. **82**(4): p. 297-305.

290. Akula, S.K., et al., *Treatment of cytomegalovirus retinitis with intravitreal injection of liposome encapsulated ganciclovir in a patient with AIDS.* Br J Ophthalmol, 1994. **78**(9): p. 677-80.

291. Fishman, P.H., G.A. Peyman, and T. Lesar, *Intravitreal liposome-encapsulated gentamicin in a rabbit model. Prolonged therapeutic levels.* Invest Ophthalmol Vis Sci, 1986. **27**(7): p. 1103-6.

292. Abrishami, M., et al., *Preparation, characterization, and in vivo evaluation of nanoliposomes-encapsulated bevacizumab (avastin) for intravitreal administration.* Retina, 2009. **29**(5): p. 699-703.

293. Honda, M., et al., *Liposomes and nanotechnology in drug development: focus on ocular targets.* Int J Nanomedicine, 2013. **8**: p. 495-503.

294. Thrimawithana, T.R., et al., *Drug delivery to the posterior segment of the eye.* Drug Discov Today, 2011. **16**(5-6): p. 270-7.

295. Moritera, T., et al., *Microspheres of biodegradable polymers as a drug-delivery system in the vitreous.* Invest Ophthalmol Vis Sci, 1991. **32**(6): p. 1785-90.

296. MacCumber, M.W., et al., *Suture loop to aid in ganciclovir implant removal.* Arch Ophthalmol, 1999. **117**(9): p. 1250-4.

297. Haller, J.A., et al., *Randomized, sham-controlled trial of dexamethasone intravitreal implant in patients with macular edema due to retinal vein occlusion.* Ophthalmology, 2010. **117**(6): p. 1134-1146 e3.

298. Kimura, H., et al., *In vitro phagocytosis of polylactide microspheres by retinal pigment epithelial cells and intracellular drug release.* Curr Eye Res, 1994. **13**(5): p. 353-60.

299. Bourges, J.L., et al., *Ocular drug delivery targeting the retina and retinal pigment epithelium using polylactide nanoparticles.* Invest Ophthalmol Vis Sci, 2003. **44**(8): p. 3562-9.

300. Sakurai, E., et al., *Effect of particle size of polymeric nanospheres on intravitreal kinetics.* Ophthalmic Res, 2001. **33**(1): p. 31-6.

301. Ansari, M.J., K. Kohli, and N. Dixit, *Microemulsions as potential drug delivery systems: a review.* PDA J Pharm Sci Technol, 2008. **62**(1): p. 66-79.

302. Vandamme, T.F., *Microemulsions as ocular drug delivery systems: recent developments and future challenges.* Prog Retin Eye Res, 2002. **21**(1): p. 15-34.

303. Fialho, S.L. and A. da Silva-Cunha, *New vehicle based on a microemulsion for topical ocular administration of dexamethasone.* Clin Exp Ophthalmol, 2004. **32**(6): p. 626-32.

304. Quintana, A., et al., *Design and function of a dendrimer-based therapeutic nanodevice targeted to tumor cells through the folate receptor.* Pharm Res, 2002. **19**(9): p. 1310-6.

305. Cheng, Y., et al., *Dendrimers as drug carriers: applications in different routes of drug administration.* J Pharm Sci, 2008. **97**(1): p. 123-43.

306. Kambhampati, S.P. and R.M. Kannan, *Dendrimer nanoparticles for ocular drug delivery.* J Ocul Pharmacol Ther, 2013. **29**(2): p. 151-65.

307. Shmueli, R.B., et al., *Long-term suppression of ocular neovascularization by intraocular injection of biodegradable polymeric particles containing a serpin-derived peptide.* Biomaterials, 2013. **34**(30): p. 7544-51.

308. Schwartz, S.G., et al., *Drug delivery techniques for treating age-related macular degeneration.* Expert Opin Drug Deliv, 2014. **11**(1): p. 61-8.

309. Peeters, L., et al., *Vitreous: a barrier to nonviral ocular gene therapy.* Invest Ophthalmol Vis Sci, 2005. **46**(10): p. 3553-61.

310. Kim, H., S.B. Robinson, and K.G. Csaky, *Investigating the movement of intravitreal human serum albumin nanoparticles in the vitreous and retina.* Pharm Res, 2009. **26**(2): p. 329-37.

311. Kim, N., et al., *Synthesis and characterization of mannosylated pegylated polyethylenimine as a carrier for siRNA.* Int J Pharm, 2012. **427**(1): p. 123-33.

312. Zern, B.J., et al., *A Biocompatible Arginine-based Polycation.* Adv Funct Mater, 2011. **21**(3): p. 434-440.

313. Veiseh, O., et al., *In vivo safety evaluation of polyarginine coated magnetic nanovectors.* Mol Pharm, 2013. **10**(11): p. 4099-106.

314. Sarker, S.R., et al., *Arginine-based cationic liposomes for efficient in vitro plasmid DNA delivery with low cytotoxicity.* Int J Nanomedicine, 2013. **8**: p. 1361-75.

315. Liu, X., et al., *Promoting siRNA delivery via enhanced cellular uptake using an arginine-decorated amphiphilic dendrimer.* Nanoscale, 2015. **7**(9): p. 3867-75.

316. Li, H., et al., *Sustaining Intravitreal Residence With L-Arginine Peptide-Conjugated Nanocarriers.* Invest Ophthalmol Vis Sci, 2017. **58**(12): p. 5142-5150.

317. Ramirez, J.C., M. Sanchez-Chaves, and F. Arranz, *Dextran functionalized by 4-nitrophenyl carbonate groups. Aminolysis reactions.* Die Angewandte Makromolekulare Chemie, 1995. **225**: p. 123-130.

318. Vanndoorne, F., et al., *Re-investigation of the 4-nitrophenyl chloroformate activation of dextran. Evidence for the formation of different types of carbonate moieties.* Makromol Chem, 1985. **186**: p. 2455-2460.

319. Sam, D.J. and H.E. Simmons, *Crown ether chemistry. Substitution reactions of potassium halide and potassium hydroxide complexes of dicyclohexyl-18-crown-6.* Journal of the American Chemistry Society, 1974. **96**(7): p. 2252-2253.

320. Hatano, M. and K. Ishihara, *Lanthanum(III) catalysts for highly efficient and chemoselective transesterification.* Chem Commun (Camb), 2013. **49**(20): p. 1983-97.

321. Hilal, S.H., *Estimation of Hydrolysis Rate Constants of Carboxylic Acid Ester and Phosphate Ester Compounds in Aqueous Systems from Molecular Structure by*

SPARC. 2006, U.S. Environmental Protection Agency Office of Research and Development Washington, DC 20460.

322. Nourinia, R., et al., *Ocular Safety of Intravitreal Propranolol and Its Efficacy in Attenuation of Choroidal Neovascularization.* Invest Ophthalmol Vis Sci, 2015. **56**(13): p. 8228-35.
323. Yano, H., et al., *Hydrolysis behavior of prednisolone 21-hemisuccinate/beta-cyclodextrin amide conjugate: involvement of intramolecular catalysis of amide group in drug release.* Chem Pharm Bull (Tokyo), 2000. **48**(8): p. 1125-8.
324. Lance, K.D., et al., *In Vitro and In Vivo Sustained Zero-Order Delivery of Rapamycin (Sirolimus) From a Biodegradable Intraocular Device.* Invest Ophthalmol Vis Sci, 2015. **56**(12): p. 7331-7.
325. Al-Zamil, W.M. and S.A. Yassin, *Recent developments in age-related macular degeneration: a review.* Clin Interv Aging, 2017. **12**: p. 1313-1330.
326. Adamis, A.P., et al., *Increased vascular endothelial growth factor levels in the vitreous of eyes with proliferative diabetic retinopathy.* Am J Ophthalmol, 1994. **118**(4): p. 445-50.
327. Bodh, S.A., et al., *Inflammatory glaucoma.* Oman J Ophthalmol, 2011. **4**(1): p. 3-9.
328. Adamson, P., et al., *Single ocular injection of a sustained-release anti-VEGF delivers 6months pharmacokinetics and efficacy in a primate laser CNV model.* J Control Release, 2016. **244**(Pt A): p. 1-13.
329. Bantseev, V., et al., *Determination of a No-Observable Effect Level for Endotoxin Following a Single Intravitreal Administration to Dutch Belted Rabbits.* Invest Ophthalmol Vis Sci, 2017. **58**(3): p. 1545-1552.
330. Magalhaes, P.O., et al., *Methods of endotoxin removal from biological preparations: a review.* J Pharm Pharm Sci, 2007. **10**(3): p. 388-404.
331. Kompella, U.B., et al., *Nanomedicines for back of the eye drug delivery, gene delivery, and imaging.* Prog Retin Eye Res, 2013. **36**: p. 172-98.
332. Wang, Y., A. Rajala, and R.V. Rajala, *Lipid Nanoparticles for Ocular Gene Delivery.* J Funct Biomater, 2015. **6**(2): p. 379-94.
333. Park, D., et al., *An anti-angiogenic reverse thermal gel as a drug-delivery system for age-related wet macular degeneration.* Macromol Biosci, 2013. **13**(4): p. 464-9.

334. Jones, C.I., et al., *The antithrombotic effect of dextran-40 in man is due to enhanced fibrinolysis in vivo.* J Vasc Surg, 2008. **48**(3): p. 715-22.

335. Howard, J.M., et al., *The present status of dextran as a plasma expander.* Am J Surg, 1959. **97**(5): p. 593-6.

336. Rosenblum, W.I., *Effects of dextran-40 on blood viscosity in experimental macroglobulinaemia.* Nature, 1968. **218**(5141): p. 591-3.

337. Administration, U.F.a.D., *Ophthalmic drug products for over-the-counter human use*, U.F.a.D. Administration, Editor. 2017. p. 1.

338. Yang, J., et al., *The biocompatibility of fatty acid modified dextran-agmatine bioconjugate gene delivery vector.* Biomaterials, 2012. **33**(2): p. 604-13.

339. Liu, C.G., et al., *Linolenic acid-modified chitosan for formation of self-assembled nanoparticles.* J Agric Food Chem, 2005. **53**(2): p. 437-41.

340. Senanayake, T.H., G. Warren, and S.V. Vinogradov, *Novel anticancer polymeric conjugates of activated nucleoside analogues.* Bioconjug Chem, 2011. **22**(10): p. 1983-93.

341. Ghosh, J.G., et al., *Long-acting protein drugs for the treatment of ocular diseases.* Nat Commun, 2017. **8**: p. 14837.

342. Coulson-Thomas, V.J., et al., *Tumor Necrosis Factor-stimulated Gene-6 (TSG-6) Is Constitutively Expressed in Adult Central Nervous System (CNS) and Associated with Astrocyte-mediated Glial Scar Formation following Spinal Cord Injury.* J Biol Chem, 2016. **291**(38): p. 19939-52.

343. Bosshart, H., Heinzelmann, M., *Arginine-Rich Cationic Polypeptides Amplify*

Lipopolysaccharide-Induced Monocyte Activation. INFECTION AND IMMUNITY, 2002. **70**(12): p. 6904-6910.

344. Bonilha, V.L., et al., *Retinal deimination and PAD2 levels in retinas from donors with age-related macular degeneration (AMD).* Exp Eye Res, 2013. **111**: p. 71-8.

345. Bhattacharya, S.K., *Retinal deimination in aging and disease.* IUBMB Life, 2009. **61**(5): p. 504-9.

346. Algeciras, M.E., H. Takahara, and S.K. Bhattacharya, *Mechanical stretching elevates peptidyl arginine deiminase 2 expression in astrocytes.* Curr Eye Res, 2008. **33**(11): p. 994-1001.

347. Bagneris, C., et al., *Crystal structures of alpha-crystallin domain dimers of alphaB-crystallin and Hsp20.* J Mol Biol, 2009. **392**(5): p. 1242-52.

348. Engstrom, K.M., et al., *The Stability of N,N-Carbonyldiimidazole Toward Atmospheric Moisture.* Organic Process Research & Development, 2014. **18**(4): p. 488-494.

349. Bakhoj, A. and N.H. Heegaard, *Monitoring nitrotyrosinylation of a synthetic peptide by capillary zone electrophoresis.* Electrophoresis, 1999. **20**(12): p. 2519-23.

350. Los, L.I., *The rabbit as an animal model for post-natal vitreous matrix differentiation and degeneration.* Eye (Lond), 2008. **22**(10): p. 1223-32.

351. Lopez-Arbeloa, I., *Molecular forms of rhodamine B.* Chemical physics letters, 1981. **79**(2): p. 347-350.

352. Segura-Ibarra, V., et al., *Nanoparticles administered intrapericardially enhance payload myocardial distribution and retention.* J Control Release, 2017. **262**: p. 18-27.

353. Rudnick-Glick, S., et al., *Near IR fluorescent conjugated poly(ethylene glycol)bisphosphonate nanoparticles for in vivo bone targeting in a young mouse model.* J Nanobiotechnology, 2015. **13**: p. 80.

354. Bundgaard, H.B., A.; Chang, S.; Lee, V. H. L., *Prodrugs of timolol for improved ocular delivery: synthesis, hydrolysis kinetics and lipophilicity of various timolol esters.* International Journal of Pharmaceutics, 1986. **33**(1-3): p. 15-26.

355. Sam, D.J.S., H. E., *Crown ether chemistry. Substitution reactions of potassium halide and potassium hydroxide complexes of dicyclohexyl-18-crown-6.* Journal of the American Chemical Society, 1974. **96**(7): p. 2252–2253.

356. Singh, R., et al., *Transesterification/Acylation of secondary alcohols mediated by N-heterocyclic carbene catalysts.* J Org Chem, 2004. **69**(1): p. 209-12.

357. Tanaka, K., et al., *Rhodium-catalyzed asymmetric one-pot transesterification and [2 + 2 + 2] cycloaddition leading to enantioenriched 3,3-disubstituted phthalides.* Org Lett, 2007. **9**(7): p. 1307-10.

358. Pericas, À., A. Shafir, and A. Vallribera, *Zinc(II) oxide: an efficient catalyst for selective transesterification of β-ketoesters.* Tetrahedron, 2008. **64**(39): p. 9258-9263.

359. Stanton, M.G. and M.R. Gagné, *A Mild Protocol for the Conversion of Simple Esters to tert-Butyl Esters.* The Journal of Organic Chemistry, 1997. **62**(23): p. 8240-8242.

360. Kleinpeter, E., F. Taddei, and P. Wacker, *Electronic and Steric Substituent Influences on the Conformational Equilibria of Cyclohexyl Esters: The Anomeric Effect Is Not Anomalous!* Chemistry – A European Journal, 2003. **9**(6): p. 1360-1368.

361. Mainolfi, N., et al., *An Effective Prodrug Strategy to Selectively Enhance Ocular Exposure of a Cannabinoid Receptor (CB1/2) Agonist.* Journal of Medicinal Chemistry, 2013. **56**(13): p. 5464-5472.

362. Ashworth, I.W., B.G. Cox, and B. Meyrick, *Kinetics and mechanism of N-Boc cleavage: evidence of a second-order dependence upon acid concentration.* J Org Chem, 2010. **75**(23): p. 8117-25.

363. Yano, H., et al., *Preparation of prednisolone-appended alpha-, beta- and gamma-cyclodextrins: substitution at secondary hydroxyl groups and in vitro hydrolysis behavior.* J Pharm Sci, 2001. **90**(4): p. 493-503.

364. Liu, C., et al., *Arginine-terminated generation 4 PAMAM dendrimer as an effective nanovector for functional siRNA delivery in vitro and in vivo.* Bioconjug Chem, 2014. **25**(3): p. 521-32.

Supplement

S.1 Boc-N-R-O-ahx-DNP compounds

S.1.1 *Synthesis of intermediates and final products*

Synthesis of Methyl 5-oxo-5-[(*tert*-butoxycarbonylmethyl)amino]valerate (1). Amide of sarcosine-t-butyl ester with glutaric acid monomethyl ester.

0.1 mEq of sarcosine *tert*-butyl ester hydrochloride was dissolved in DCM with 0.2 mEq of TEA under stirring at RT. Then 0.1 mEq of glutaric acid monomethyl ester chloride was dissolved in DCM and this solution was added dropwise on the first solution. After 30 min the reaction was complete. It was followed by TLC (DCM:MeOH; 9:1). The crude product was purified by ColCh with a mixture of DCM:MeOH. Final product: meO-glt-Sar-O-tbut.

Synthesis of Potassium 5-Oxo-5-(tert-butoxycarbonylamino)valerate (2). Potassium salt of glutaric acid half amide with sarcosine-t-butyl ester.

0.1 mEq of cmpd 1 was dissolved in a mixture of MeOH:water, 9:1. To this solution, 0.1 mEq of KOH was added. The reaction was stirred at RT. After 1 h the reaction was complete. It was followed (Boc UV absorbance) by TLC (DCM:MeOH; 9:1). The solution was dried under vacuum, product in water was extracted in a separation funnel (ether/water), and aqueous phase freeze-dried to give the potassium salt. Final product: KO-glt-Sar-O-tbut.

Synthesis of Methyl 6-oxo-6-[(*tert*-butoxycarbonylmethyl)amino]hexanoate (3). Amide of sarcosine-t-butyl ester with adipic acid monomethyl ester.

0.1 mEq of glycine *tert*-butyl ester hydrochloride was dissolved in DCM with 0.2 mEq of TEA under stirring at RT. Then 0.1 mEq of methyl adipoyl acid monomethyl ester chloride was dissolved in DCM and this solution was added dropwise to the first solution. After 30 min the reaction was done. It was followed by TLC (DCM:MeOH; 9:1). The crude product methyl ester was purified by ColCh with a mixture of DCM:MeOH. Final product: meO-adp-Gly-O-tbut.

Synthesis of Potassium 6-Oxo-6-(tert-butoxycarbonylamino)hexanoate (4). Potassium salt of adipic acid half amide with sarcosine-t-butyl ester.

0.1 mEq of cmpd 3 was dissolved in a mixture of MeOH:water 9:1. To this solution, 0.1 mEq of KOH was added. The reaction was stirred at RT. After 1 h the reaction was complete. It was followed (Boc UV absorbance) by TLC (DCM:MeOH; 9:1). The solution was dried under vacuum, product in water was extracted in a separation funnel (ether/water), and aqueous phase freeze-dried to give the potassium salt. Final product: KO-adp-Gly-O-tbut.

Synthesis of *Tert*-butyl {2-[(4-hydroxypentanoyl)amino]ethyl}carbamate (8). 3-hydroxypentanoic acid amide with mono-Boc-ethylenediamine (a secondary alcohol to which a chromophoric acid can later be attached).

To synthesize a secondary amino alcohol, we have followed the method described by Chalid et al (2011) with some modifications. 0.1 mEq of *N*-Boc-ethylenediamine was dissolved in 5 mL of methanol in a round bottom flask. Then 0.1 mEq of γ-Valerolactone (Figure S-1) was added to the reaction. The reaction was stirred at RT, and followed by TLC (DCM:MeOH; 9:1). After 16 h the reaction was complete. The mixture was dried under vacuum and purify it by CC (DCM:MeOH). Final produc: Boc-NetN-val-secOH.

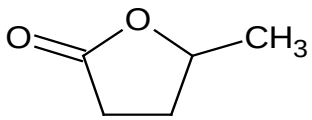

Figure S-1. Chemical structure of γ-Valerolactone.

There were three compounds (below) for which we used the above alternative synthetic route to attach chromophoric carboxamides to aid in kinetic monitoring of ester hydrolysis, by HPLC.

For example, cmpd 12 is a chromophoric sarcosine amide which can be amide bound to adipic or glutaric esters (left side) of *N*-blocked amino alcohols to enable facile observation of chromophore detachment following ester hydrolysis (Figure S-11).

The synthesis pathway to achieve the chromophore-sarcosine compound (12) are the following:

Synthesis of *Tert* butyl (2-[[(3-nitrophenyl)carbonyl]amino]ethyl)*c*arbamate (9). Amide between 3-nitrobenzoic acid and mono-Boc-ethylenediamine.

0.1 mEq of *N*-Boc-ethylenediamine was dissolved in DCM with 0.1 mEq of TEA under stirring at RT. Then 0.1 mEq of 3-Nitrobenzoyl chloride was dissolved in DCM and this solution was added dropwise on the first solution. After 30 min the reaction was complete. It was followed (nitrophenyl UV absorbance) by TLC (DCM:MeOH; 9:1). The crude product was purified by ColCh with a mixture of DCM:MeOH. Final product: Boc-NetN-ph-NO_2.

Synthesis of *N*-(2-Aminoethyl)-3-nitrobenzamide (10). Removal of Boc group from (9). 0.1 mEq of cmpd 9 was deblocked by dissolution in a mixture of TFA 20 % v/v in DCM at RT. After 17 h the reaction was complete. 20 volumes of toluene were added to the mixture and the sample was dried by rotary evaporation. The reaction was followed by TLC (DCM:MeOH; 9:1). Final product: NetN-ph-NO_2.

Synthesis of 2-[*N*-Methyl(1-*tert*-butoxyethenyl)amino]-1-[2-(*m*-nitrobenzoyl-amino) ethylamino]-1-ethanone (11). A chromophoric amide of Boc-Sarcosine.

0.1 mEq of Boc-sarcosine was mixed with 0.2 mEq of TEA and an excess of isobutyl chloroformate in ACN under stirring at RT. On the other hand, after 15 min, 0.1 mEq of cmpd 10 was dissolved in ACN and add it dropwise to the reaction. After 30 min the reaction was complete. It was followed by TLC (DCM:MeOH; 9:1). The crude product was purified by ColCh with a mixture of DCM:MeOH. Final product: Boc-Sar-NetN-ph-NO_2.

Synthesis of 2-(Methylamino)-1-[2-(m-nitrobenzoylamino)ethylamino]-1-ethanone (12). Removal of Boc group from (11). The chromophore-Sarcosine compound.

0.1 mEq of cmpd 11 was dissolved in a mixture of TFA 20% v/v in DCM at RT. After 17 h the reaction was complete. 20 volumes of toluene were added to the mixture and the sample was dried by rotary evaporation. The reaction was followed by TLC (DCM:MeOH; 9:1). Final product: Sar-NetN-ph-NO_2. (a chromophoric amide of sarcosine)

Synthesis of Methyl 5-(*N*-methyl{2-[2-(*p*-nitrobenzoylamino)ethylamino]-2-oxoethyl}amino)-5-oxovalerate (13). Amide of the cmpd 12 with glutaric acid monomethyl ester.

0.1 mEq of cmpd 12 was mixed with 0.2 mEq of TEA in ACN under stirring at RT. Then, 0.1 mEq of glutaric acid monomethyl ester chloride was dissolved in ACN and this solution was added dropwise on the first solution. After 30 min the reaction was complete. The reaction was followed by TLC (DCM: MeOH; 9:1). When the reaction was complete, the mixture was dried under vacuum and extracted with a mixture of water: DCM. The organic phase was collected and dried under vacuum. Final product: meO-glt-Sar-NetN-ph-NO_2.

S.1.2 *Characterization of intermediates and final products*

Methyl 5-oxo-5-[(*tert*-butoxycarbonylmethyl)amino]valerate (1).

Appearance: transparent oil. The molecular weight of the compound was 273.33 g/mol. The yield of the reaction was 100 % (Figure S-2).

^{1}H NMR (500 MHz, Chloroform-*d*) δ 4.16 (s, 1H), 3.64 (s, 2H), 3.12 (s, 2H), 2.90 (t, *J* = 5.4 Hz, 1H), 2.35 (t, *J* = 5.5 Hz, 1H), 1.96 (p, *J* = 5.5 Hz, 1H), 1.43 (s, 5H).

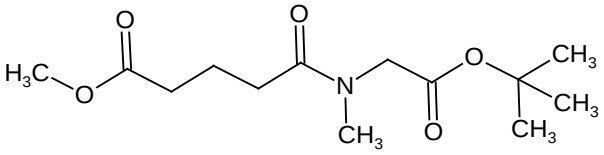

Figure S-2. Chemical structure of methyl 5-[(2-*tert*-butoxy-2-oxoethyl)(methyl)amino]-5-oxopentanoate (meO-glt-Sar-O-tbut).

Potassium 5-Oxo-5-(*tert*-butoxycarbonylamino)valerate (2).

Appearance: transparent-yellowish oil. The molecular weight of the compound was 297.39 g/mol. The yield of the reaction was 96.9 % (Figure S-3).

^{1}H NMR (500 MHz, DMSO-d_6) δ 4.11 (s, 1H), 2.97 (s, 2H), 2.32 (t, J = 7.1 Hz, 1H), 2.27 (t, J = 7.1 Hz, 1H), 2.02 (p, J = 7.1 Hz, 1H), 1.42 (s, 5H).

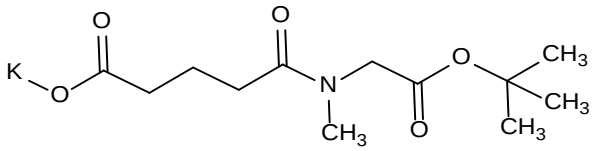

Figure S-3. Chemical structure of Potassium 5-Oxo-5-(*tert*-butoxycarbonylamino)valerate (KO-glt-Sar-O-tbut).

Methyl 6-oxo-6-[(*tert*-butoxycarbonylmethyl)amino]hexanoate (3).

Appearance: transparent oil. The molecular weight of the compound was 273.33 g/mol. The yield of the reaction was 100 % (Figure S-4).

^{1}H NMR (500 MHz, Chloroform-*d*) δ 6.73 (s, 1H), 4.17 (s, 1H), 3.64 (s, 2H), 2.52 (t, J = 8.0 Hz, 1H), 2.35 (t, J = 8.1 Hz, 1H), 1.77-1.67 (m, 1H), 1.61 (pd, J = 7.9, 1.1 Hz, 1H), 1.43 (s, 5H).

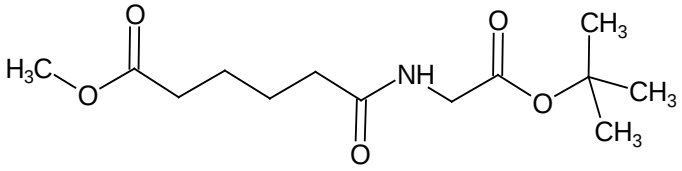

Figure S-4. Chemical structure of methyl 6-[(2-*tert*-butoxy-2-oxoethyl)amino]-6-oxohexanoate (meO-adp-Gly-O-tbut).

Potassium 6-Oxo-6-(tert-butoxycarbonylamino)hexanoate (4).

Appearance: transparent-yellowish oil. The molecular weight of the compound was 297.39 g/mol. The yield of the reaction was 97 % (Figure S-5).

^{1}H NMR (500 MHz, DMSO-d_6) δ 8.49 (s, 1H), 4.17 (s, 2H), 2.30-2.24 (m, 2H), 2.16-2.10 (m, 1H), 2.13 (s, 1H), 1.56-1.45 (m, 4H), 1.42 (s, 9H).

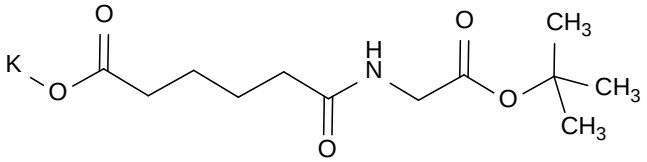

Figure S-5: Chemical structure of potassium 6-Oxo-6-(tert-butoxycarbonylamino)hexanoate (KO-adp-Gly-O-tbut).

***tert*-butyl {2-[(4-hydroxypentanoyl)amino]ethyl}carbamate (8).**

Appearance: transparent oil. The molecular weight of the compound was 260.33 g/mol. The yield of the reaction was 100 %. (Figure S-6).

^{1}H NMR (500 MHz, Chloroform-*d*) δ 6.16 (s, 1H), 5.05 (s, 1H), 4.13 (ddd, *J* = 12.3, 3.1, 1.3 Hz, 1H), 3.92 (ddd, *J* = 12.3, 3.1, 1.3 Hz, 1H), 3.74 (dqd, *J* = 11.4, 6.8, 2.4 Hz, 1H), 3.20 (td, *J* = 12.1, 3.1 Hz, 1H), 3.06 (td, *J* = 12.1, 3.1 Hz, 1H), 2.70 (td, *J* = 12.4, 4.0 Hz, 1H), 2.15 (td, *J* = 12.5, 1.5 Hz, 1H), 1.97 (s, 1H), 1.88 (tdd, *J* = 12.6, 11.4, 4.1 Hz, 1H), 1.70 (tdd, *J* = 12.5, 2.4, 1.4 Hz, 1H), 1.44 (s, 9H), 1.16 (d, *J* = 6.9 Hz, 3H).

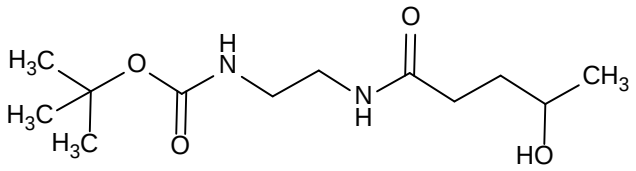

Figure S-6. Chemical structure of *tert*-butyl {2-[(4-hydroxypentanoyl)amino]ethyl}carbamate (Boc-NetN-val-secOH).

***tert*-butyl (2-{[(3-nitrophenyl)carbonyl]amino}ethyl)carbamate (9).**

Appearance: yellow oil. The molecular weight of the compound was 309.32 g/mol. The yield of the reaction was 100 %. (Figure S-7).

^{1}H NMR (500 MHz, Chloroform-*d*) δ 8.60 (t, *J* = 2.0 Hz, 1H), 8.48 (ddt, *J* = 20.7, 7.5, 1.9 Hz, 2H), 7.63 (t, *J* = 7.5 Hz, 1H), 6.75 (s, 1H), 5.12 (s, 1H), 3.74 (t, *J* = 4.3 Hz, 2H), 3.58 (t, *J* = 4.3 Hz, 2H), 1.44 (s, 9H).

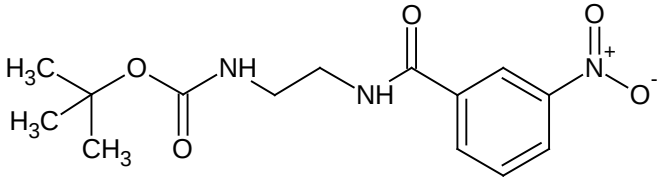

Figure S-7. Chemical structure of *tert*-butyl (2-{[(3-nitrophenyl)carbonyl]amino}ethyl)carbamate (Boc-NetN-ph-NO_2).

***N*-(2-aminoethyl)-3-nitrobenzamide (10).**

Appearance: yellow oil. The molecular weight of the compound was 209.2 g/mol. The yield of the reaction was 100 %. (Figure S-8).

^{1}H NMR (500 MHz, Deuterium Oxide) δ 8.46 (dp, *J* = 3.8, 2.0 Hz, 2H), 8.30 (dt, *J* = 7.5, 2.0 Hz, 1H), 7.65 (t, *J* = 7.7 Hz, 1H), 6.75 (s, 1H), 4.70 (s, 2H), 3.94 (t, *J* = 5.0 Hz, 2H), 3.26 (t, *J* = 5.0 Hz, 2H).

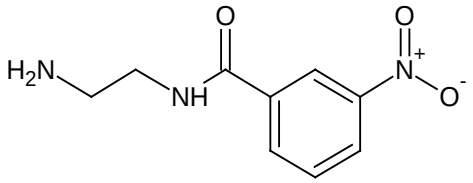

Figure S-8. Chemical structure of *N*-(2-aminoethyl)-3-nitrobenzamide (NetN-ph-NO_2).

2-[*N*-Methyl(1-*tert*-butoxyethenyl)amino]-1-[2-(*m*-nitrobenzoylamino)ethylamino]-1-ethanone (11).

Appearance: yellow powder. The molecular weight of the compound was 378.43 g/mol. The yield of the reaction was 100 %. (Figure S-9).

^{1}H NMR (500 MHz, Chloroform-*d*) δ 8.59 (t, *J* = 2.0 Hz, 1H), 8.46 (dt, *J* = 7.3, 1.9 Hz, 1H), 8.12 (dt, *J* = 7.5, 2.0 Hz, 1H), 7.67 (t, *J* = 7.5 Hz, 1H), 7.34 (s, 1H), 6.75 (s, 1H), 4.04-3.95 (m, 4H), 3.58 (t, *J* = 7.5 Hz, 2H), 3.05 (s, 3H), 2.71 (d, *J* = 2.2 Hz, 1H), 2.42 (d, *J* = 2.2 Hz, 1H), 1.36 (s, 9H).

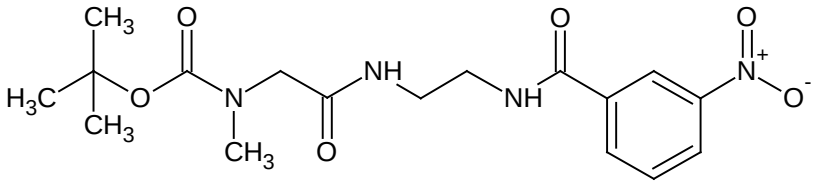

Figure S-9. Chemical structure of 2-[*N*-Methyl(1-*tert*-butoxyethenyl)amino]-1-[2-(*m*-nitrobenzoylamino) ethylamino]-1-ethanone (Boc-Sar-NetN-CO-ph-NO_2).

2-(Methylamino)-1-[2-(*m*-nitrobenzoylamino)ethylamino]-1-ethanone (12).

Appearance: yellow powder. The molecular weight of the compound was 378.43 g/mol. The yield of the reaction was 100 %. (Figure S-10).

^{1}H NMR (500 MHz, Deuterium Oxide) δ 8.53-8.43 (m, 2H), 8.04 (dt, *J* = 7.5, 2.0 Hz, 1H), 7.63 (t, *J* = 7.5 Hz, 1H), 6.75 (s, 1H), 4.70 (s, 2H), 3.98 (t, *J* = 4.9 Hz, 2H), 3.58 (t, *J* = 4.9 Hz, 2H), 3.44 (s, 2H), 3.32 (s, 3H).

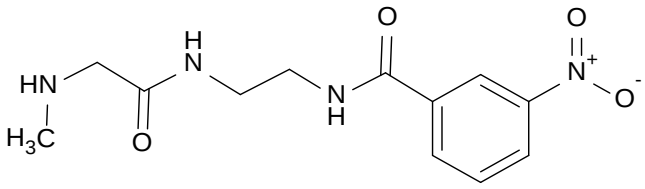

Figure S-10. Chemical structure of 2-(Methylamino)-1-[2-(*m*-nitrobenzoylamino)ethylamino]-1-ethanone (Sar-NetN-CO-ph-NO_2).

Methyl 5-(*N*-methyl{2-[2-(*p*-nitrobenzoylamino)ethylamino]-2-oxoethyl}amino)-5-oxovalerate (13).

Name of the structure: Methyl 5-(*N*-methyl{2-[2-(*p*-nitrobenzoylamino)ethylamino]-2-oxoethyl}amino)-5-oxovalerate.

Appearance: yellow powder. The molecular weight of the compound was 408.41 g/mol. The yield of the reaction was 68.41% (Figure S-11).

^{1}H NMR (500 MHz, Chloroform-*d*) δ 9.69 (s, 1H), 8.33-8.27 (m, 2H), 7.99-7.93 (m, 2H), 6.75 (s, 1H), 4.09 (s, 2H), 3.98 (t, *J* = 4.5 Hz, 2H), 3.64 (s, 3H), 3.58 (t, *J* = 4.5 Hz, 2H), 3.00 (s, 3H), 2.90 (t, *J* = 8.0 Hz, 2H), 2.35 (t, *J* = 5.3 Hz, 2H), 1.96 (tt, *J* = 8.1, 5.3 Hz, 2H).

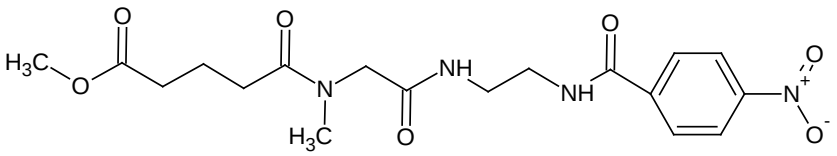

Figure S-11. Chemical structure of Methyl 5-(*N*-methyl{2-[2-(*p*-nitrobenzoylamino)ethylamino]-2-oxoethyl}amino)-5-oxovalerate (meO-glt-Sar-NetN-CO-ph-NO_2).